From the Cécile and Oskar Vogt Institute of Brain Research

at Heinrich Heine University Düsseldorf

Development of an anatomo-functional model of Broca's region based on cytoarchitecture, connectivity, and language function

Dissertation

to obtain the academic title of Doctor rerum medicarum (Dr. rer. med.) from the Faculty of Medicine at Heinrich Heine University Düsseldorf

submitted by

Nataliia Fedorchenko

(2026)

As an inaugural dissertation printed by permission of the

Faculty of Medicine at Heinrich Heine University Düsseldorf

signed:

Dean: Prof. Dr. med. Nikolaj Klöcker

Examiners: Prof. Dr. med. Dr. h. c. Katrin Amunts, Prof. Dr. Dr. h. c. Angela D. Friederici

"If I have seen further, it is by standing on the shoulders of Giants."

Isaac Newton[1]

[1] Newton, I. (1675). Letter to R. Hooke, 5 February 1675

Parts of this work have been published:

- *"High-Resolution 3D Mapping of Cytoarchitectonic Areas 44 and 45 Reveals New Anatomical Details of Broca's Region"*, proceedings of the 118th Annual Meeting of the Anatomical Society – Tripartite Meeting of the Anatomische Gesellschaft, Austrian Society of Anatomy, and Swiss Society for Anatomy, Histology and Embryology, Graz, Austria, 25–27 September 2024. (Poster).
- *"High-Resolution 3D Mapping Within Areas 44 and 45 – New Cytoarchitectonic Subdivisions in Broca's Region"*, proceedings of the 16th Göttingen Meeting of the German Neuroscience Society, Göttingen, Germany, 26–29 March 2025. (Talk).
- *"Fine-Grained Cytoarchitectonic Parcellation of Broca's Region Supports Functional Differentiation — In Julich-Brain Atlas (EBRAINS)",* presented at the EBRAINS Summit 2025, Brussels, on 8-11 December 2025, Brussel, Belgium. (Poster)

Summary

In this study, four new areas were mapped within Broca's region, cytoarchitectonic areas 44 and 45. The parcellation of this region is thus more fine-grained than previously thought. The location, extent, and inter-individual variability were represented in probabilistic maps in stereotaxic space. This allows us to use them as a detailed reference for functional activations. Multidimensional scaling for the areas of the left and right hemispheres, and cluster analysis, revealed similarities between areas and thus gave evidence of their functional relationship. Euclidean distance analyses revealed systematic structural asymmetry across Broca's region areas 44p, 44a, 45p, and 45a. Posterior area 44p showed moderate but variable left-right cytoarchitectonic differences, whereas area 44a exhibited small and consistent structural asymmetry. Area 45a displayed the strongest descriptive lateralisation, while area 45p had low median asymmetry but high inter-individual variability. Overall, areas 44p and 45p were more variable in cytoarchitecture, whereas areas 44a and 45a were more consistent with lateralisation peaking in area 45a and moderate in 44p. The sulcal morphology of the diagonal sulcus (DS), Ramus ascendens (RA), Sylvian fissure (SF), and horizontal ramus (RH) seems to influence the precise positioning of borders between areas 44p, 44a, 45p, and 45a, suggesting a combination of microstructural continuity and local anatomical variability. Volume analyses suggested overall leftward asymmetry in area 44p, with trends toward leftward asymmetry in area 44a, whereas areas 45p and 45a were largely symmetric. No significant sex differences in regional volumes were observed, although males tended to have slightly larger volumes and showed a trend toward stronger leftward asymmetry in posterior areas. The presence of a diagonal sulcus was associated with increased volumes in areas 44a and 44p, particularly in area 44a, suggesting the sulcal morphology contributes to local volumetric variability; however, our results did not reach significance.

Furthermore, functional peak activation mapping from the fMRI studies onto the probability maps of the areas 44p, 44a, 45p, and 45a showed that in the left hemisphere, syntactic and semantic activations predominantly overlap with areas 44p, 44a and 45a, whereas lexical/phonological processing involved area 44a and adjacent opercular areas, action-related activations engaged area 44p, as well as premotor, and opercular areas, area 45p involved in semantic processing. The right hemisphere included fewer peaks, mainly in premotor areas 44p and the insula. These findings suggest a close structure-function relationship within Broca's region, where anteriorly located areas 44a, 45a, and 45p are associated with language-related functions such as syntax and semantics, while posterior area 44p contributes to syntax and action-related and motor processes. The asymmetrical distribution of activations, with the left hemisphere showing extensive language-related peaks, further supports the link between cytoarchitectonic lateralisation and functional specialisation in Broca's region.

BrainMap meta-analytic functional characterisation confirmed domain-general cognitive involvement across all Broca's region subdivisions. MACM analyses revealed partially overlapping but distinct co-activation networks. Posterior areas (44p, 45p) displayed bilateral co-activation, whereas anterior areas (44a, 45a) were predominantly left-lateralised, co-activating fronto-parietal, thalamic, and posterior superior temporal gyrus (pSTG) regions. Specifically, posterior areas 44p and 45p shared a frontal-insular-precentral core, with area 44p uniquely co-activating posterior parietal and thalamic regions, and area 45p engaging limbic and medial temporal structures. Anterior areas 44a and 45a shared fronto-parietal-thalamic networks, with area 44a uniquely recruiting intraparietal and multiple thalamic nuclei, and area 45a engaging fronto-opercular, premotor, and occipital areas. These results indicate that structural heterogeneity within Broca's region underlies functional differentiation, with posterior areas supporting sensorimotor and action-related processes, and anterior areas contributing to higher-order cognitive and language functions.

Overlapping the MPMs of areas 44p, 44a, 45p, and 45a with task-evoked ECoG data (Liu et al., 2025) further demonstrated that speech-related high-gamma activity is largely localised outside classical Broca's region areas, predominating in premotor cortex, with only limited overlap in ventral 44a and, to a lesser extent, 44p for sequence complexity. Visual alignment of middle precentral gyrus activity with the cytoarchitectonic maps of Ruland et al (2025) suggests potential correspondence with ventral premotor subdivisions areas 6v2 and 6v3, though precise registration with Julich-Brain Atlas MPMs is required. Systematic mapping of all electrode activations onto these MPMs would allow quantitative assignment of sequence- and articulatory-related effects to specific cortical areas across participants, integrating functional electrophysiology with cytoarchitectonic reference maps.

These maps will be publicly available as part of the Julich Brain Cytoarchitectonic Atlas (https://julich-brain-atlas.de/), which is included within EBRAINS research infrastructure (https://ebrains.eu/services/human-brain-atlas).

Zusammenfassung

In dieser Studie wurden vier neue Areale innerhalb der Broca-Region neu kartiert, die zytoarchitektonischen Areale 44 und 45. Die Parzellierung dieser Region ist somit feiner als bisher angenommen. Die Lage, Ausdehnung und interindividuelle Variabilität wurden in probabilistischen Karten im stereotaktischen Raum dargestellt. Dies ermöglicht es uns, sie als detaillierte Referenz für funktionelle Aktivierungen zu verwenden. Die multidimensionale Skalierung für die Bereiche der linken und rechten Hemisphären sowie die Clusteranalyse ergaben Ähnlichkeiten zwischen den Bereichen und lieferten somit Hinweise auf ihre funktionelle Beziehung. Euklidische Distanzanalysen ergaben eine systematische strukturelle Asymmetrie über die Broca-Areale 44p, 44a, 45p und 45a hinweg. Das hintere Areal 44p zeigte moderate, aber variable zytoarchitektonische Unterschiede zwischen links und rechts, während das Areal 44a eine geringe und konsistente strukturelle Asymmetrie aufwies. Das Areal 45a zeigte die stärkste deskriptive Lateralisierung, während das Areal 45p eine geringe mediane Asymmetrie, aber eine hohe interindividuelle Variabilität aufwies. Insgesamt waren die Areale 44p und 45p in ihrer Zytoarchitektur variabler, während die Areale 44a und 45a konsistenter waren, mit einer maximalen Lateralisierung im Areal 45a und einer moderaten Lateralisierung im Areal 44p. Die Sulkusmorphologie des Sulcus diagonalis (DS), des Ramus ascendens (RA), der Sylvian-Fissur (SF) und des horizontalen Ramus (RH) scheint die genaue Positionierung der Grenzen zwischen den Arealen 44p, 44a, 45p und 45a zu beeinflussen, was auf eine Kombination aus mikrostruktureller Kontinuität und lokaler anatomischer Variabilität hindeutet. Volumenanalysen deuteten auf eine allgemeine Linksasymmetrie im Areal 44p hin, mit Tendenzen zur Linksasymmetrie im Areal 44a, während die Areale 45p und 45a weitgehend symmetrisch waren. Es wurden keine signifikanten geschlechtsspezifischen Unterschiede in den regionalen Volumina beobachtet, obwohl Männer tendenziell etwas größere Volumina aufwiesen und eine Tendenz zu einer stärkeren Linksasymmetrie in den hinteren Arealen zeigten. Das Vorhandensein eines diagonalen Sulcus war mit erhöhten Volumina in den Arealen 44a und 44p verbunden, insbesondere im Areal 44a, was darauf hindeutet, dass die Sulcusmorphologie zur lokalen Volumenvariabilität beiträgt; unsere Ergebnisse erreichten jedoch keine Signifikanz.
Darüber hinaus zeigen die funktionellen Peak-Aktivierungen aus den fMRI-Studien auf den Wahrscheinlichkeitskarten der Areale 44p, 44a, 45p und 45a, dass in der linken Hemisphäre syntaktische und semantische Aktivierungen überwiegend mit den Arealen 44p, 44a und 45a überlappen, während die lexikalische/phonologische Verarbeitung das Areal 44a und angrenzende Opercular-Bereiche betraf. Bei handlungsbezogenen Aktivierungen waren das Areal 44p und die prämotorischen und operkulären Bereiche sowie das Areal 45p an der semantischen Verarbeitung beteiligt. Die rechte Hemisphäre wies weniger Spitzen auf, hauptsächlich in den prämotorischen Arealen 44p und der Insula. Diese Ergebnisse deuten auf eine enge Struktur-Funktions-Beziehung innerhalb der Broca-Region hin, wo die anterior gelegenen Areale 44a, 45a und 45p mit sprachbezogenen Funktionen wie Syntax und Semantik assoziiert sind, während das posterior

gelegene Areal 44p zu Syntax- und handlungsbezogenen sowie motorischen Prozessen beiträgt. Die asymmetrische Verteilung der Aktivierungen, wobei die linke Hemisphäre umfangreiche sprachbezogene Spitzen aufweist, unterstützt zusätzlich den Zusammenhang zwischen zytoarchitektonischer Lateralisation und funktioneller Spezialisierung in Brocas Arealen.
Die metaanalytische funktionelle Charakterisierung von BrainMap bestätigte eine domänenübergreifende kognitive Beteiligung in allen Unterteilungen von Brocas Arealen. Die hinteren Areale (44p, 45p) zeigten eine bilaterale Koaktivierung, während die vorderen Areale (44a, 45a) überwiegend links lateralisiert waren und mit fronto-parietalen, thalamischen und hinteren superior temporalen Regionen koaktivierten, einschließlich des hinteren superior temporalen Gyrus (pSTG), einer Kernkomponente des klassischen fronto-temporalen (IFG-pTC) Sprachsystems, das die syntaktische und semantische Verarbeitung unterstützt. MACM-Analysen ergaben teilweise überlappende, aber unterschiedliche Koaktivierungsnetzwerke: Die hinteren Areale 44p und 45p hatten einen gemeinsamen frontalen-insulären-präzentralen Kern, wobei Areal 44p einzig die hinteren parietalen und thalamischen Regionen koaktivierte und Areal 45p limbische und mediale temporale Strukturen einbezog. Die vorderen Areale 44a und 45a teilten sich fronto-parietale-thalamische Netzwerke, wobei das Areal 44a einzig intraparietale und multiple thalamische Kerne einbezog und das Areal 45a fronto-operkuläre, prämotorische und okzipitale Areale einbezog. Diese Ergebnisse deuten darauf hin, dass alle Areale der Broca-Region zu domänenübergreifenden kognitiven Funktionen beitragen, aber jeder Bereich an teilweise unterschiedlichen Netzwerken beteiligt ist, die die funktionale Spezialisierung widerspiegeln. Die hinteren Bereiche integrieren sensomotorische und assoziative Bereiche und unterstützen motorische und handlungsbezogene Prozesse, während die vorderen Bereiche durch fronto-parietale und thalamische Netzwerke zu höheren kognitiven und sprachbezogenen Funktionen beitragen. Die unterschiedlichen Co-Aktivierungsmuster deuten darauf hin, dass die strukturelle Heterogenität innerhalb der Broca-Region der funktionellen Differenzierung zugrunde liegt, wobei jeder Bereich einzigartige Konnektivitätsprofile bildet, die wahrscheinlich die spezifischen kognitiven und sprachlichen Funktionen unterstützen.

Die Überlagerung der MPMs der Areale 44p, 44a, 45p und 45a mit aufgabenbezogenen ECoG-Daten (Liu et al., 2025) zeigte weiter, dass die sprachbezogene Hoch-Gamma-Aktivität weitgehend außerhalb der klassischen Broca-Region lokalisiert ist und vorwiegend im prämotorischen Kortex auftritt, mit nur begrenzter Überlappung im ventralen 44a und in geringerem Maße im 44p für Sequenzkomplexität. Die manuelle, rein visuelle Ausrichtung der Aktivität des mittleren präzentralen Gyrus mit den zytoarchitektonischen Karten von Ruland et al. (2025) deutet auf eine mögliche Korrespondenz mit den ventralen prämotorischen Unterarealen 6v2 und 6v3 hin, wobei noch eine genaue Registrierung mit den MPMs des Julich-Brain-Atlases erforderlich ist. Eine systematische Kartierung aller Elektrodenaktivierungen auf diese MPMs würde eine quantitative Zuordnung von sequenz- und artikulationsbezogenen Effekten zu bestimmten kortikalen Arealen bei allen Teilnehmern ermöglichen und damit die funktionelle Elektrophysiologie mit zytoarchitektonischen Referenzkarten kombinieren.

Diese Karten werden als Teil des Julich Brain Cytoarchitectonic Atlas (https://julich-brain-atlas.de/), welcher Bestandteil von EBRAINS (https://ebrains.eu/services/human-brain-atlas) ist, öffentlich zugänglich sein.

List of Abbreviations

IFG inferior frontal gyrus

prCG pre-central gyrus

IQRs interquartile ranges

PM premotor cortex

ROIs regions of interest

STG superior temporal gyrus

pmaps probability maps

MPMs maximum probability maps

CNNs convolutional neural networks

MACM meta-analytic connectivity modelling

AF arcuate fasciculus

BA Brodmann area

GLI Grey Level Index

2D two-dimensional

3D three-dimensional

MRI magnetic resonance imaging

fMRI functional magnetic resonance imaging

ALE activation likelihood estimation

MA modelled activation

FEW family-wise error

preCS pre-central sulcus

IFJ inferior frontal junction

IFS inferior frontal sulcus

LAD lesion-activation distance

Op frontal operculum

MFG middle frontal gyrus

MDS multidimensional scaling

RA Ramus ascendens

RH Ramus horizontal

TS triangular sulcus

DLPFC dorsolateral prefrontal cortex

SF Sylvian fissure

IPL inferior parietal lobule

IPS intraparietal sulcus

pSTG posterior superior temporal gyrus

TPJ temporo-parietal junction

VLP ventral lateral posterior thalamic nucleus

MNI Montreal Neurological Institute

DOI Digital Object Identifier

MD Mahalanobis distance

Siibra software interface for interacting with brain atlases

SPM Statistical Parametric Mapping

NifTI Neuroimaging Informatics Technology Initiative

ECoG Electrocorticography

BC brain code

mPrCG middle precentral gyrus

pTC posterior temporal cortex

Table of Contents

1. Introduction

1.1 Anatomy and Function of Broca's Region

Broca's region (Broca, 1861), located in the inferior frontal gyrus (IFG), comprises cytoarchitectonically defined areas 44 and 45, corresponding to the Pars opercularis and Pars triangularis, respectively (Amunts et al., 1999; Brodmann, 1909; Petrides & Pandya, 2012; Sarkisov et al., 1955). During ontogenesis, areas 44 and 45 undergo substantial postnatal changes, characterised by a sharp decrease in cell-body density and a large increase in neuropil during infancy and early childhood (Shankle et al., 1999; Uylings et al., 2005). These changes reflect the rapid growth of dendrites, axons, and synapses that are critical for language development. Interhemispheric asymmetry emerges gradually: initially, both areas are structurally similar across hemispheres, but adult-like left-hemisphere specialisation develops later, around 5-6 years for area 45 and about 11-12 years for area 44 (Amunts et al., 2003). Comparative studies indicate that the posterior area 44 in humans, associated with action, aligns with the core area 44 of chimpanzees, while the anterior area 44 supports syntactic processes unique to humans, reflecting evolutionary expansion and left-right lateralisation of Broca's region (Gallardo et al., 2023). Recent evidence shows that the development of lateralised white matter pathways connecting Broca's region to temporal regions also follows a fine-grained trajectory: in preschool children, the dorsal tract targeting posterior Broca's area 44 shows localised microstructural asymmetry that correlates with language skills, whereas the tract targeting the premotor cortex (area 6) does not (Eichner et al., 2024). By adulthood, the left hemisphere exhibits increased neuropil, indicative of greater connectivity, aligning with its dominant role in language. Structural maturation continues into late childhood and adulthood, suggesting ongoing experience-dependent plasticity shaped by language use (Amunts et al., 2003).

Over two decades ago, in our lab, cytoarchitectonic areas 44 and 45 were systematically mapped using an observer-independent method. This work provided the first quantitative mapping of areas 44 and 45, revealing substantial inter-individual variability in cell densities and volumes. Additionally, during this work, the indications of potential internal subdivisions within both areas were noted. However, the scope of that study was limited to delineating the overall boundaries of areas 44 and 45, these finer subdivisions were not systematically investigated at that time (Amunts et al., 1999). Building on this framework, the following work provided a more detailed parcellation of Broca's region based on the distribution of six neurotransmitter receptors. This study revealed previously unknown further subdivisions of areas 44 and 45 into dorsal/ventral and anterior/posterior areas. In addition, they identified areas in the neighbourhood, such as area 6r1 in the ventral precentral sulcus (Ruland et al., 2025) and Op8 and Op9 in the frontal operculum (Saal, 2019). Importantly, the study demonstrated a significant left-ward asymmetry in cholinergic M2 receptors, supporting a link between molecular architecture and the left-hemispheric dominance for language. This receptor-based mapping offered a nuanced, functionally relevant perspective on the organisation of Broca's region, highlighting its complex structural and functional segregation beyond traditional cytoarchitectonic boundaries (Amunts et al., 2010).

Functionally, in adults, area 45 predominantly supported semantic processes, whereas area 44 contributed to syntactic processes (Goucha et al., 2017; Hagoort & Indefrey, 2014; Rodd et al., 2015). Hagoort (2005) proposed a broader unification framework, conceptualising the left IFG as a unified linguistic workspace. In this framework, area 44 participated in syntactic unification, phonological processing, and structural binding, whereas area 45 contributed to semantic unification, controlled semantic retrieval, and context-sensitive integration. Foundational work by Grodzinsky & Friederici (2006) proposed that Broca's region supports hierarchical, long-distance syntactic dependencies, providing a neuroanatomical basis for functional heterogeneity within the IFG. Building on this,

Friederici (2011, 2017b; 2015) suggested that area 44 implemented *Merge*, the core combinatorial operation in syntax responsible for hierarchical syntactic structure, whereas area 45 contributed to semantic retrieval and integration, linking syntactic computations to meaning. She further situated these areas within distinct temporo-frontal networks, showing a left-lateralised dorsal pathway connecting area 44 to posterior temporal cortex for syntactic processing, and a less lateralised ventral pathway linking area 45 to anterior/middle temporal regions for semantic processing. A key strength of this work was the use of cytoarchitectonic maps, which enabled the precise localisation of areas 44 and 45 and robust mapping of structure-function relationships (Friederici, 2011). Consistent with this functional evidence, later studies demonstrated that activity in left area 44 during an artificial grammar task specifically correlated with syntactic performance and natural language comprehension, supporting its classical role in syntactic processing and highlighting the ecological validity of functionally localised regions of interest (ROIs). (Liu et al., 2023). Complementing this functional evidence, structural connectivity evidence by Wu et al. (2022) demonstrated that Brodmann areas (BA) 44 and 45 were connected via multiple long-range association tracts, including the arcuate fasciculus, superior longitudinal fasciculus, inferior fronto-occipital fasciculus, frontal aslant tract, and frontal longitudinal fasciculus linking Broca's region to temporal, parietal, and frontal cortices. A comparative neuroanatomical study indicated that the posterior portion of BA 44 in humans, together with its dorsal fiber connections to the temporal cortex, constituted a neural circuit absent in nonhuman primates. This difference may underlie the uniquely human capacity for hierarchical syntax (Friederici, 2017a). More recent research suggested finer-grained functional specialisation within area 44: the anterior portion appears to implement syntactic operations such as *Merge*, while the posterior portion supports action-related computations and context-based selection (Papitto et al., 2024; Zaccarella et al., 2021). However, Fedorenko et al. (2012) offered a somewhat different perspective, showing that Broca's region was functionally heterogeneous, with subregions differentially involved in language versus domain-general tasks, and that language processing relied on a broader distributed network beyond the classical IFG areas. Complementing these views, Hickok (2013) emphasised that activation in BA 44 and 45 may have reflected domain-general processes, indicating working memory, cognitive control, or phonological rehearsal, rather than strictly syntactic or semantic computations. Expanding on this, Hickok et al. (2022) proposed that articulatory control was implemented by separate dorsal and ventral premotor circuits, with Broca's region positioned at a higher level to plan, sequence, and integrate speech, rather than executing motor commands directly. Most recent research has further revealed that Broca's region, traditionally associated with language processing, plays a critical role in planning and coordinating speech production. Fluent speech relies on precise speech-motor sequencing, which is mediated by a distributed cortical network that includes Broca's region and the middle precentral gyrus. Within this network, sustained neural activity predicts speech performance, and targeted stimulation can induce speech disfluencies resembling apraxia (Liu et al., 2025). These findings highlight the integral role of Broca's region not only in language but also in orchestrating the motor processes essential for fluent speech.

Taken together, the evidence demonstrated that Broca's region was structurally and functionally heterogeneous, with cytoarchitectonic areas 44 and 45 supporting distinct aspects of language, including syntactic processing, semantic integration, and speech-motor planning. Studies of microanatomy and function revealed that each area contributed differentially to linguistic and motor functions. Lesions of Broca's region and its associated connections could result in distinct patterns of language and speech impairments. This provided the foundation for reviewing the clinical and neurobiological consequences of Broca's region dysfunction, which are addressed in the following chapter.

1.2 Clinical and Neurobiological Consequences of Broca's Area Dysfunction

Since Paul Broca's seminal description of motor aphasia in the 19th century (Broca, 1861), lesions to the posterior inferior frontal gyrus (IFG) have been strongly linked to impairments in speech production. In clinical practice, BA 44 and 45 are often used as anatomical correlates of Broca's region, and their lesions in the dominant hemisphere are traditionally associated with motor aphasia (Mandonnet & Duffau, 2021). Consistent with this association, individuals with strokes or tumours in the IFG are less likely to develop aphasia compared with those whose lesions involve key white matter pathways, such as the AF (Bizzi et al., 2012). Early neuroimaging work investigating left IFG damage revealed that such lesions disrupt attentionally demanding lexical processes while sparing simpler ones. Patients with IFG infarcts exhibited abnormal recruitment of the right IFG along with prelesional activation in surviving left IFG tissue. Only the latter correlated with improved behavioural recovery. These findings suggested that functional restoration of residual left-hemisphere substrate, rather than contralateral compensation alone, is critical for language improvement after IFG injury (Rosen et al., 2000).

Tractography analyses further clarified the anatomical pathways underlying IFG dysfunction. Contrary to traditional assumptions, the AF does not project directly into Broca's region but terminates predominantly in PM and motor cortices (BA6/BA4). This implies that AF damage affects speech planning and monitoring via dorsal motor-articulatory systems, rather than by severing a direct link between temporal language regions and Broca's region. These insights reshaped the classical disconnection model, emphasising a distributed dorsal network supporting repetition and speech production, with Broca's region acting as one component within a broader architecture (Bernal & Ardila, 2009).

Electrocorticographic evidence has further refined our understanding of IFG function. Broca's region does not serve as the primary locus of articulatory execution. Still, it performs pre-articulatory operations: transforming sensory-phonological representations from the temporal cortex into articulatory codes implemented in motor regions. Importantly, Broca's region becomes functionally silent during actual articulation, implying that its dysfunction impairs speech not by eliminating motor control but by disrupting the integrative processes that prepare and structure articulatory gestures. Together, these findings reinterpret both the clinical deficits and recovery mechanisms associated with IFG lesions, positioning Broca's region as a computational hub within a dynamic, interacting network (Flinker et al., 2015).

Clinically, caution regarding IFG lesions remains warranted, as even minor damage can disrupt speech. However, neurosurgical perspectives highlight that Broca's region is embedded in a distributed, plastic network spanning temporal, parietal, and contralateral homologous regions. This network organisation explains why some patients recover function despite IFG damage, reinforcing the concept of Broca's region as a dynamic network rather than a fixed speech centre (Rutten, 2017).

Despite these advances, medical education and clinical practice continue to rely on Brodmann's 2D map. This persistence may reflect both historical inertia and an underestimation of neurosurgical evidence. As Mandonnet and Duffau (2021) note, Broca's original mislocalisation became deeply embedded in teaching and remains widely cited in textbooks and university courses. Decades of intraoperative mapping had argued that Broca's region can be resected without any major consequences for permanent speech production, yet these findings failed to influence mainstream neurological models.

Reliance on Brodmann's 2D map has been considered insufficient because it cannot capture the substantial interindividual variability or the microstructural and functional heterogeneity of the IFG (Bulut, 2023; Zhang et al., 2017). Modern 3D atlases, incorporating cytoarchitecture,

receptorarchitecture, and connectivity, provide precise anatomical boundaries essential for accurate structure-function mapping. Distinct cytoarchitectonically defined IFG areas differ in microstructure and connectivity to the neighbouring and functionally related cortices, making refined parcellation indispensable for interpreting functional data (Bulut, 2022; Diveica et al., 2023). Accordingly, the next chapter reviews previous parcellation schemes of Broca's region, illustrating how its anatomical definition has evolved and why modern, precise frameworks are essential for linking structure to function.

1.3 Previous Parcellation Schemes of Broca's Region

Broca's region has been characterised through numerous parcellation schemes (Tab. 1). Brodmann's map introduced the classical BA 44 and 45 and provided one of the earliest widely adopted frameworks. However, this map offered no internal subdivisions within these areas, did not account for intersubject variability, and did not delineate the borders of the areas with respect to the surrounding sulcal landmarks. It also did not consider the cortex located in the sulci (Brodmann, 1909). Von Economo and Koskinas introduced more microstructural detail by identifying distinct medial, triangular, and opercular areas within the IFG (FCBm, FDr, FCDop) (von Economo & Koskinas, 1925). Sarkisov later refined these maps, proposing subdivisions 44, 45, and adding a further subdivision, 45a (Sarkisov et al., 1955). Petrides and Pandya highlighted longitudinal variation within area 45, delineating anterior (45A) and posterior (45B) subdivisions, reflecting functional distinctions observed in non-human primates (Petrides & Pandya, 2002). These early and more recent works collectively suggested that the inferior frontal cortex exhibits more heterogeneity than previously assumed.

These concepts were further developed by our lab using an observer-independent cytoarchitectonic approach to map Broca's region in ten post-mortem brains, identifying cytoarchitectonic areas 44 and 45 (Amunts et al., 1999). They provided the first quantitative assessment of intersubject variability in this region. Fabbri-Destro and Rizzolatti subsequently provided additional empirical support for the fundamental boundaries of these two cytoarchitectonic areas (Fabbri-Destro & Rizzolatti, 2008). In a pilot study, using a multireceptor approach to analyse Broca's region, our lab identified four subregions: dorsal, ventral, anterior, and posterior, corresponding to areas 44d, 44v, 45a, 45p (Fig. 1) (Amunts et al., 2010). Recent multimodal parcellations (Fan et al., 2016; Glasser et al., 2016) have proposed additional subdivisions, such as opercular, rostral, and caudal areas, based on functional connectivity, cortical thickness, and other MRI-derived features. While the later parcellations capture important macroscale functional and structural organisation, they do not truly reflect cytoarchitectonic boundaries, which are defined by cellular composition and layering (Bohland et al., 2009). MRI-based maps are also influenced by factors such as imaging resolution, registration algorithms, and population averaging, which can obscure fine-grained microstructural boundaries. For example, Pas et al. (2024) showed in a fixed macaque monkey brain that ultra-high-resolution diffusion MRI can reveal cortical cytoarchitectonic areas with fidelity, although not all regions are equally resolvable. This work highlights the potential of MRI to approximate cytoarchitecture but also emphasises why in vivo human parcellations, like those of Fan and Glasser, rely on coarser structural and functional proxies and cannot fully capture cellular-level borders. Consequently, while these atlases provide valuable functional and structural insights across the human brain, they cannot fully substitute for cytoarchitectonic delineations of cortical areas.

Brodmann (1909)	BA44, BA45
Economo and Koskinas (1925)	FCBm, FDr, FCDop
Sarkisov (1949)	44, 45, 45a

Petrides and Pandya (2002)	44, 45A, 45B
Amunts (1999)	44, 45
Fabbri-Destro and Rizzolatti	44, 45
Amunts (2010)	44v, 44d, 45a, 45p
Glasser (2016)	44, 45
Fan (2016)	44d, 44v, 44op, 45r, 45c

Table 1 Parcellation schemes of the human Broca's region. BA Brodmann area, FCB frontal disgranular pars basalis, medial sector, FDr frontal granular region triangularis, FCDop frontal transitional cortex opercular sector, 45a anterior area, 45A anterior area, 45B posterior (caudal) area, 44v ventral area, 44d dorsal area, 45a anterior area, 45p posterior area, 44op opercular area, 45r rostral area, 45c caudal area.

In summary, these efforts reveal pronounced microstructural complexity in Broca's region and highlight substantial anatomical variability across individuals. However, existing parcellation schemes differ markedly in their definitions, criteria, and relation to cortical landmarks, complicating direct comparison and leaving open questions regarding the precise cytoarchitectonic structure of areas 44 and 45.

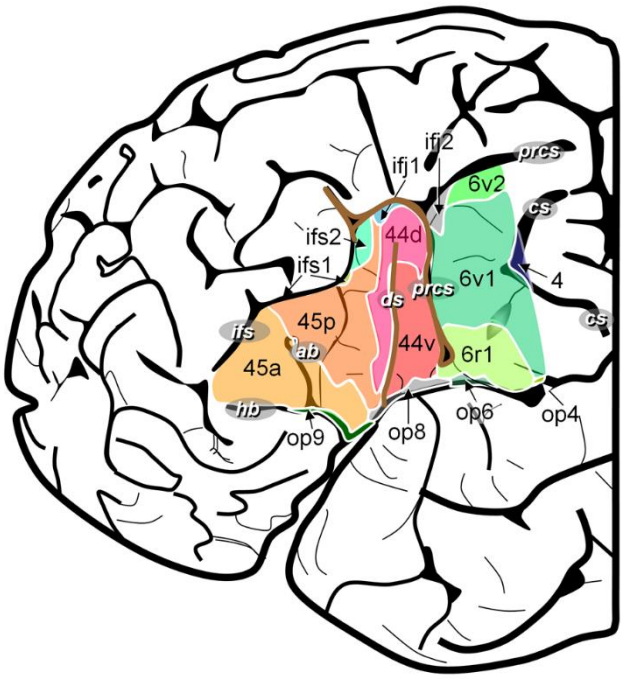

Figure 1: Extent of the receptorarchitectonically delineated areas projected to the lateral surface of an individual post-mortem brain. The figure illustrates the subdivisions of Broca's region (areas 44v, 44d, 45p, 45a), and neighbouring areas 6r1, 6v1, 6v2, Op6, Op8, Op9, ifs1, ifs2, ifj1, ifj2. (Adapted from Amunts et al. (2010))

1.4 Aims of the Dissertation

The present doctoral work aimed to systematically re-map cytoarchitectonic areas 44 and 45 (Amunts et al., 1999) in histological sections of ten post-mortem brains (five male, five female), to identify further subdivisions, and create detailed microanatomical 3D maps that account for intersubject variability and are statistically reproducible. These maps can further serve as an anatomical reference for Broca's region, providing microstructural correlates for the various functional studies, also used for

teaching, and for planning neurosurgical interventions. For this, the cytoarchitecture of Broca's region was quantitatively analysed in ten human post-mortem brains. An observer-independent cytoarchitectonic image analysis, which quantifies the distribution of cell bodies across cortical layers (Amunts et al., 2020; Bludau et al., 2014; Schleicher & Zilles, 1990), was applied to identify local changes in cytoarchitecture in serial histological sections and to define areal borders.

To enable comparisons with functional neuroimaging studies, the microstructural maps were created within a common reference space (MNI Colin27 and MNI152). Intersubject variability substantially affects cytoarchitectonic parcellation and therefore poses a particular challenge, especially in the opercular part of the IFG (Tomaiuolo et al., 1999). Accordingly, probabilistic maps for each area were generated based on the analysis of all ten brains to quantify the variability across individuals. One of the mapped brains was the BigBrain, a model that provides an ultra-high-resolution, cell-level reconstruction of Broca's region in a single brain, allowing precise visualisation of cortical layers and microstructural features. Potential interhemispheric and sex-related differences were studied using areal volumes. Considering the known left-hemispheric language dominance of Broca's region, structural left-right differences were further assessed using Euclidean distance analyses.

To further investigate the functional heterogeneity of the region, peak activation coordinates from the three functional studies (Goucha & Friederici, 2015; Papitto et al., 2024; Zaccarella & Friederici, 2015) were superimposed onto the probability maps of the newly defined subdivisions of Broca's region. Additionally, meta-analytic connectivity modelling (MACM) was performed to examine functional differentiation and connectivity profiles at a broader network level (Eickhoff et al., 2012; Eickhoff et al., 2009; Robinson et al., 2010). Finally, electrocorticography (ECoG) recordings from syllable production tasks were overlaid onto the MPMs of areas 44p, 44a, 45p, and 45a, enabling precise visualisation of task-related cortical activity relative to the newly defined cytoarchitectonic subdivisions.

2. Materials and Methods

2.1 Post-mortem Material and Cytoarchitectonic Analysis Pipeline

The cytoarchitecture analysis was based on the human post-mortem brains of 10 subjects (5 male and 5 female). The subjects (age range: 30-85 years, mean age: 65 years) had no clinical history of psychiatric or neurological diseases. Brains were obtained from the body donor program of the Department of Anatomy at the University Hospital Düsseldorf of the Heinrich Heine University. Ethical approval and documented written informed consent were obtained by legal requirements (Faculty of Medicine, Heinrich Heine University, Düsseldorf, Germany, study number 2023-2632) (Tab. 2).

Brain no.	Sex	Age (years)	Cause of death	Fresh brain weight (g)
BC1	Female	79	Bladder carcinoma	1350
BC3	Male	69	Vascular disease	1360
BC4	Male	75	Acute glomerulonephritis	1349
BC5	Female	59	Cardiorespiratory insufficiency	1142
BC7	Male	37	Right heart failure	1437
BC8	Female	72	Renal failure	1216

BC9	Female	79	Cardiorespiratory failure	1110
BC10	Female	85	Mesenteric infarction	1046
BC20	Male	65	Cardiorespiratory insufficiency, carcinoma of the prostate	1392
BC21	Male	30	Hodgkin's disease, bronchopneumonia, deep vein thrombosis	1409

Table 2 Brain donors' information

The brains were removed less than 24 hours post-mortem, and fixed for a minimum of three to six months in 4% buffered formalin (pH 7.4) or Bodian solution (Amunts et al., 2007). To record their original size and shape, magnetic resonance imaging (MRI) was performed using a 1.5 Tesla scanner (Siemens, Erlangen, Germany) with a T1-weighted 3D Fast Low Angle Shot (FLASH) sequence (flip angle = 40°, echo time = 5 ms, repetition time 40 = ms). Based on these images, histological sections were 3D-reconstructed and corrected (Amunts et al., 2020; Bludau et al., 2014).

After removing the meninges and blood vessels, the brains were embedded in paraffin and sectioned coronally into 20 µm serial slices using a microtome. Every 15th section was mounted on coated slides, and cell bodies were visualised using a modified Merker silver nitrate staining method (Merker, 1983). The stained sections were digitised with flatbed scanners at a resolution of 10 µm, resampled to an isotropic resolution of 20 µm, cropped to a standardised image size, and stored as lossless compressed grayscale images.

Cortical areas were mapped on at least every 60th section, which corresponds to a spacing of 1.2 mm between mapped slices.

2.2 GLI-Based Volume Fraction of Neuronal Cell Bodies

The inferior frontal gyrus (IFG), including its Pars opercularis and Pars triangularis, was identified using the Atlas of Cerebral Sulci (Ono et al., 1990) based on photographs of the lateral brain views. Cytoarchitectonic areas 44 and 45 are located in the IFG and occupy the Pars opercularis and Pars triangularis, respectively (Brodmann, 1909). Area 44 was consistently found on the free cortical surface of the opercular part of the IFG, whereas area 45 was reliably situated on the free cortical surface of the triangular part rostral to the ascending branch of the lateral fissure (Amunts et al., 1999).

Rectangular regions of interest (ROIs) encompassing cytoarchitectonically relevant areas were defined in histological sections. The ROIs were digitised with a CCD camera (AxioCam Mpm, Zeiss, Germany) attached to an optical light microscope (AxioObserver Z1, Zeiss, Germany). The microscope's computer-controlled motorised stage (Axioplan 2 imaging, Zeiss, Germany) and Camera were operated via the Axiovision software (version 4.6, Zeiss, Germany). Images were acquired at a resolution of 1.02 µm per pixel, with an 8-bit greyscale depth, and assembled from individual 524 × 524 µm image tiles captured line-by-line (Schleicher et al., 2000).

The digitised images were converted into Grey Level Index (GLI) images using an internal procedure. For each acquired tile image, a binary image was generated using adaptive thresholding (Castleman, 1979), which accounted for the contrast between darkly stained cell bodies and the lighter neuropil. This process involved filtering the images twice with Gaussian filters of 1 pixel and 40 pixels radii, subtracting the filtered images, and segmenting the result using an individually calculated threshold to generate a binary image. The binary image was subdivided into a grid of 16 × 16 µm measurement fields. For each field, the ratio of neuronal cell bodies to neuropil was calculated and represented as a

grey value. Fields containing no cell bodies were assigned a GLI value of 0 (0%), while fields filled by a cell body were assigned a GLI value of 1 (100%).

The GLI maps reflect the relative neuronal cell density at each location within the microscopic image. The advantage of the GLI approach lies in its reliance on cell packing density rather than staining intensity, reducing the influence of variability in histological staining. Although glial and epithelial cells are also stained, their density variations are minimal and do not significantly affect the analysis (Wree et al., 1982).

Mean GLI values were obtained from 15 profiles per histological section, across three sections for each brain, hemisphere, and cortical area. These GLI values served as the basis for analysing sex-specific, interhemispheric, and interareal differences in the volume fractions of neuronal cell bodies within the areas 44p, 44a, 45p, and 45a. A lower cell-body volume fraction indicates a greater proportion of neuropil - composed of synapses, dendrites, and axons – relative to the volume occupied by neuronal and glial perikaryal. Statistical analyses were conducted using a mixed-design ANOVA at a significance level of $\alpha = 0{,}05$. The within-subject factors included cortical area and hemisphere, while the between-subject factor was sex, as described in Section (Analysis of Volumes of the Areas).

2.3 Observer–independent Cortical Border Detection and GLI Profile Analysis

Within each ROI, the fraction of neuronal cell body volume was estimated along the cortical depth using the described above GLI method. In each GLI image, the outer contour line was placed at the border between cortical layers I and II, and the inner contour line at the border between layer VI and the underlying white matter. Between these contours, curvilinear traverses perpendicular to the laminar structure were calculated using a physical model based on electrical field lines (Jones et al., 2000) (Fig. 2 panels A-C) illustrate this workflow.

GLI values were extracted along each traverse from the cortical surface to the white matter and compiled into density profiles. To improve the signal-to-noise ratio, the GLI images were smoothed using anisotropic filtering. All profiles were normalised to 101 data points to account for interindividual differences in cortical thickness. Each profile was described by a 10-dimensional feature vector comprising the mean GLI value, the standard deviation, the cortical depth of the centre of gravity, skewness, kurtosis, and the corresponding parameters from the first derivative of the profile (Schleicher et al., 2000).

For each cortical area, 15 profiles were extracted at three positions in each hemisphere and averaged to produce a mean profile per area per subject. The resulting mean profiles were then averaged across all subjects. Panel D of Figure 1 shows an inverted GLI image with a statistically significant border between areas 44p and 44a.

For statistical detection of cortical borders, adjacent blocks of profiles were compared using the Mahalanobis distance (MD) (Mahalanobis et al., 1949; Schleicher et al., 2000). Profile blocks contained between 8 - 24 profiles. The blocks were shifted along the cortex in single-profile steps (sliding window method), and the MD between each pair of adjacent blocks was calculated:

$$\mathbf{Di2 = (xi - xi+1)' \; Ci,i+1-1 \; (xi - xi+1)}$$

Where **xi** and **xi+1** are the mean feature vectors of the two profile blocks, and **Ci,i+1-1** is the inverse of their pooled variance-covariance matrix.

Local maxima of the MD function indicate positions where the compared blocks differ most strongly in their laminar patterns, suggesting a potential border between cortical areas. Each maximum was tested for statistical significance using Hotelling's T2-test with the Bonferroni correction ($p \leq 0.001$).

Only those maxima that occurred at similar positions across at least three adjacent sections and for at least three different block sizes were accepted as true borders. Panels E and F of Figure 2 illustrate the detection of a significant maximum and its replication across block sizes.

This observer-independent method relies on the principle that each cortical area has a characteristic laminar pattern of cell density that differs significantly from that of its neighbouring areas. By quantifying these differences statistically, reproducible and objective delineations of cortical borders can be achieved.

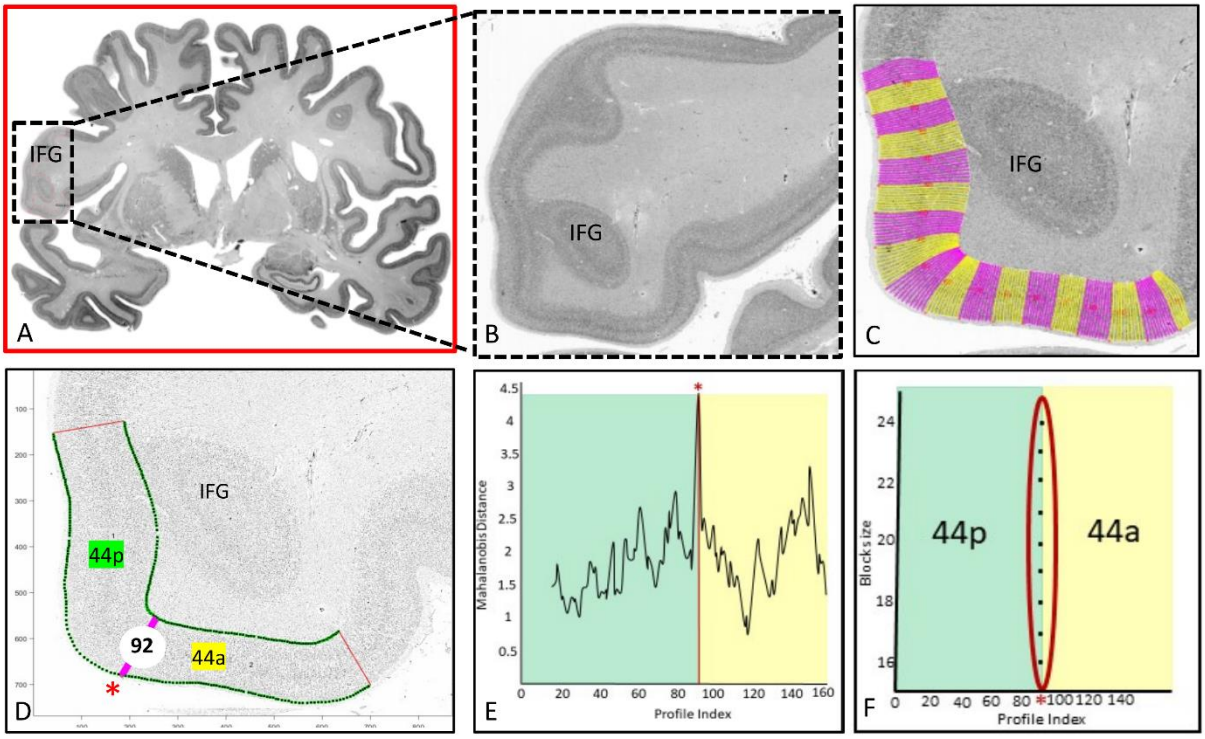

Figure 2 Observer-independent Mapping Approach. (A) Cell-body-stained section (scale: 1 cm) with the region of interest (ROI). (B) ROI defining the examined cytoarchitectonic area on the Inferior Frontal Gyrus (IFG). (C) ROI with outer and inner contour lines and traverses (pink and yellow) (scale: 400 µm). (D) Inverted GLI image of the ROI with a statistically significant border (pink line) between areas 44p and 44a (scale 400 µm). (E) Statistically significant maximum (asterisk) in the Mahalanobis distance function for one block size. (F) Positions of significant maxima across different block sizes.

2.4 Multidimensional Scaling and Cluster Analysis

To visualise the architectural similarities and differences between cortical areas, a multidimensional scaling (MDS) analysis was performed. It is important to note that due to the very dark staining (BC 1) of one of the brains, an additional brain[2] was mapped and used for the multidimensional scaling and cluster analyses. For this purpose, feature vectors were extracted from 45 GLI profiles per area, obtained from three histological sections per hemisphere, and then averaged across hemispheres. The shape of these GLI profiles, and consequently the descriptive mathematical features derived from them, characterises and quantifies the cytoarchitecture of each brain area. A 10-dimensional feature vector described each GLI profile. The feature vectors were used to calculate pairwise Euclidean distances between areas via MATLAB's *pdist* function. The *mdscale* function was then applied to generate a two-dimensional representation of these distances. The resulting MDS plot provides a descriptive visualisation of the inter-areal relationship: a low Euclidean distance between two areas

[2] BC 12, 43 years, female, pulmonary embolism

indicates high cytoarchitectonic similarity and suggests that they belong to the same group, whereas a high Euclidean distance indicates cytoarchitectonic dissimilarity and suggests different groups.

The hierarchical cluster analysis was also based on the Euclidean distance between the mean feature vectors of the areas, following the approach described by (Bacher et al., 2010). Ward's linkage algorithm (Ward, 1963) was applied to the group areas into clusters of similar cytoarchitecture. In addition, an unrooted tree representation was generated using the program SplitsTree126 (Huson & Bryant, 2006) with UPGMA (unweighted pair-group method with arithmetic mean) as the linkage method, providing an alternative view of the relationships between areas.

Additionally, the Euclidean distance between the feature vectors of the areas of the left and right hemisphere was calculated in Python, for each of the new cytoarchitectonic brain areas, together with their neighbouring areas. Results were visualised using box plots.

2.5 Analysis of Volumes of the Areas

The volumes of cytoarchitectonic areas 44p, 44a, 45p, and 45a were calculated using the number of sections between successive delineations, the physical section thickness, the pixel dimensions of the digitised images, the measured area in pixels across all relevant sections, and an individual shrinkage correction factor.

Specifically, the formula applied was:

$$V = s * T * x * y * \sum A_i * F$$

Where V - calculated volume (mm^3), s – the number of sections between mapped sections (s = 60 in the present study), T = section thickness (20 µm), x, y = pixel length and width (21,2 µm) $\sum A_i$ = the sum of measured area in pixels across all analysed sections, and F = the individual shrinkage correction factor. This factor was determined as the ratio of the fresh brain volume to the volume after histological processing, multiplied by the mean specific density of 1.033 g/mm^3. In this way, differences in shrinkage due to factors such as age, sex, pathology, or histological preparation were compensated for (Amunts et al., 2007; Amunts et al., 2005; Zilles et al., 1988).

To account for variation in overall brain size, the calculated area volumes were normalised to the total volume of the respective brain. Interhemispheric and sex-related differences in the volumes were assessed using a mixed ANOVA, with area and hemisphere as within-subject factors and sex as a between-subject factor. The assumptions of normality and sphericity were tested using the Shapiro-Wilk and Mauchly tests, respectively, while the homogeneity of error variances was evaluated using Levene's test. A significance level of $\alpha = 0,05$ was applied for all statistical tests.

2.6 3D Reconstruction of the Areas

For the three-dimensional (3D) reconstruction, areas 44p, 44a, 45p, and 45a were initially outlined interactively in high-resolution scans of the corresponding histological sections using the in-house Online Section Tracer tool. Histological processing inevitably causes tissue deformations and shrinkage due to fixation, embedding, sectioning, and staining (Amunts et al., 2020). If left uncorrected, these distortions could undermine the spatial accuracy of the reconstructed cortical areas. Therefore, before the actual reconstruction, the outlined sections were co-registered to two complementary reference datasets: (i) a 3D structural magnetic resonance imaging (MRI) dataset of the fixed post-mortem brain acquired before sectioning, which provides a geometrically accurate reference, and (ii) high-resolution flatbed scans of the stained histological sections containing detailed cytoarchitectonic information. The MRI dataset served as a structural template, while the histological scans preserved microstructural detail. The alignment of these datasets was performed using in-house software that applied both linear

and nonlinear spatial transformations. This process enabled the correction of section-specific distortions and ensured that the reconstructed cortical areas accurately reflect both the true anatomical shape of the brain and the precise location of the cytoarchitectonic borders (Amunts et al., 2020).

2.7 Generation of Probability Maps

The cortical areas of the ten reconstructed brains were normalised to the anatomical reference brains MNI Colin 27 and ICBM152casym (Evans et al., 2012) using a combination of linear and nonlinear elastic transformations within a multiscale registration framework (Amunts et al., 2020). By superimposing the delineated areas from the ten individual brains in both reference spaces, a probabilistic map (p-map) was generated for each area in stereotaxic space (Amunts et al., 2020). These maps represent intersubject variability, with probability values ranging from 10% to 100%, and a colour gradient (from blue to red) indicating the degree of overlap and the proportion of individuals in whom a specific cortical area is present at each voxel within the reference brain.

These probabilistic maps served as the basis for generating a maximum probability map (MPM) for the areas 44p, 44a, 45p, and 45a. The MPM is a continuous, non-overlapping map in which each voxel is assigned to the cytoarchitectonic area with the highest probability at the location (Eickhoff et al., 2005). For both reference spaces, the centre of gravity (centroid) of each area was calculated. The MPM includes the newly identified cytoarchitectonic areas 44p, 44a, 45p, and 45a, as well as the adjacent regions.

The respective area representations and their descriptions were made publicly available in the Julich-Brain Cytoarchitectonic Atlas (https://julich-brain-atlas.de) and in the EBRAINS research infrastructure (https://ebrains.eu/service/human-brain.atlas)

2.8 3D Reconstruction of the Areas 44p, 44a, 45p, and 45a in BigBrain

BigBrain is an ultra-high-resolution 3D model of a post-mortem human brain (Amunts et al., 2013; Amunts et al., 2020). The BigBrain dataset is based on 7,404 cell-body-stained, three-dimensionally reconstructed histological sections. It provides detailed structural insights into the human brain and its regional heterogeneity, with a nearly cellular resolution of 20 × 20 µm per pixel (Amunts et al., 2013). Ultra-high-resolution maps of the newly identified areas in BigBrain space were created using a deep learning-based brain mapping tool that utilises convolutional neural networks (CNNs) (Schiffer et al., 2021). This tool has been previously tested and validated on several cytoarchitectonic areas (Brandstetter et al., 2021; Kiwitz et al., 2022; Kiwitz et al., 2020). The new areas were manually delineated on at least every 15th section of the high-resolution, digitised BigBrain scans (Amunts et al., 2013). A total of 53 annotated training sections were used for the areas 44p, 44a, 45p, and 45a in both the left and right hemispheres of the BigBrain dataset. Using these training sections, the CNN-based brain mapping tool was trained via a web-based interface (Schiffer et al., 2021) on the JURECA supercomputer at the Jülich Supercomputing Centre (Krause & Thörnig, 2018). The model learned to interpolate area boundaries between the manually labelled training sections. Following training, the model automatically predicted 1,650 histological sections, generating continuous 2D segmentation maps for the areas throughout the brain (Fig. 3). These automatically generated maps were subjected to rigorous quality control, and sections of insufficient quality were excluded from further processing. Following quality control, the segmentation maps were transformed into 3D-reconstructed histological BigBrain space using nonlinear registration of the digitised 1 µm sections and existing transformation parameters (Amunts et al., 2013; Omidyeganeh et al., 2020). This process enabled the generation of 3D volumetric representations of the areas at a resolution of 20 µm.

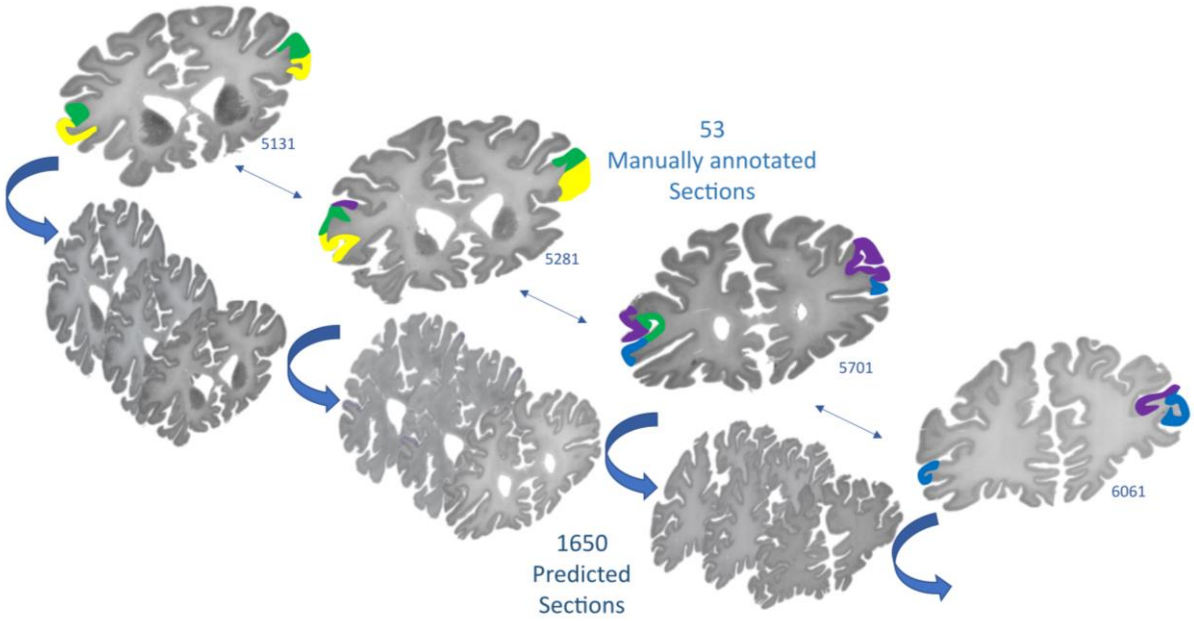

Figure 3 Ultra-high resolution 3D reconstruction of Cytoarchitectonic areas in the BigBrain. A deep-learning model was trained on 53 manually delineated histological sections to identify Broca's region areas 44p, 44a, 45p, and 45a across the remaining 1650 sections. All resulting annotations were verified and transformed into the 3D reconstructed BigBrain.

In this step, we additionally employed CytoNet (Schiffer, 2025), a foundational model for cytoarchitectonic feature extraction, to predict and fill in missing or excluded sections during the 3D reconstruction process. Trained on high-resolution histological data, CytoNet uses a self-supervised learning strategy that captures local architectural similarity to infer plausible representations of cortical microstructure. In our workflow, CytoNet was applied to generate segmentation maps for the missing sections, using neighbouring image context along the cortical ribbon. These predictions were integrated with the CNN-based segmentations to ensure continuity and consistency across the entire volume. Missing sections reconstructed by CytoNet were validated through visual inspection and alignment with adjacent manually annotated slices. This approach enabled anatomically consistent 3D representations of the cortical areas. After integration of the CytoNet-based predictions, the resulting 3D volumes were smoothed using a 3D median filter to address residual segmentation noise. The largest contiguous components were identified and retained as the final area volumes, while false-positive or disconnected voxels were excluded. For each cytoarchitectonic area, we generated both 3D surface models and corresponding 2D segmentations overlaid on histological sections (Schiffer et al., 2021). The results are also publicly available in the Julich Brain Atlas[3], on the EBRAINS research infrastructure[4].

2.9 Comparison of Activation Coordinates in Common Stereotaxic Space

To visualize activation peaks as reported in functional studies from the Department of Neuropsychology in Leipzig at the Max Planck Institute for Human Cognitive and Brain Sciences, and to compare them with new cytoarchitectonic maps in MNI space (ICBM 152 non-linear asymmetric 2009c), we used MATLAB (MATLAB R2009a; MathWorks Inc., MA, USA), the Statistical Parametric Mapping (SPM12) software package and an in-house MATLAB script, which can be found on GitHub[5].

[3] https://julich-brain-atlas.de
[4] https://ebrains.eu/service/human-brain.atlas
[5] https://github.com/INM-1-FZJ-Cytoarchitecture/Figure_Template_Brain_with_coords

Probabilistic assignment of activation peaks to cytoarchitectonic areas was conducted using the Siibra explorer[6] assignment function, applying a pmap threshold of p = 0.2 to account for interindividual variability (Dickscheid et al., 2025). To functionally validate our new cytoarchitectonic subdivisions of Broca's region, comprising four distinct areas within BA44 and BA45, we mapped peak activation coordinates from functional neuroimaging studies focusing on hierarchical syntactic processing, semantic integration, and action grammar (Goucha & Friederici, 2015; Papitto et al., 2024; Zaccarella & Friederici, 2015). Given the substantial heterogeneity in theoretical framework and experimental designs across language neuroscience laboratories, studies from the Department of Neuropsychology in the Max Planck Institute for Human Cognitive and Brain Sciences, led by Angela Friederici, were considered particularly well-suited for this analysis. This decision was based on the lab's consistent theoretical focus, precise task design targeting core language components, and close alignment with cytoarchitectonic mapping efforts. Their work offers high methodological compatibility with the goals of this study and provides reliable functional data for assessing the structure-function relationship of the new areas of Broca's region. While the primary focus of this thesis is the mapping of language-related activations to the newly defined subdivisions of Broca's region, additional anatomical context was provided by the recent cytoarchitectonic parcellation of the adjacent premotor cortex by Ruland and colleagues (Ruland et al., 2025). Notably, during the analysis of peak activations from the three key functional studies mentioned above, it was observed that some activation foci originally reported as falling within area 44 in MNI space were more accurately assigned to area 6r1 in our updated cytoarchitectonic maps. Given the cytoarchitectonic and functional similarities between areas 6r1 and 44p, this finding suggests a potential overlap or misattribution in earlier studies, highlighting underscoring the importance of using high-resolution anatomical maps for functional interpretation. These observations support a more refined view of the inferior frontal and premotor cortex in the context of language processing, especially for domains involving syntactic structuring and action-related components.

2.10 Functional Characterisation of the Newly Delineated Areas (44p, 44a, 45p, and 45a)

The functional and connectivity analyses of the cytoarchitectonic areas 44p, 44a, 45p, and 45a were conducted using a comprehensive meta-analytic framework combining cytoarchitectonic MPM-based seed areas, MACM with ALE meta-analysis, behavioural decoding, cytoarchitectonic assignment via Siibra, and visualisation in SurfIce using the MNI 152 2009c (curv) template. This integrative approach allowed for the systematic investigation of functional connectivity patterns and behavioural associations of the subregions within Broca's region, thereby linking microstructural differentiation with large-scale functional organisation.

2.10.1 BrainMap Database and Data Extraction

To investigate the functional roles of the newly delineated cytoarchitectonic areas, we employed a quantitative functional characterisation approach based on Maximum Probability Maps (MPMs) derived from histological analyses (See section: Generation of Probability Maps). These MPMs were used to extract activations reported in functional neuroimaging studies from the BrainMap database (www.brainmap.org). At the time of analysis, the BrainMapDatabase contained 4,341 publications, 22,302 experiments, 112,160 subjects, 169,986 reported activation foci, and 115 paradigm classes, providing a comprehensive basis for large-scale meta-analytic modelling.

MPMs for each region were imported into Sleuth (v.3.0.4), the BrainMap query interface. Sleuth performs region-of-interest (ROI) – based searches by identifying all experiments that include at least one reported activation focus falling within the voxel-defined extent of the ROI. When an MPM mask

[6] https://ebrains.eu/data-tools-services/tools/siibra-python

is loaded, sleuth automatically checks each experiment's stereotactic coordinates against the mask, returning only those experiments with empirical activation inside the cytoarchitectonic area. The search was restricted to studies conducted with healthy participants, and only activations (not deactivations) were included. For each area, Sleuth provided the total number of eligible studies, the associated experimental metadata, and the full list of activation foci, which were exported from meta-analytic connectivity modelling (MACM).

Each experiment in BrainMap is associated with a rich, standardized set of metadata based on BrainMap taxonomy of Behavioural Domains (e.g., cognition, action, perception, emotion, interoception). This controlled vocabulary enables consistent functional annotation across diverse neuroimaging studies and forms the basis for forward and reverse inference analyses. These metadata were used later for functional characterisation of each cytoarchitectonic area's activation profile.

2.10.2 Meta-Analytic Connectivity Modelling (MACM)

To assess the functional connectivity (Friston, 1994) of each cytoarchitectonic area, Meta-Analytic Connectivity Modelling (MACM) was performed (Robinson et al., 2010). MACM aims to find brain areas that reliably co-activate with a chosen seed region in numerous neuroimaging studies. Such co-activation patterns can be interpreted as indicators of task-based functional connectivity derived from meta-analytic data. Each cytoarchitectonic area (44p, 44a, 45p, and 45a) served as an independent seed region, analysed separately for the left and right hemisphere. For each seed, all experiments in the BrainMap database reporting at least one activation focus within the seed region were identified, and all activation coordinates from those experiments were extracted. These data served as the empirical basis for the subsequent meta-analysis.

2.10.3 Activation Likelihood Estimation (ALE) Meta-Analysis

The extracted activation coordinates were analysed using the Activation Likelihood Estimation (ALE) approach implemented in GingerALE (v 3.0.2) (Eickhoff et al., 2012; Eickhoff et al., 2009; Turkeltaub et al., 2012). The ALE method models each reported activation focus for a three-dimensional Gaussian probability distribution, representing spatial uncertainty that arises from inter-individual and methodological variability. The width of each Gaussian kernel (full-width at half maximum, FWHM) was empirically determined as a function of the study's sample size (Eickhoff et al., 2009), such that studies with larger participant numbers contributed more precise spatial estimates.

For each experiment, Modelled Activation (MA) maps were computed by combining all Gaussian-modelled foci from that experiment. Subsequently, MA maps from all experiments were merged to produce an ALE map. Reflecting the voxel-wise likelihood of activation convergence across the included studies.

To distinguish true convergence from random spatial overlap, statistical inference was performed using a permutation-based test. The resulting ALE maps were thresholded at a voxel-level cluster-forming threshold of $p < 0.001$, and significant clusters were determined using family-wise error (FEW) correction at the cluster level ($p < 0.05$). A minimum cluster size of 100 mm^3 was applied to ensure spatial robustness. The final thresholded ALE maps represent brain regions showing significant convergence of co-activation across studies, thus revealing the functional connectivity profile of each cytoarchitectonic area.

2.10.4 Behavioural Decoding

To determine the behavioural relevance of the identified co-activation patterns, the associated behavioural metadata were analysed using the BrainMap behavioural taxonomy. For each cytoarchitectonic area, the distribution of behavioural domains (e.g., cognition, language, perception, emotion) linked to the identified studies was compared to the overall behavioural distribution of the

entire BrainMap database. This comparison was performed using a binomial test, corrected for multiple comparisons using the Bonferroni method ($p < 0.05$), following the procedure described by (Eickhoff et al., 2010). This analysis enabled inference about behavioural functions that were significantly overrepresented among the studies activating each cytoarchitectonic area, thereby allowing a data-driven functional characterisation.

2.10.5 Anatomical Assignment

For anatomical assignment of the significant ALE clusters, we used the Julich-Brain Atlas via the Siibra (Scalable Interactive Interface for Brain Atlases) framework (Amunts et al., 2020). Thresholded ALE maps generated with GingerALE were exported in NIfTI format and processed in Python using Siibra. Queries to the probabilistic cytoarchitectonic maps of the Julich-Brain Atlas (version 3.1) yielded, for each activation cluster, a set of quantitative indices describing the spatial relationship between the ALE cluster and each cortical or subcortical area.

For every MACM cluster, Siibra returned three key metrics:

1. Map value – the maximum probability of a cytoarchitectonic area within the ALE cluster.
2. Map containedness – the proportion of the cytoarchitectonic area included within the cluster.
3. Input containedness – the proportion of ALE cluster contained within the cytoarchitectonic area.

These measures allow a precise, quantitative characterisation of anatomical overlap. Based on these metrics, cytoarchitectonic regions were classified as overlapping or non-overlapping between pairs of MACM-derived clusters. To ensure interpretability and to reflect differences in data distribution across regions, we applied comparison-specific thresholds for map containedness. The exact thresholds used for each comparison are listed in the corresponding supplementary tables (Tables 1-21). Thresholds ranged from map containedness > 0.01 – 0.50 and input containedness > 0.01 – 0.50, depending on the specific region pair being compared (e.g., 6r1-44p, 44p-45p, 44a-45a, and their left/right hemispheric variants).

All anatomically assigned regions – including overlapping and uniquely assigned areas – were exported as supplementary tables. Each table lists, for every MACM input cluster, the cytoarchitectonic area, map value, map containedness, input containedness, and the originating input region. This workflow ensured reproducible, high-resolution anatomical mapping grounded in state-of-the-art cytoarchitectonic reference data.

2.10.6 Visualisation of Results

For visualisation of the ALE results and functional connectivity patterns, Surf Ice (https://www.nitrc.org/projects/surfice/) was used. The resulting ALE maps were projected onto three-dimensional cortical surfaces for visualisation of the spatial distribution and overlap of co-activation clusters. Visualisations were rendered on the MNI 152 2009c (curv) surface template, which provides a high-resolution representation of cortical folding and curvature. Both inflated and semi-transparent surface views were used to illustrate the localisation of significant clusters within Broca's region and surrounding cortical areas. This visualisation approach facilitated intuitive assessment of inter-regional connectivity and spatial organisation across the analysed cytoarchitectonic areas.

In summary, the functional and connectivity analyses of the cytoarchitectonic areas 44p, 44a, 45p, and 45a were conducted using a comprehensive meta-analytic framework combining cytoarchitectonic MPM–based seed definitions, MACM with ALE meta-analysis, behavioural decoding, cytoarchitectonic assignment via Siibra, and visualisation in Surf Ice using the MNI152 2009c (curv) template. This integrative approach allowed for the systematic investigation of functional connectivity patterns and

behavioural associations of the subregions within Broca's region, thereby linking microstructural differentiation with large-scale functional organisation.

2.11 Overlay Registration of the MPMs of Areas 44p, 44a, 45p, and 45a onto Task-Evoked Electrocorticography Activity

The MPMs of areas 44p, 44a, 45p, and 45a were loaded as contours into the MNI ICBM 152 asym 2009 reference space volume. The volume was cropped to the left hemisphere to focus on relevant cortical areas. Both the MPMs and the template volume were visually aligned using the software Napari through manual rotation and translation, ensuring optimal correspondence with the left-lateral MNI template used in Liu et al. (2025). Electrode positions were indicated as red crosses. (Fig. 33 A-B). Electrocorticography (ECoG) recordings were obtained while patients performed syllable production tasks, with and without cortical stimulation. To integrate functional data with anatomical maps, volume slices of the MPMs were projected onto the MNI-lateral image from lateral to medial direction. Task-related activity was represented using kernel density estimates, with red indicating articulatory complexity and blue indicating sequence complexity. ROIs were further examined by creating zoomed views of the overlays. These allowed visualisation of the overlap between MPM contours and electrode signals, with saturated colours applied to improve contrast and visibility. ROIs were displayed in three forms: (1) with MPM contours (Fig. 33 D), (2) without MPMs (Fig. 33 E), and (3) electrode signals only (Fig. 33 F).

Data and code: The analyses were performed using the dataset published on **Zenodo** (https://doi.org/10.5281/zenodo.15346719) and the code hosted on **GitHub** (https://github.com/ChangLabUcsf/Liu2025_Sequencing), as referenced in Liu et al. (2025). These resources were used to generate electrode-brain overlays and to recreate kernel density estimates for the pre-speech visualisation.

3. Results

Cytoarchitectonic mapping of Broca's region revealed four subdivisions: posterior (44p, 45p), and anterior (44a, 45a), distinguished by laminar architecture and GLI profiles. Posterior areas exhibited broader supragranular layers and smoother white-matter transitions, whereas anterior areas displayed denser granular layers and sharper laminar borders. Euclidean distance analyses showed that left-right cytoarchitectonic differences varied systematically across Broca's region subdivisions. Area 44a showed small and consistent hemispheric differences, whereas area 44p showed slightly bigger and markedly more variable differences. Area 45a displayed the strongest descriptive lateralisation overall, while area 45p had the lowest median but the greatest inter-individual variability. Overall, posterior subdivisions (44p, 45p) were characterised by higher variability, and anterior subdivisions (44a, 45a) by more consistent patterns, with the strongest lateralisation occurring in area 45a and moderate lateralisation in area 44p. The three-dimensional reconstructions across ten brains confirmed a caudo-rostral arrangement of subdivisions, with surface projections influenced by sulcal variability, including the presence or absence of the diagonal sulcus (DS). Based on the 3D reconstructions of all ten brains, pmaps and MPMs were calculated in a common stereotaxic space (Colin27). One of the brains was the BigBrain model, where all 1650 sections where the areas were present were 3D reconstructed at ultra-high resolution with the help of CNN.

Functional mapping using three complementary approaches highlighted distinct roles for posterior versus anterior subdivisions. First, peak activation coordinates from independent fMRI studies were overlaid onto the cytoarchitectonic maps, showing that in the left hemisphere, syntactic and semantic activations predominantly overlapped with 44p, 44a, and 45a, whereas lexical/phonological processing involved ventral 44a and adjacent opercular regions; action-related activations engaged premotor and

frontal opercular areas. The right hemisphere included fewer peaks, mainly in premotor areas, 44p, and the insula. Second, BrainMap meta-analytic functional characterisation confirmed domain-general cognitive involvement across all subdivisions, with posterior areas (44p, 45p) displaying balanced bilateral engagement while anterior areas (44a, 45a) were largely symmetric. Third, MACM analyses revealed partially overlapping but distinct co-activation networks: posterior 44p and 45p shared a frontal-insular-precentral core, with 44p uniquely co-activating posterior parietal and thalamic regions and 45p engaging limbic and medial temporal structures. Anterior 44a and 45a shared fronto-parietal-thalamic networks, with 44a uniquely recruiting intraparietal and multiple thalamic nuclei and 45a engaging fronto-opercular, premotor, and occipital areas. Overlapping the MPMs of areas 44p, 44a, 45p, and 45a with task-evoked ECoG data further demonstrated that speech-related activity is largely localised outside of Broca's region, predominating in PM, with only limited involvement of ventral area 44a and 44p for sequence complexity. Together, these findings demonstrate that cytoarchitectonic differences between posterior and anterior subdivisions correspond to distinct structural, volumetric, and functional profiles, with posterior areas showing higher bilateral similarity and anterior areas exhibiting specialised, lateralized connectivity patterns.

3.1 Cytoarchitecture of Broca's Region Areas 44p, 44a, 45a, 45p

The new areas display a characteristic six-layered cortical structure, including a visible layer IV, consistent with the organisation of the isocortex. At the same time, the expression of layer IV differed between the areas that belong to the granular or disgranular type. Previous cytoarchitectonic studies from our lab (Amunts et al., 1999) demonstrated that Broca's region can be reliably subdivided into two main areas corresponding to Brodmann areas 44 and 45. They also reported that both areas are internally heterogeneous, with additional cytoarchitectonic borders within each area (Amunts et al., 1999).

Building on these observations, the present study further refines Broca's region into four distinct areas: 44p, 44a, 45p, and 45a. Each area exhibits a characteristic laminar architecture and a unique Grey Level Index (GLI) profile, enabling reliable differentiation between them and from adjacent cortical regions. Within this broader organisation, area 44 is dysgranular, characterised by a poorly defined layer IV caused by the intermingling of granular cells from layer IV with pyramidal cells from layers III and V. In contrast, area 45 is granular, showing a well-developed and more sharply delineated granular layer IV (Amunts & Zilles, 2012).

The four subdivisions show distinct laminar features, neuronal densities, and transitions to the underlying white matter. The following sections describe the characteristic cytoarchitecture of each subdivision.

Area 44p (Fig. 4A) was characterised by a broad supragranular compartment, with large pyramidal neurons concentrated in sublayer IIIc, giving it a robust upper-layer structure. Layer IV was relatively broad but sparsely populated, while layer V contained medium-to-large pyramidal cells at moderate density. The deep layer showed a gradual transition to white matter, reflected in a smooth decline of GLI values.

Area 44a (Fig. 4B) showed a thin layer IV, and a less packed supragranular compartment with smaller pyramidal cells concentrated in IIIc. Layer V was thinner but slightly more populated than in 44p, and the transition to white matter was sharp as compared to 44p.

Area 45p (Fig. 4C) displayed higher cell density in the upper layers, particularly in layer II, and a broad, homogeneously packed layer III with large pyramidal neurons in IIIc. Layer IV was moderately developed, forming a clear granular ribbon, while layer V was subdivided into sparse Va and a denser Vb within larger pyramids. The deep layer VI transitioned smoothly into white matter.

Area 45a (Fig. 4D) had an even higher density of pyramidal neurons in IIIb-c, a broader layer IV with more granular cells, and a sharply defined transition to white matter in layer VI, distinguishing it as the most granular of the four subdivisions.

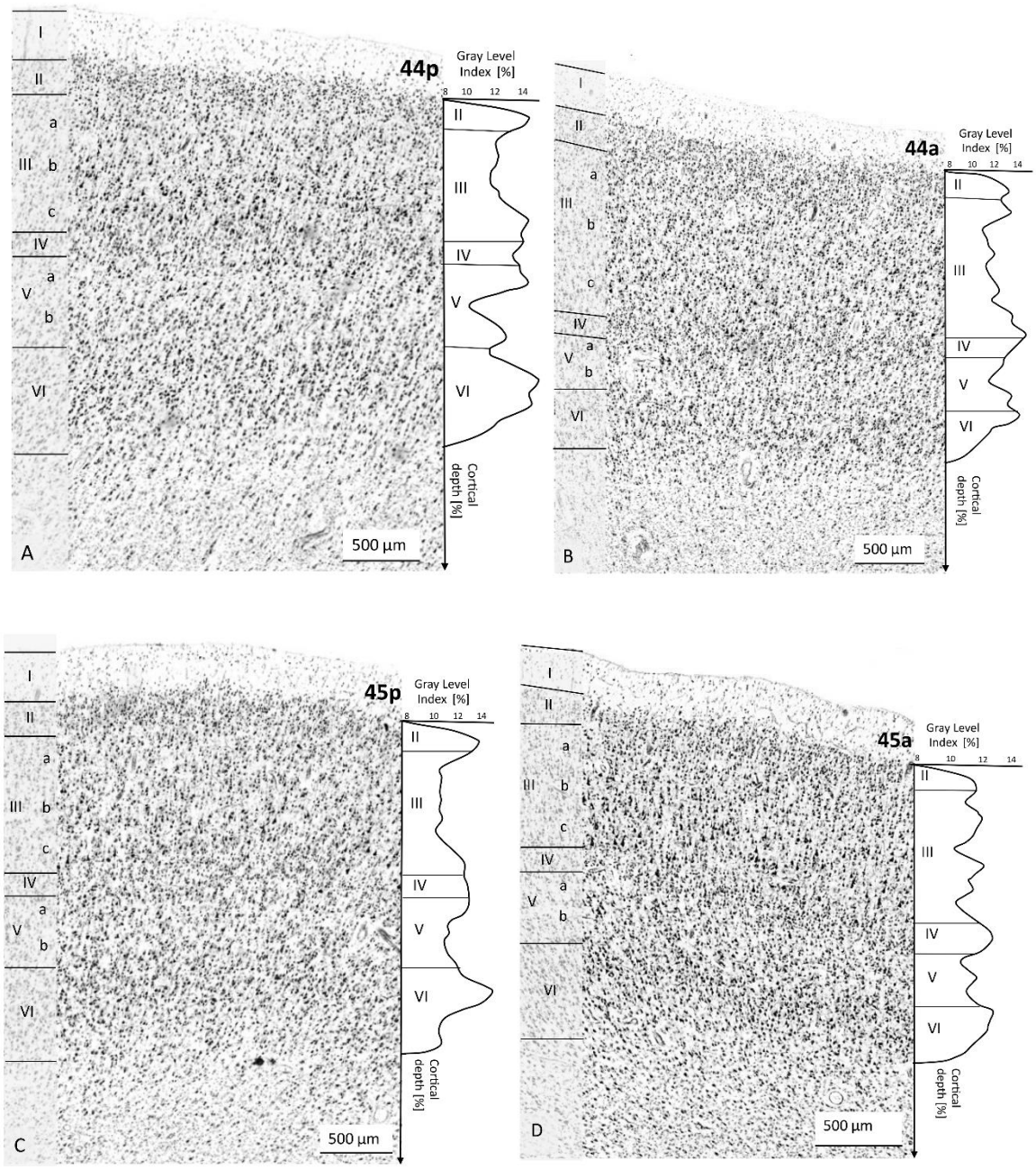

Figure 4 Cytoarchitecture of areas 44p, 44a, 45p, and 45a with corresponding GLI profiles. Shown are cell-body-stained coronary sections of areas 44p, 44a, 45p, and 45a with their corresponding GLI (Grey Level Index) profiles. Cell density is indicated in percent. Roman numerals denote the cortical layers, and black lines mark the layer boundaries. The disgranular areas 44p and 44a show a less distinct layer IV, whereas the granular areas 45p and 45a exhibit a more clearly defined internal granular layer IV. Across all areas, differences can be observed in the cell-packing density of layers II and V and in the sharpness of the boundary between layer VI and the white matter.

3.2 Borders Within Areas 44 and 45

Cytoarchitectonic analysis supported by statistical analysis revealed significant borders within areas 44 and 45(Fig. 5). These borders were identifiable based on characteristic changes in the laminar composition and neuronal density patterns.

The border between 44p and 44a (Fig. 5A) was defined primarily by differences in the organisation of the supragranular and infragranular layers. Area 44a contained a higher density of neurons in layers IIIb-c and showed an increased number of cells in layer Vb. In contrast, area 44p exhibited a greater neuronal density across all subdivisions of layer III (IIIa-b) and a more homogeneously populated layer V. The transition between layer VI and the white matter was broader in 44a, whereas 44p showed a sharper, more abrupt border, indicating a clear laminar shift between the two subdivisions.

The border between areas 45p and 45a (Fig. 5B) was characterised by differences in the granular and supragranular layers. Area 45p displayed a well-developed layer IV, along with a higher density of neurons in layers IIIb-c and a moderate transition from layer VI into white matter. In comparison, area 45a exhibited a broader and more cell-dense layer IV, with pyramidal neurons distributed across layers II a-c, and a sharper transition of layer VI into the white matter.

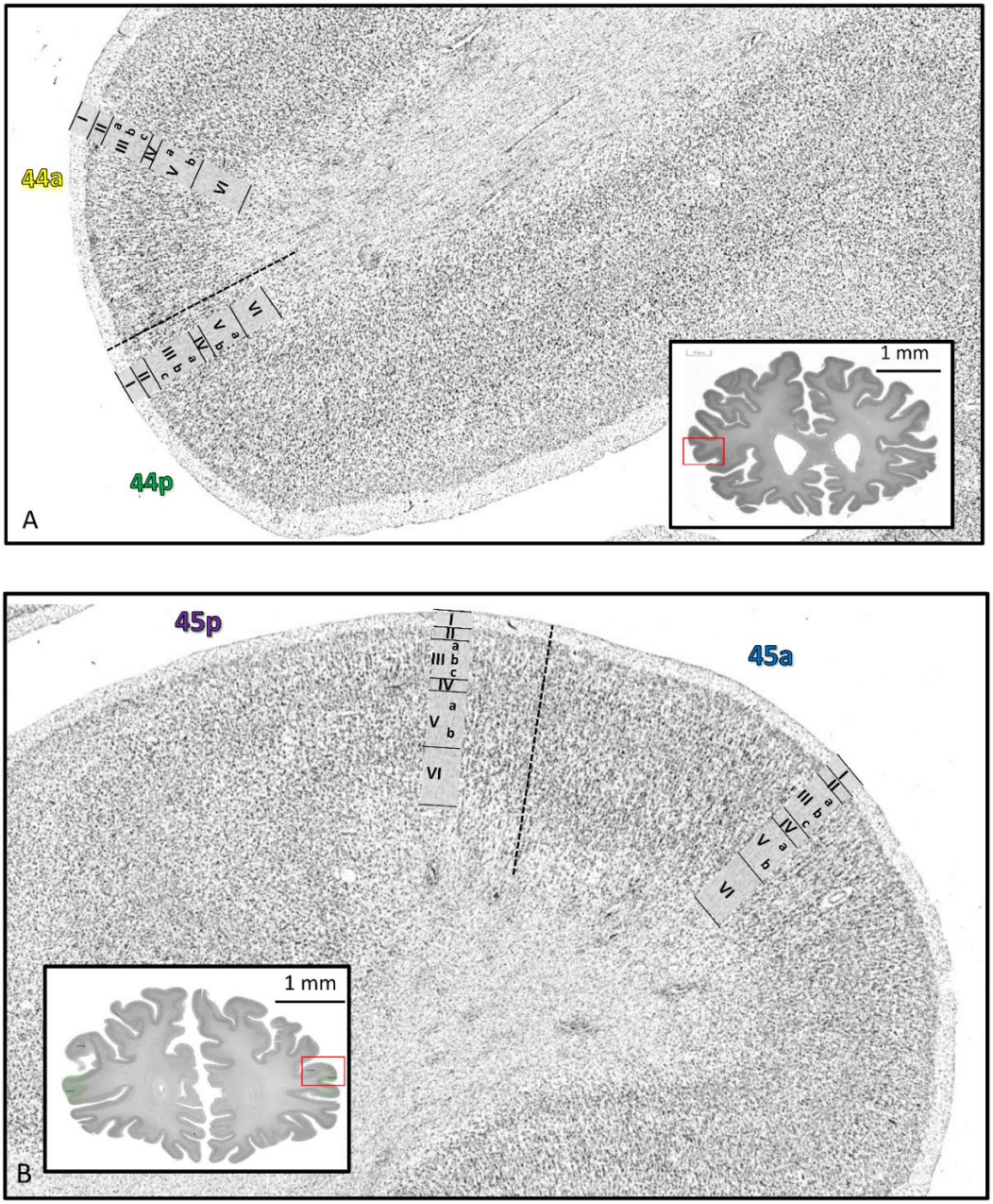

Figure 5 Cytoarchitectonic borders of areas 44a/44p and 45p/45a. (A) Area 44a shows more cells in layers IIIb-c, a denser layer Vb, and a broad layer VI-white matter transition than 44p. Area 44p has a higher amount of cells in layer III, a more evenly populated layer V, and a sharper VI-white matter transition. (B) Area 45p exhibits a distinct layer IV, more cells in IIIb-

c, and a moderate VI-white matter transition, while area 45a shows a broader layer IV, pyramidal cells across IIIa-c, and a sharper VI-white matter transition.

3.3 Neighbouring Areas of Broca's Region, and Their Cytoarchitectonic Characteristics

Areas 44p, 44a, 45p, and 45a are surrounded by multiple areas that differ notably in their cytoarchitectonic characteristics (Tab. 3; Fig.6 and 7). Area 44p bordered the premotor cortex area 6r1 (Ruland et al., 2025) caudally, within the fundus of the precentral sulcus, preCS. Dorsally, it was adjacent to the inferior frontal junction (IFJ) areas ifj1 and ifj2, as well as the IFS areas ifs1, ifs2, and ifs4 (Ruland et al., 2022). Ventrally, it bordered areas Op6 and Op8 of the frontal operculum (Saal, 2019; Unger et al., 2023). Area 44a was located rostrally to area 44p. Dorsally, it bordered the same IFJ and IFS areas: ifj1, ifj2, ifs1, if2, and ifs4. Ventrally, it bordered the area Op8.

Area 45p was situated anteriorly to area 44a. Dorsally, it bordered areas ifj1, ifj2, ifs1, ifs2, and ifs4, as well as the middle frontal gyrus (MFG) area MFG5 (Bruno et al., 2024). Ventrally, it was bordered by opercular areas Op9 and Op10 (Saal, 2019).

Area 45a, positioned rostrally to area 45p, also shared a dorsal border with area MFG5. Rostral to it lay the Inferior frontal gyrus (IFG) areas IFG2 and IFG1 (Zhang, 2025). Ventrally, it bordered the opercular area Op9.

Area	Cytoarchitectonic features
Dorsally located neighbouring areas	
ifj1	blurred transition between layer VI and white matter, densely packed granular cells in layer II, and large pyramidal cells mainly in deep layer III. Area ifj2 contained larger pyramidal cells in upper layer V and large pyramidal cells almost exclusively in the very low part of layer III, as compared to ifj1.
Ifj2	
Ifs1	barely recognizable layer IV was invaded by pyramidal cells of layers III and V Blurred layer II/III border Subdivision of layer III into an upper part with smaller and a lower part with larger pyramidal cells. Layer V has a gradient in pyramidal cell size from large cells in the upper and smaller ones in lower V, with a low cell density.
Ifs2	
Ifs4	
MFG5	high cell density with a gradient in cell size to layer IIIc Visible, thinner layer IV than in IFG2 but broader than in MFG3 Thinner and less cell density layer V and layer VI than in IFG2 Sharp border to white matter
Ventrally located neighbouring areas	
Op6	disgranular, layer II showed a high cell density, and its border to layer III was visible. Layer IV was intermingled by pyramidal cells from layers III and V. Prominent and elongated pyramidal cells were found in layer V. Layers IIIc and IV had a higher cell density than layer V. Layer VI was broad, with numerous small cells.
Op7	high cell density of layer IIIc, layer IV and the upper layer V The lower cell density of layers IIIa and be and the lower layer V of Op7 Large-sized pyramidal cells within the lower layer III and Layer V Blurred transition with the WM, because of the low cell density in the lower portion of layer VI
Op8	has a dense but narrow layer II, with a sharp transition to layer III. Lover layer III has medium-large prominent pyramidal cells. Layer V consists of pyramidal cells in the upper layer and less densely packed lower Layer V. The transition of layer VI to the WM is mostly sharp.
Op9	dense layer II and a sharp transition to layer III. The upper and mid parts of layer III presented with lower cell packing density. With large prominent pyramidal cells in the lower part of layer III.

Caudally located neighbouring areas	
6r1	barely recognizable, thin, and discontinuous layer IV and could be described as on the transition form from a- to disgranular. The loosely packed granular cells of layer IV were often interrupted by pyramidal cells of layers III and V. Sublayer IIIa cell-dense with pyramidal cells of different sizes. Seamless transition of layer II to III. Relatively high cell density of layer VI.
Rostrally located neighbouring areas	
IFG1	thin layer II with an indistinct border to layer III. Prominent layer III with large pyramidal cells in its lower part. Layer IV is definable with a low number of cells. Layer V is loosely packed. Layer VI is prominent with densely packed cells.
IFG2	layer II has a thin and sharp border with layer III. Layer III with high cell density. Layer IV is densely packed and well-defined. Layer V contained small to medium pyramidal cells. VI is densely packed with cells, and has blurred WM transition

Table 3 Summarised cytoarchitectonic features of Broca's region neighbouring areas

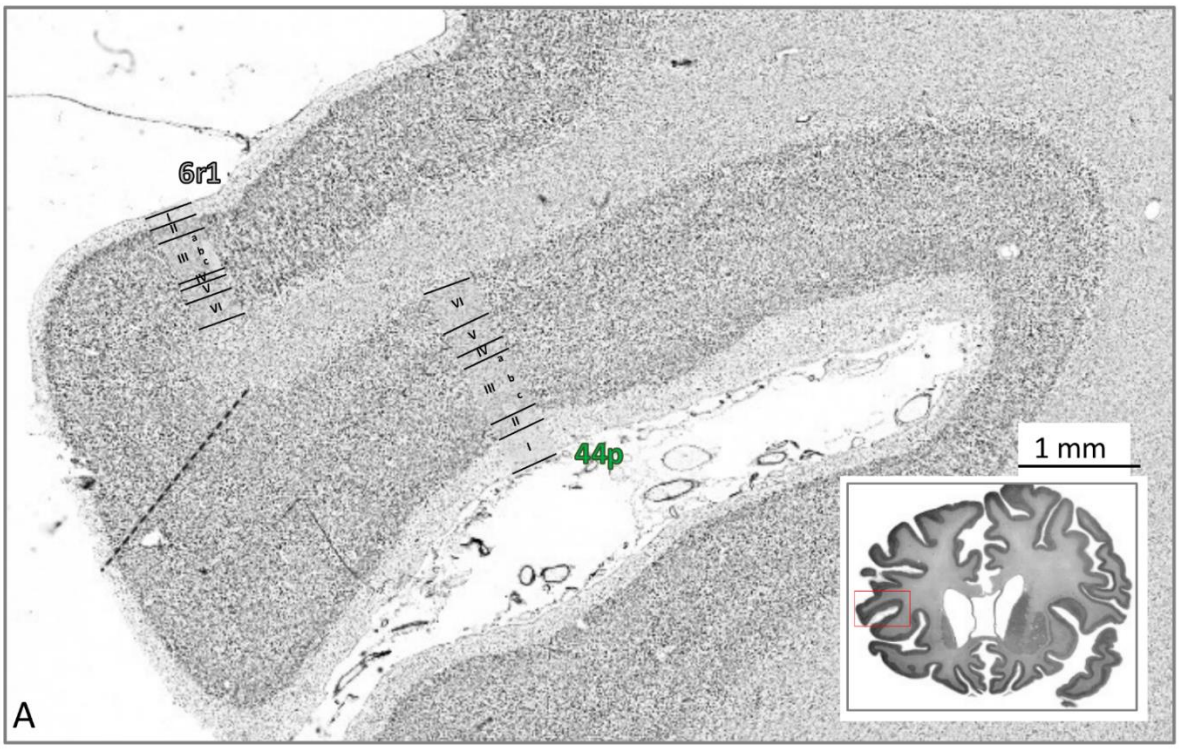

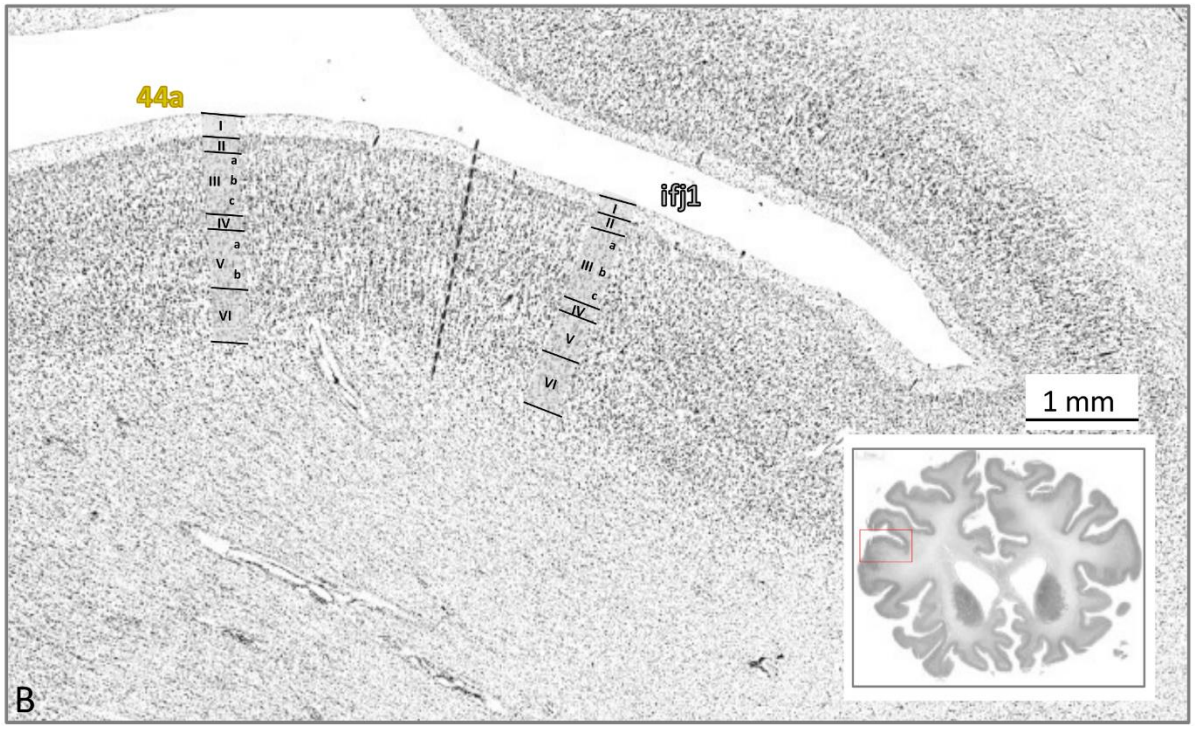

Figure 6 Cytoarchitectonic borders of areas 6r1/44p and 44a/ifj1. (A) Area 6r1 shows a very faint, hardly visible layer IV invaded by pyramidal cells from layers III and V, a narrow layer V, and a sharp transition from Layer VI to white matter. Area 44p has a more visible, though still dysgranular, layer IV and a broader layer V. (B) Area 44a contains more pyramidal cells in layers IIIb-c and fewer cells in layer V, whereas area ifj1 shows larger and more numerous cells in the upper part of layer V and a moderate transition from layer VI to white matter.

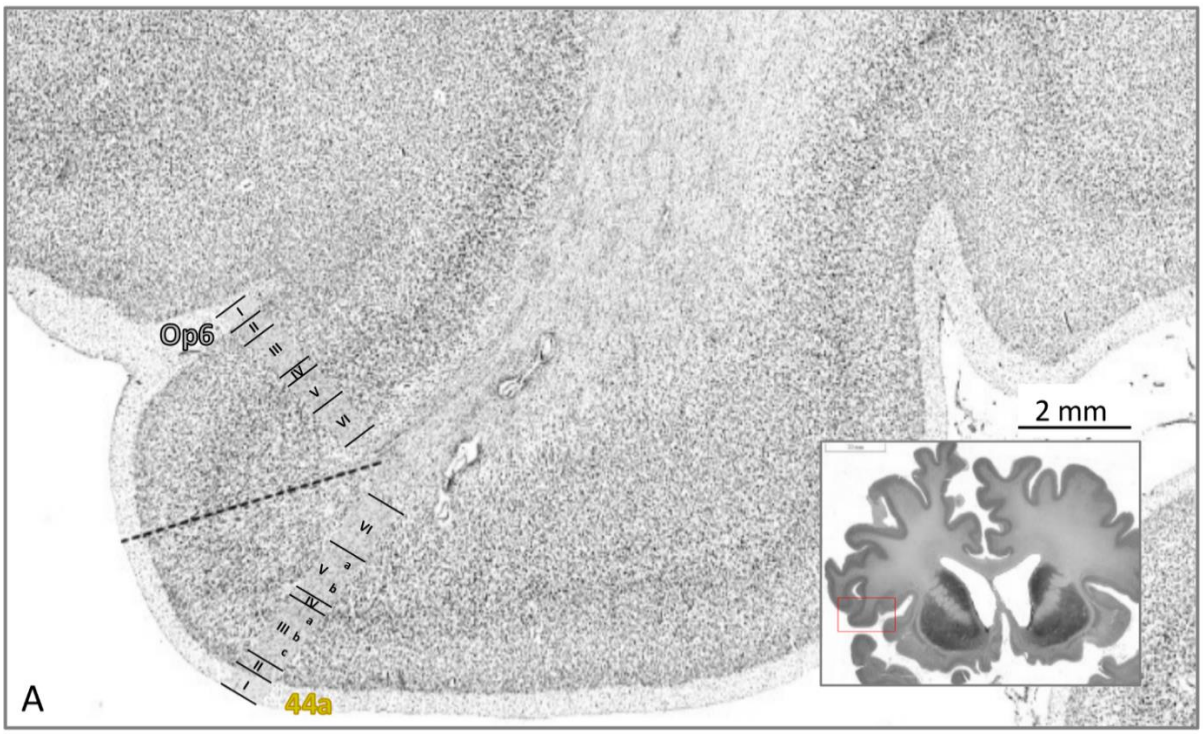

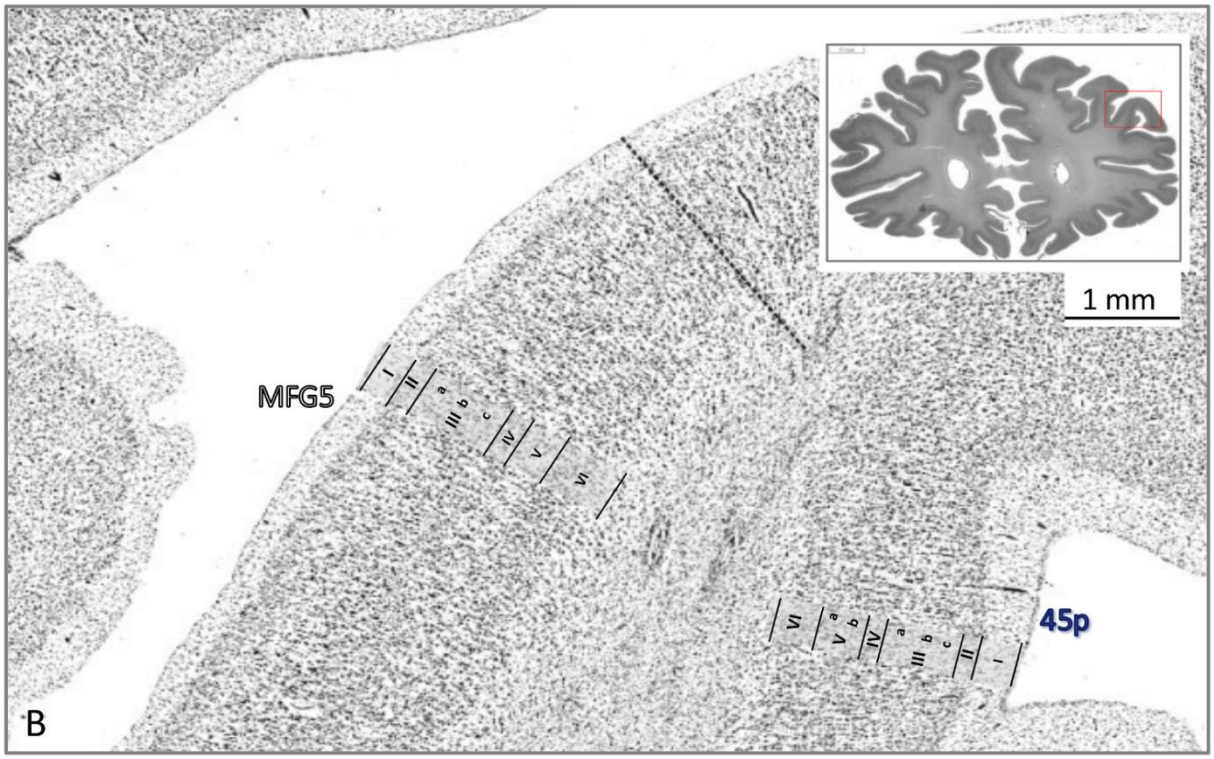

Figure 7 Cytoarchitectonic borders of areas Op6/44a and MFG5/45a. (A) Area Op6 contains fewer cells in layer III, whereas area 44a shows magnopyramidal cells in layers IIIb-c; layer V is more cell-dense in Op6, while 44a has more cells in Vb. (B) Area MFG5 exhibits more cells in IIIb and a narrower layer V, while area 45a shows a broader layer IV and magnopyramidal cells in layers IIIb-c and Va-b.

3.4 Macroanatomical Landmarks and Interindividual Variability of Areas 44p, 44a, 45p, and 45a

Following the 3D reconstruction of the new areas from serial coronal sections, their spatial relationships to macroanatomical landmarks and intersubject variability were assessed in all 20 hemispheres. Each area's location was analysed relative to the sulcal anatomy of the inferior frontal gyrus (IFG), enabling a topographical description of the reconstructed cytoarchitectonic areas 44p, 44a, 45p, and 45a. Relationship of sulcal landmarks and areal borders in the 10 post-mortem brains was summarised in Tab. 4.

In the reconstructed datasets, the cytoarchitectonic areas showed a consistent caudo-rostral arrangement within the IFG, but their surface projections displayed considerable interindividual and interhemispheric variability when viewed in relation to the surrounding sulcal pattern. This variability is illustrated in Fig. 8, showing individual 3D reconstructions of all brains. The pattern of the precentral (prCS) and inferior frontal (IFS) sulci varied between brains. The same was true for the appearance of the diagonal sulcus (DS), Ramus ascendens (RA), and triangular sulcus (TS). The individual maps of 20 hemispheres (Fig. 8) maps provide a visual reference for how areas 44p, 44a, 45p, and 45a are located within Broca's region across different sulcal configurations, while the overall organisation of the areas themselves remains comparable between hemispheres. Broca's region consistently bordered areas 6r1 and 6v3 caudally at the prCS, adjoined ifj and the ifs areas dorsally along the IFS, and extended rostrally toward MFG5, MFG3, and IFG2 at the level of the horizontal ramus of the Sylvian fissure.

Area 44p was consistently found in a posterior position within the Pars opercularis of the IFG. It was typically located at the fundus or rostral bank of the prCS and extended anteriorly into the caudal part of the opercular surface. This pattern was observed in all hemispheres, with the prCS serving as a reliable anatomical reference for its caudal boundary. The anterior extent of the area, however,

showed measurable inter-individual variation. In the left hemisphere, 44p reached the DS in 66.7% of cases (BC 01, BC 05, BC 07, BC 08, BC 20, BC 21) and extended further rostrally into area 44a in 88.9% (BC 01, BC 03, BC04, BC05, BC 08, BC 10, BC 20, BC 21), whereas in only one hemisphere (11.1%, BC 07) area 44p terminated at the DS. IN the right hemisphere area 44p extended into area 44a in 100% of the cases (BC 01, BC 03, BC 04, BC 05, BC 07, BC 08, BC 09, BC 10, BC 20, BC 21) and reached the RA in 50% (BC 01, BC 07, BC 09, BC 20, BC 21). Despite this variability in its anterior reach, the overall localisation of area 44p remained stable.

Area 44a occupied the remaining rostral position of the Pars opercularis, located directly anterior to area 44p. Its localisation showed substantial interindividual and interhemispheric variability, closely tied to the presence and configuration of the DS and Ramus ascendens (RA). In 60% of the left hemispheres (BC 01, BC 05, BC 07, BC 08, BC 20, BC 21), area 44a began within the fundus or rostral bank of the DS. For example, in BC 01 and BC 05, the area clearly emerged from the DS and extended rostrally along its bank, whereas in BC 07 and BC 08, the DS formed a distinct caudal boundary from which area 44a extended anteriorly onto the opercular surface. This pattern was rare on the right side, where it was present in only 10% of cases (BC 08). Conversely, in 40% of right hemispheres (BC 01, BC 02, BC 20, BC 21), the area began in the rostral bank of the RA, a pattern not observed in the left hemisphere. For example, in BC 01 and BC 20, the area extended rostrally along the opercular surface, while in BC 02 and BC 21, the area arose just anterior to the RA and continued dorsally along the opercular surface. In the remaining hemispheres, no distinct sulcus marked the caudal border of area 44a, which lay on the opercular surface without a clearly identifiable anatomical boundary. The left hemisphere more often showed a DS-associated localization, whereas the right hemisphere more frequently showed a shift toward the RA.

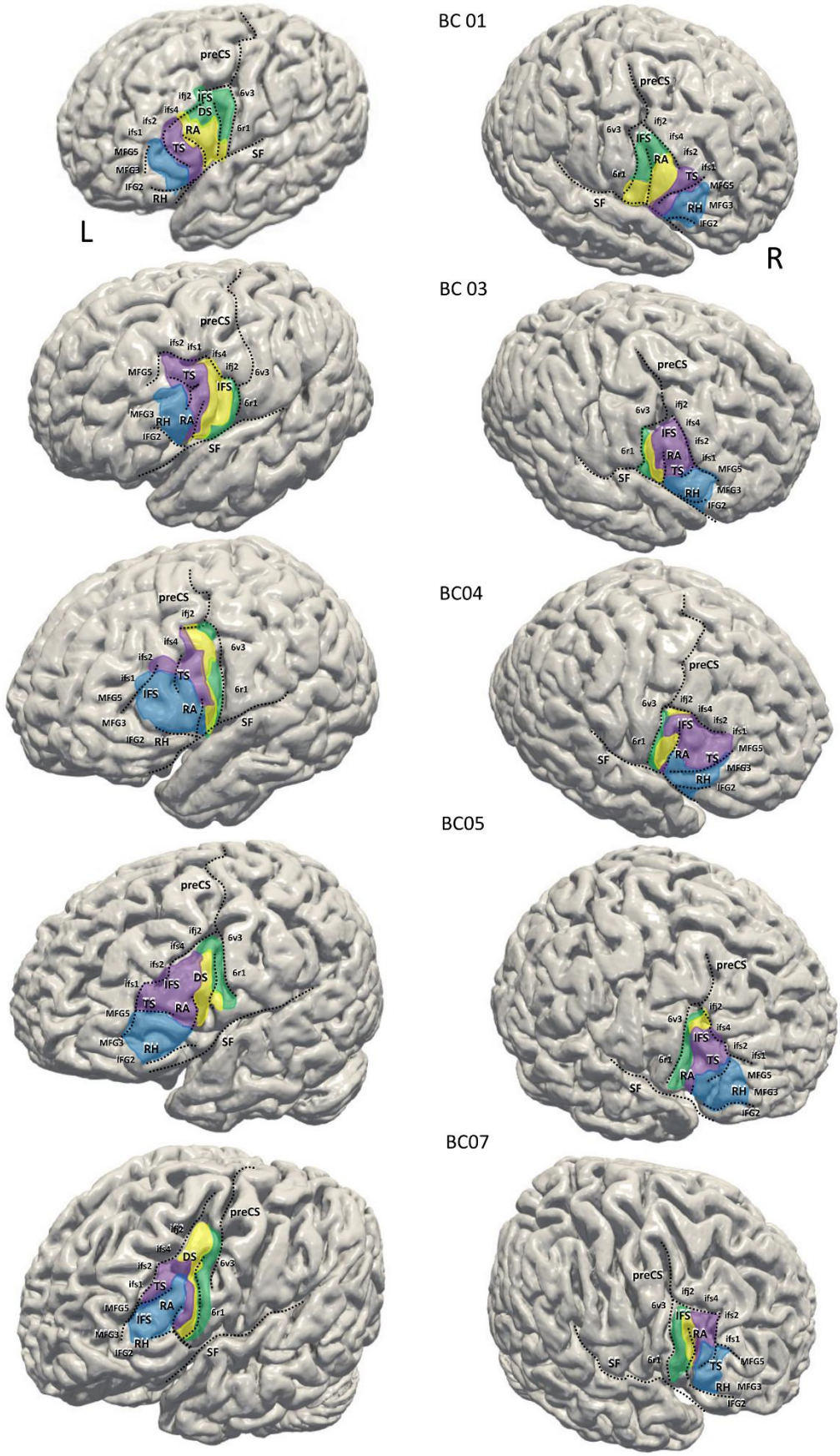
BC 01
BC 03
BC04
BC05
BC07
L
R
preCS
ifj2
IFS
6v3
ifs4
DS
ifs2
ifs1
RA
6r1
TS
SF
MFG5
MFG3
IFG2
RH

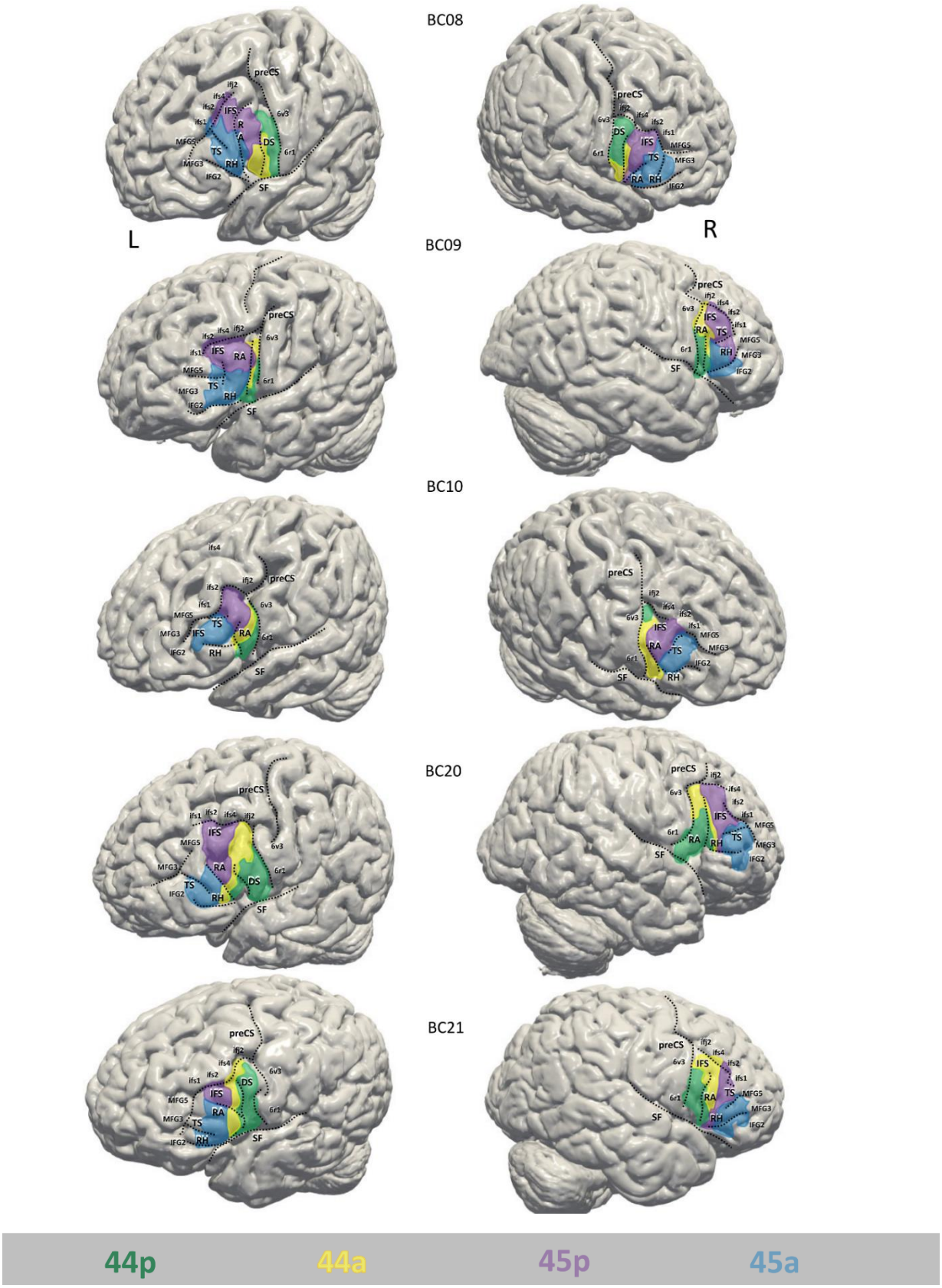

Figure 8: Individual maps of ten post-mortem brains. A 3D reconstruction and maps of Broca's region areas on the pial surfaces of ten brains illustrating the interindividual variability. Black (dotted) lines mark Sulci. BC – brain code, preCS – pre-central sulcus, IFS – inferior frontal sulcus, DS – diagonal sulcus, RA – Ramus ascendens, TS – triangular sulcus, RH – Ramus horizontal, SF – Sylvian fissure. The preCS and IFS are often interrupted and subdivided into several parts. Caudally, Broca's region bordered areas 6r1 and 6v3 at the level of the prCS. Dorsally, it adjoined ifj2, ifs4, ifs2, and ifs1 along the IFS. Dorso-rostrally, it bordered MFG5, and rostrally, it was adjacent to MFG3 and IFG2 at the level of the RH of the Sylvian fissure.

Area 45p was found at the Pars triangularis, rostrally to area 44a. In 50% of left hemispheres (BC 01, BC 03, BC 05, BC 09, BC 10) and 50% of right hemispheres (BC 03, BC 04, BC 05, BC 07, BC 10), its dorsal border was positioned at the fundus or rostral bank of the RA. In the remaining hemispheres, the dorsal border of area 45p was more variable and could not be associated with a consistent anatomical landmark. Nonetheless, area 45p remained well-contained within the Pars triangularis and showed less interindividual variability than areas 44p and 44a.

Area 45a occupied the most anterior part of the Pars triangularis. Its surface localisation varied considerably between brains and hemispheres. In 50% of the left hemispheres (BC 01, BC 04, BC 05, BC 09, BC 10) and 70% of the right hemispheres (BC 01, BC 03, BC 04, BC 10, BC 20, BC 21), area 45a began in the rostral bank of the TS. In 30% of left hemispheres, the area instead began at the rostral bank on the RA, while this was the case in 20% of the right hemispheres. Additionally, in 20% of left hemispheres (BC 03, BC 07) and only 10% of right hemispheres (BC 05), area 45a began at both the TS and the RA, indicating a more extended rostro-caudal placement. Caudally, area 45a reached the fundus or caudal bank of the horizontal ramus (HS) of the Sylvian fissure in all left hemispheres, without spreading onto the orbital part of the IFG. The same pattern was observed in 40% of the right hemispheres, whereas in the remaining 60% (BC01, BC 03, BC 04, BC 09, BC 20, BC 21), the area extended several millimetres beyond the HS, suggesting a more anterior spread in some hemispheres.

Area	Sulcal landmark	Left hemispheres (n=10)	Right hemispheres (n=10)	Total hemispheres (n=20)
44p	Fundus or rostral bank of prCS	10/10 (100%)	10/10 (100%)	20/20 (100%)
44a	Fundus or rostral bank of DS	6/10 (60%)	1/10 (10%)	7/20 (35%)
	Fundus or rostral bank of RA	0/10 (0%)	4/10 (40%)	4/20 (20%)
	No identifiable sulcus at the caudal border	4/10 (40%)	5/10 (50%)	9/20 (45%)
45p	Fundus or rostral bank of RA	5/10 (50%)	5/10 (50%)	10/20 (50%)
	Variable location within Pars triangularis	5/10 (50%)	5/10 (50%)	10/20 (50%)
45a	Rostral bank of TS	5/10 (50%)	7/10 (70%)	12/20 (60%)
	Rostral Bank of RA	3/10 (30%)	2/10 (20%)	5/20 (25%)
	Both TS and RA	2/10 (20%)	1/10 (10%)	3/20 (15%)
	Caudal border at fundus/caudal bank of HS	10/10 (100%)	4/10 (40%)	14/20 (70%)
	Extended beyond HS	0/10 (0%)	6/10 (60%)	6/20 (30%)

Table 4 This table summarises the surface localisation of newly identified cytoarchitectonical area 44p, 44a, 45p, and 45a in relation to macronatomical sulcal landmarks in 10 post-mortem human brains (20 hemispheres). For each area, the number and percentage of hemispheres in which a particular sulcus marked the caudal or rostral border are listed separately for the left and right hemispheres. Sulcal landmarks include the precentral sulcus (prCS), diagonal sulcus (DS), ramus ascendens (RA), triangular sulcus (TS), and horizontal ramus (HS) of the Sylvian fissure. The table illustrates both interindividual and interhemispheric variability in the surface projection of these areas.

The newly identified areas displayed differing levels of variability in their localization. Areas 44p and 44a showed the highest interindividual and interhemispheric variability, especially in how their boundaries corresponded to sulcal landmarks and how much of their extent was located on the gyral surface versus within sulcal depths. The presence of the diagonal sulcus was a particularly important factor: when DS was present, area 44a most often began in its rostral bank of the fundus. In hemispheres lacking a DS, area 44a more frequently began in the RA, particularly in the right hemisphere. Similarly, the configuration of the RA and TS appeared to influence the caudal and rostral boundaries of areas 45p and 45a, though with less consistency.

These results highlight the significance of individual sulcal morphology in determining the topographical localisation of cytoarchitectonic areas. Some boundaries corresponded reliably to identifiable sulci (e.g., prCS for area 44p), while others, particularly those of area 44a, were more variable and sometimes not associated with any clear anatomical feature.

The observed variability is exemplarily illustrated by brain BC 05 (Fig. 9), in which the diagonal sulcus was present only in the left hemisphere. On initial inspection, area 44a appeared smaller on the right hemisphere surface. However, its full extent was located within the sulcal depth behind the precentral gyrus and was not visible on the free surface. This example illustrates how sulcal variation, particularly the presence or absence of DS, affects the visibility and surface extent of cytoarchitectonic areas. A general trend was observed across subjects: when the diagonal sulcus was present, area 44a tended to be larger, especially in its surface projection. While not statistically significant in this sample, the pattern suggests that sulcal configuration may have a measurable influence on the size and shape of cortical areas, and further investigation in larger samples is required.

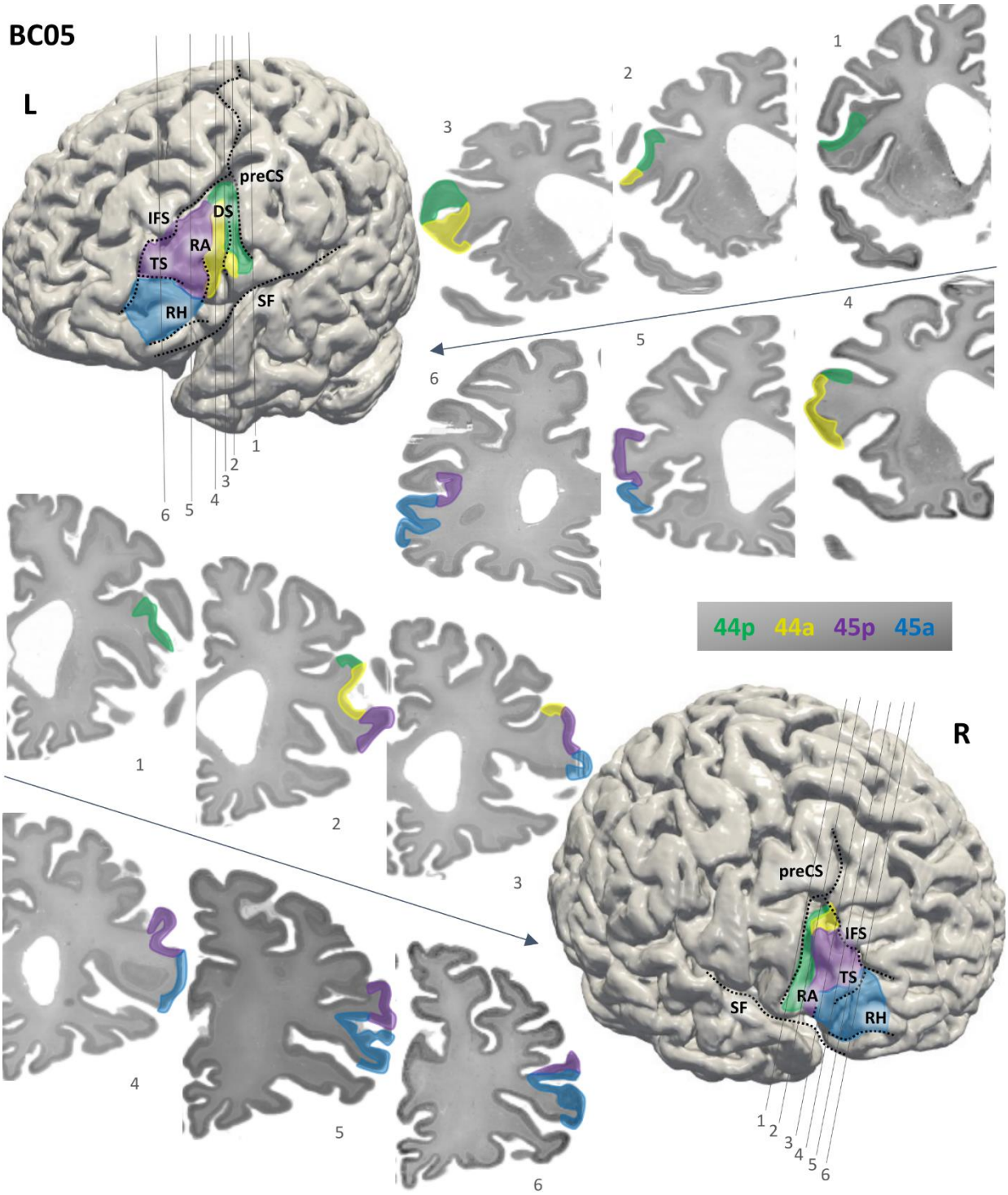

Figure 9: Individual map of the post-mortem brain BC05. A 3D reconstruction and maps of Broca's areas on the pial surface of the separate left and right hemispheres. Black (dotted) lines mark Sulci. BC - brain code; preCS - precentral sulcus; IFS - inferior frontal sulcus; TS - triangular sulcus; DS - diagonal sulcus; SF - sylvian fissure; RA - Ramus ascendens; RH - Ramus horizontal.

3.5 Cytoarchitectonic Relationships Across Broca's Region Areas and Neighbouring Cortex

Areas 44p, 44a, 45p, and 45a could be distinguished based on their GLI profiles in a discriminant analysis (Fig. 10), which enabled their grouping according to specific cytoarchitectonic characteristics. For the statistical analysis, each area was represented by ten points per hemisphere, corresponding to the ten human brains analysed, together with the cross representing the average value of each brain.

The dispersion of points around each centroid reflected the intrasubject variability and thus cytoarchitectonic heterogeneity across individual brains.

While the clusters of areas 44p, 44a, 45p, and 45a show some overlap, the averaged values form four distinct points. Although the GLI profiles varied to some extent between individual brains, the boundaries between all areas could be detected and verified along their entire extent.

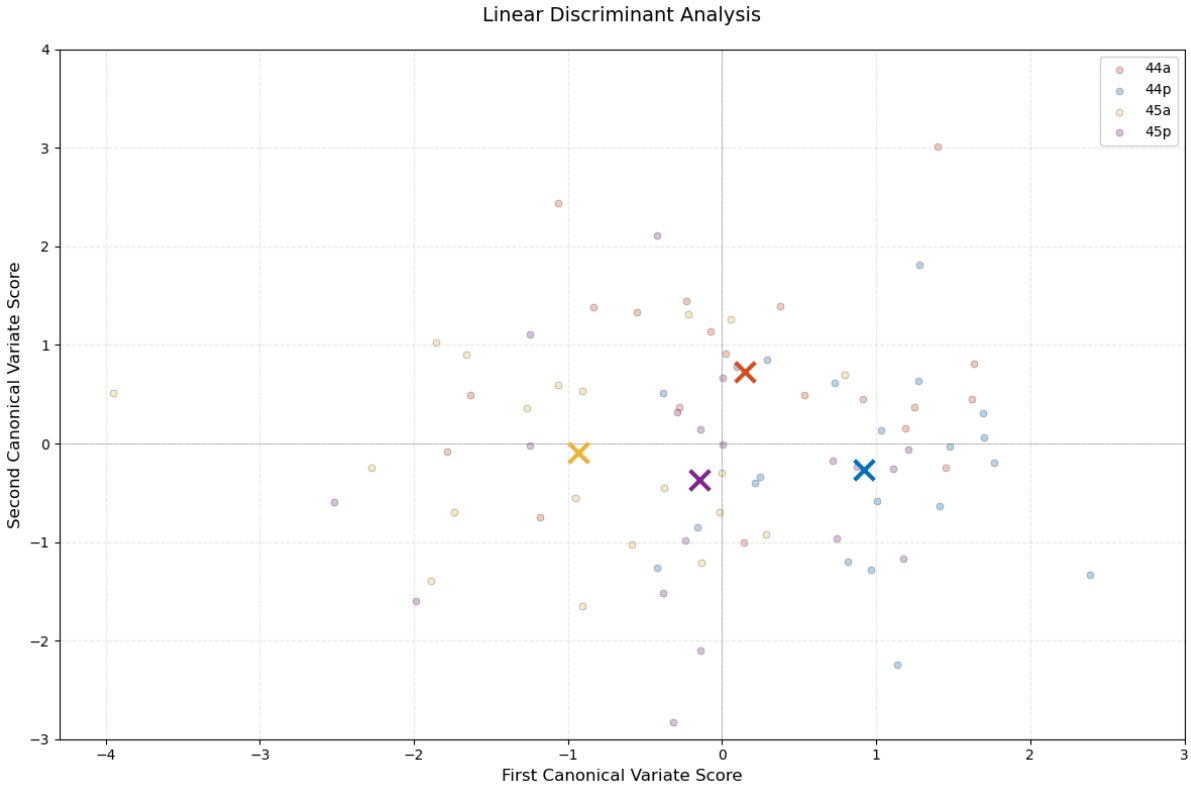

Figure 10 Discriminant analysis of Broca's region areas 44p, 44a, 45p, and 45a. GLI profiles from areas 44p (blue), 44a (red), 45p (violet), and 45a (yellow) were compared using discriminant analysis, with each point representing the profile of an area in a single hemisphere. For each area, the mean position is indicated by a cross. The four areas form clearly separable clusters, and the crosses mark the averaged position of each area without overlap. The spread of points within each cluster reflects intrasubject variability.

To further explore these relationships, multidimensional scaling (MDS) was applied. It allowed to visualize and comparison of the cytoarchitecture of Broca's region areas both among themselves and with neighbouring cortical areas in the left and right hemispheres (Fig. 11). In this analysis, the distances between points represented their degree of cytoarchitectonic similarity, with shorter distances indicating closer similarity in laminar architecture.

In the left hemisphere, three distinct clusters were identified. The first cluster consisted of areas 6r1 and IFG2, which showed strong cytoarchitectonic resemblance. The second cluster included areas 44p, 45p, 45a, 44a, MFG5, and IFG1, reflecting structural similarity within Broca's region areas and adjacent anterior and DLPFC. The third cluster comprised the frontal opercular areas Op6, Op7, OP8, Op9, and Op10, which were more similar to each other than to neighbouring DLPFC areas or to Broca's region.

In the right hemisphere, three clusters were also identified, although their internal structure differed from that in the left hemisphere. The first cluster consisted of areas 44p, 6r1, 45p, and IFG2. The second included areas MFG5, 44a, 45a, and IFG1. The third cluster again comprised the frontal opercular areas Op6, Op7, Op8, Op9, and Op10. Although the overall number of clusters was comparable between hemispheres, the precise relationships among individual areas varied, suggesting

subtle hemispheric differences in the cytoarchitectonic organisation of Broca's region areas and their neighbouring areas.

In the hierarchical cluster analysis (Fig. 12), the relationship between the four areas and neighbouring cortical areas was examined in more detail. The analysis revealed two main clusters. Areas 44p and 45p showed shorter Euclidean distances to each other than to areas 44a and 45a, indicating larger similarity within the posterior subdivisions. Likewise, areas 44a and 45a showed shorter distances to each other than to 44p or 45p, forming a distinct anterior cluster. The posterior cluster (44p and 45p) also showed shorter distances to the neighbouring premotor area 6r1 and the anterior dorsolateral cortex area IFG2 than to IFG1 or MFG5, whereas the anterior cluster (44a and 45a) exhibited shorter distances to IFG1 and MFG5 than to 6r1 or IFG2. The frontal opercular areas formed a clearly separate cluster from both Broca's region clusters, demonstrating their cytoarchitectonic distinction from inferior frontal and dorsolateral cortical areas.

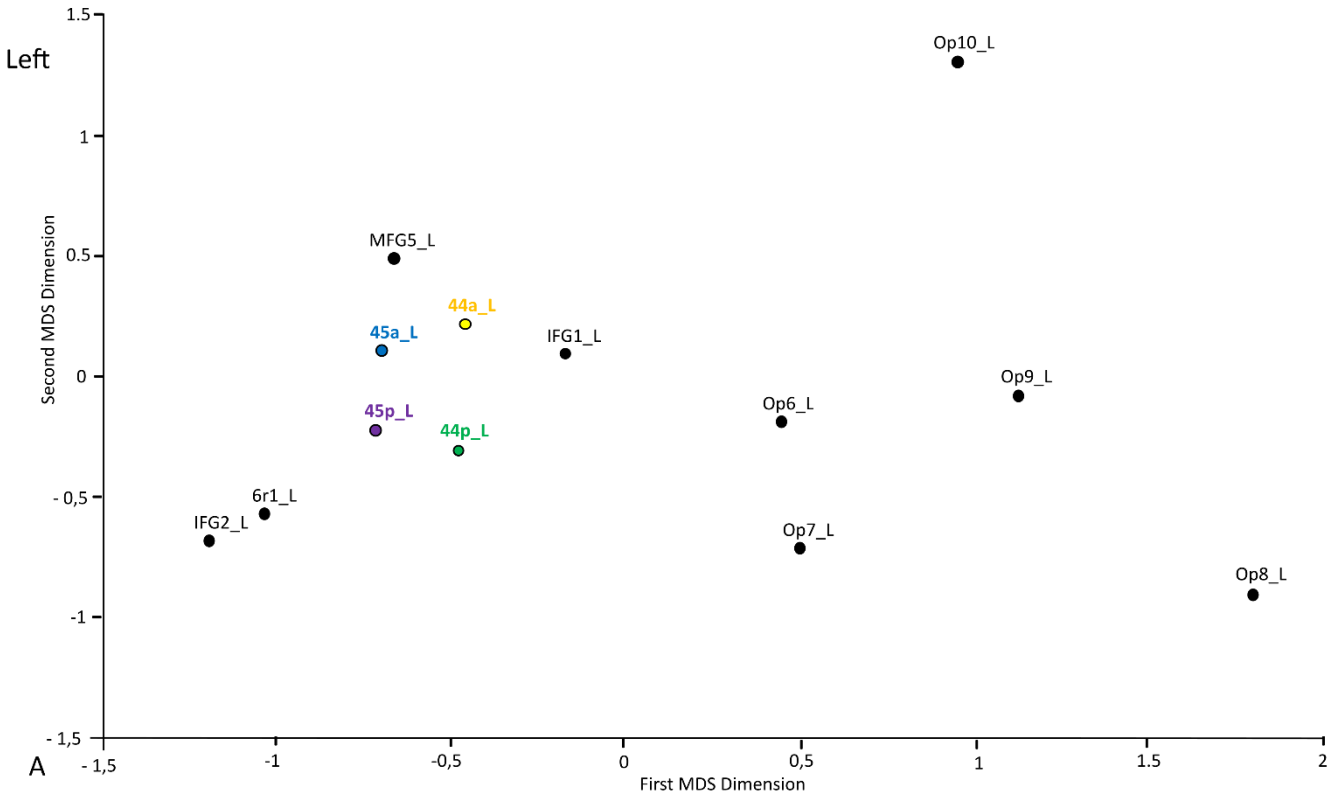

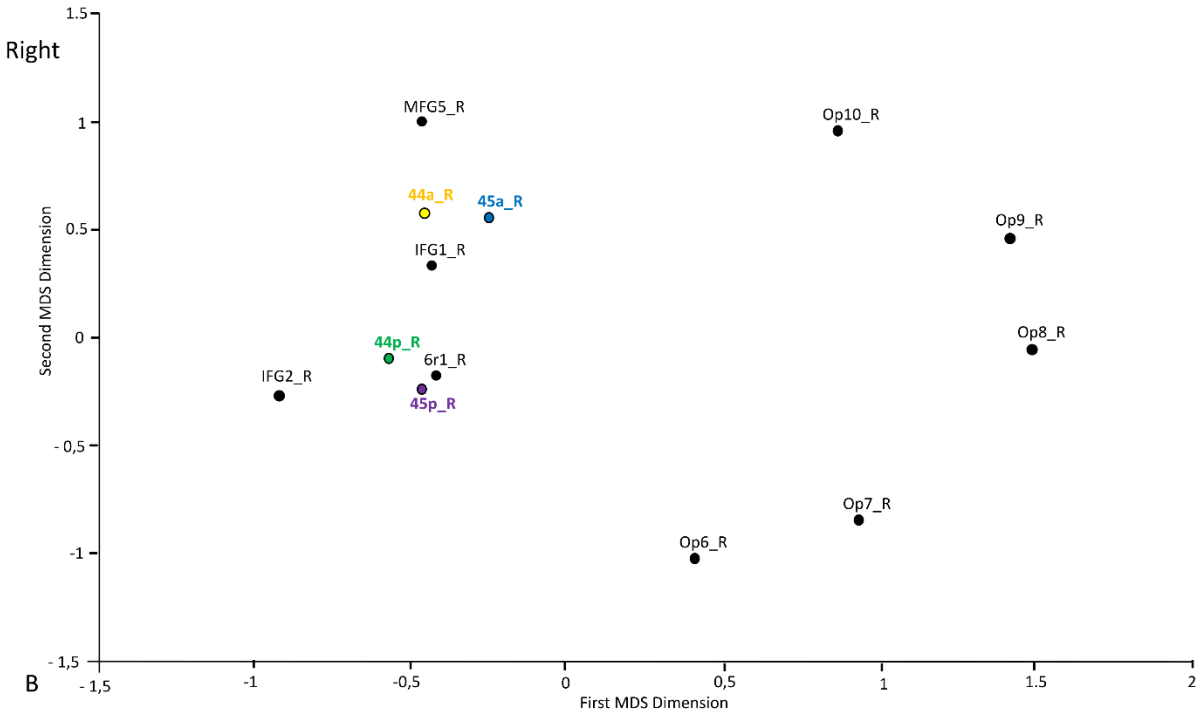

Figure 11 Cytoarchitectonic similarity of areas. Multidimensional scaling of Broca's region areas (44p, 44a, 45p, and 45a) and neighbouring areas (Op6, Op7, Op8, Op9, Op10, IFGa, IFGb, 6r1, MFG5) of the left hemispheres areas (A), and right hemispheres areas (B). Stress value in MDS: 0.047

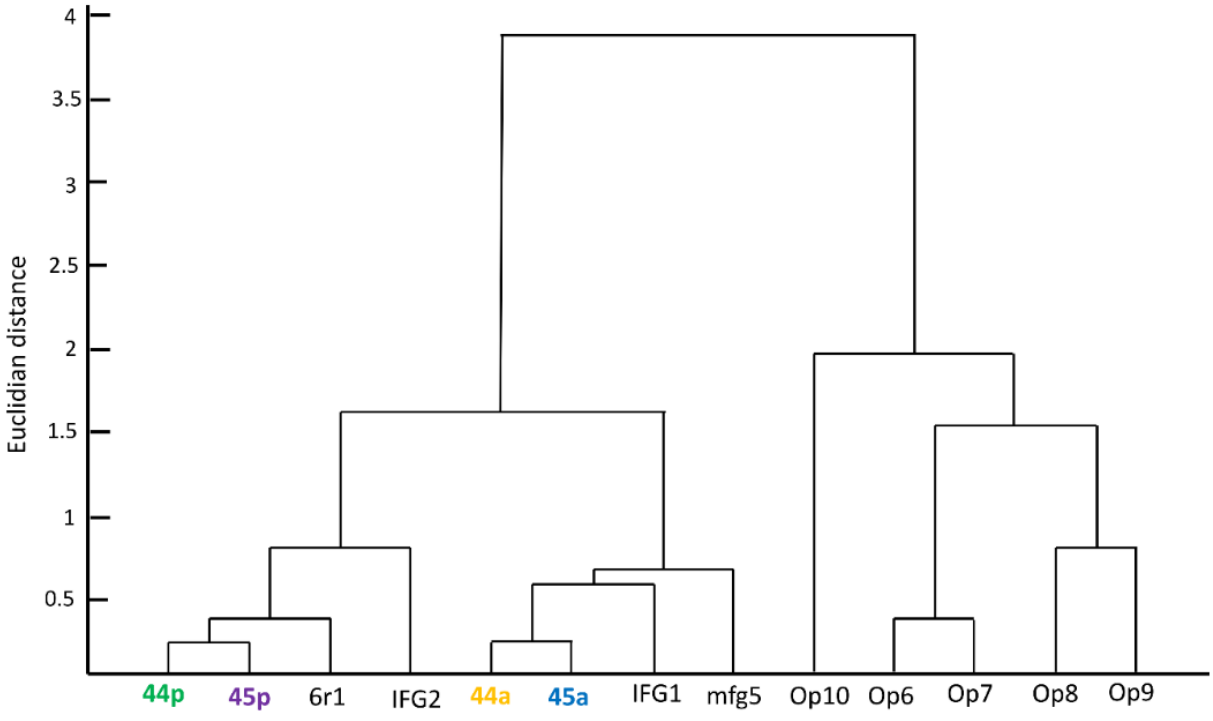

Figure 12 Hierarchical cluster analysis of areas 44p, 44a, 45p, 45a and the neighbouring areas of the anterior lateral pre-frontal cortex (IFG1, IFG2)(Zhang, 2025), dorsolateral pre-frontal cortex (DLPFC) (mfg5) (Bruno et al., 2024), frontal operculum (Op6, Op7) (Unger et al., 2023), (Op8, Op9) (Saal, 2019), pre-frontal cortex (6r1) (Ruland et al., 2025). The Euclidean distance reflects structural similarity. Areas 44p and 45p are cytoarchitectonically closer to areas 6r1 and IFGa, forming a distinct cluster, whereas areas 44a and 45a are closer to areas IFGb and mfg5. Frontal operculum areas form a clearly separate cluster from their neighbouring areas.

Taken together, the discriminant analysis, multidimensional scaling, and hierarchical clustering demonstrated that areas 44p, 44a, 45p, and 45a could be reliably distinguished based on the GLI profiles. The analyses further revealed systematic patterns of similarity between Broca's region areas and adjacent frontal regions, as well as clear structural distinctions from the frontal opercular cortex. The observed hemispheric differences suggest that, despite an overall comparable organisation, the left and right inferior frontal cortices exhibited unique cytoarchitectonic patterns that may underlie aspects of functional lateralisation within Broca's region.

3.6 Left – Right Differences in Cytoarchitecture of Areas 44p, 44a, 45p, and 45a

Euclidean distance is a descriptive measure to visualise interhemispheric differences. They showed that left-right cytoarchitectonic differences varied systematically across Broca's region areas 44p, 44a, 45p, and 45a. Area 44a showed small and consistent hemispheric differences, whereas area 44p showed slightly bigger and markedly more variable differences. Area 45a displayed the strongest asymmetry. Area 45p had the lowest median but the greatest inter-individual variability. Overall, posterior areas (44p, 45p) were characterised by higher variability, and anterior areas (44a, 45a) by more consistent patterns, with the highest lateralisation occurring in area 45a and moderate lateralisation in area 44p; areas 45p and 44a displayed low lateralisation. Overall, these findings suggest that cytoarchitectonic asymmetry within Broca's region is not uniform but follows a systematic organisation. Anterior areas (44a, 45a) show more stable and consistent hemispheric organisation, with area 44a exhibiting low lateralisation and area 45a the highest lateralisation. Posterior areas (44p, 45p) are more variable across individual brains: area 44p showed moderate but variable lateralisation, while area 45p has low median lateralisation with high inter-individual variability.

3.7 Volume of Areas: Sex Differences, and Relationship to the Diagonal Sulcus

3.7.1 Shrinkage-Corrected Volumes of Areas

Shrinkage-corrected volumes of Broca's region subdivisions (44p, 44a, 45p, and 45a) were determined for both hemispheres for males and females (Tab.6). Among males, mean left-hemispheric volumes ranged from 1233 ± 571 mm^3 (area 45a) to 1696 ± 787 mm^3 (area 44a), whereas right-hemispheric means ranged from 995 ± 521 mm^3 (area 44p) to 1791 ± 586 mm^3 (area 45p). Females showed generally smaller absolute regional volumes, with left-hemispheric means ranging from 951 ± 488 mm^3 (44a) to 1236 ± 283 mm^3 (45p) and right-hemispheric means from 868 ± 509 mm^3 (44p) to 1238 ± 224 mm^3 (45a). Intersubject variability (SD) was higher in males, especially in the subdivisions 44a and 45p.

Brain	Sex	Left				Right			
		44p	44a	45p	45a	44p	44a	45p	45a
BC 07	m	1741	1999	2051	1484	1040	842	1380	1262
BC 04	m	943	651	858	1881	453	615	1380	2247
BC 03	m	1615	2448	1753	903	874	1514	2074	1880
BC 20	m	1820	1891	1756	917	1677	1003	1200	1393
BC21	m	1944	1492	527	982	1453	1001	1361	1368
MW		1613	1696	1393	1233	1099	995	1791	1630
SD		606	787	486	571	447	521	586	557
BC 05	f	769	1091	1666	1076	248	260	1200	1375
BC 10	f	635	534	745	369	791	789	890	1268
BC 01	f	1980	1658	1272	1431	1487	1872	1005	816
BC 08	f	704	842	1431	1756	844	940	971	1680
BC 09	f	818	627	1963	1231	970	606	1137	1052
MW		981	951	1236	1173	868	896	1041	1238

SD		475	488	283	316	509	316	400	224

Table 6 Shrinkage-corrected area volumes (mm³) for left and right hemispheres areas 44p, 44a, 45p, and 45a. BC indicates the brain code for each subject. Means (MW) and standard deviation (SD) are provided for each sex.

3.7.2 Normalised Regional Volumes

To account for interindividual variability in total brain volume, normalized values were calculated for each region, hemisphere, and sex (Tab. 7).

In females, normalised left-hemispheric means ranged from 0.0856 ± 0.0488 (44a) to 0.1114 ± 0.0284 (45p), whereas in males, left-hemispheric values ranged from 0.0980 ± 0.0403 (45a) to 0.01326 ± 0.0567 (44a). The right hemisphere showed a similar pattern, with area 45a consistently presenting the highest normalised mean volume across both sexes.

Sex	Area	Hemisphere	Mean	SD
f	44p	L	0.0886	0.0488
f	44p	R	0.0788	0.0392
f	44a	L	0.0856	0.0385
f	44a	R	0.0808	0.0526
f	45p	L	0.1114	0.0284
f	45p	R	0.0947	0.0116
f	45a	L	0.1047	0.0426
f	45a	R	0.1124	0.0276
m	44p	L	0.1251	0.0246
m	44p	R	0.0842	0.0326
m	44a	L	0.1326	0.0567
m	44a	R	0.0787	0.0308
m	45p	L	0.1090	0.0499
m	45p	R	0.1430	0.0424
m	45a	L	0.0980	0.0403
m	45a	R	0.1309	0.0468

Table 7 Normalised volumes (Mean ± SD) per region by hemisphere and sex

The distribution of normalised values (Fig. 14) revealed that males have higher mean normalised values in most regions.

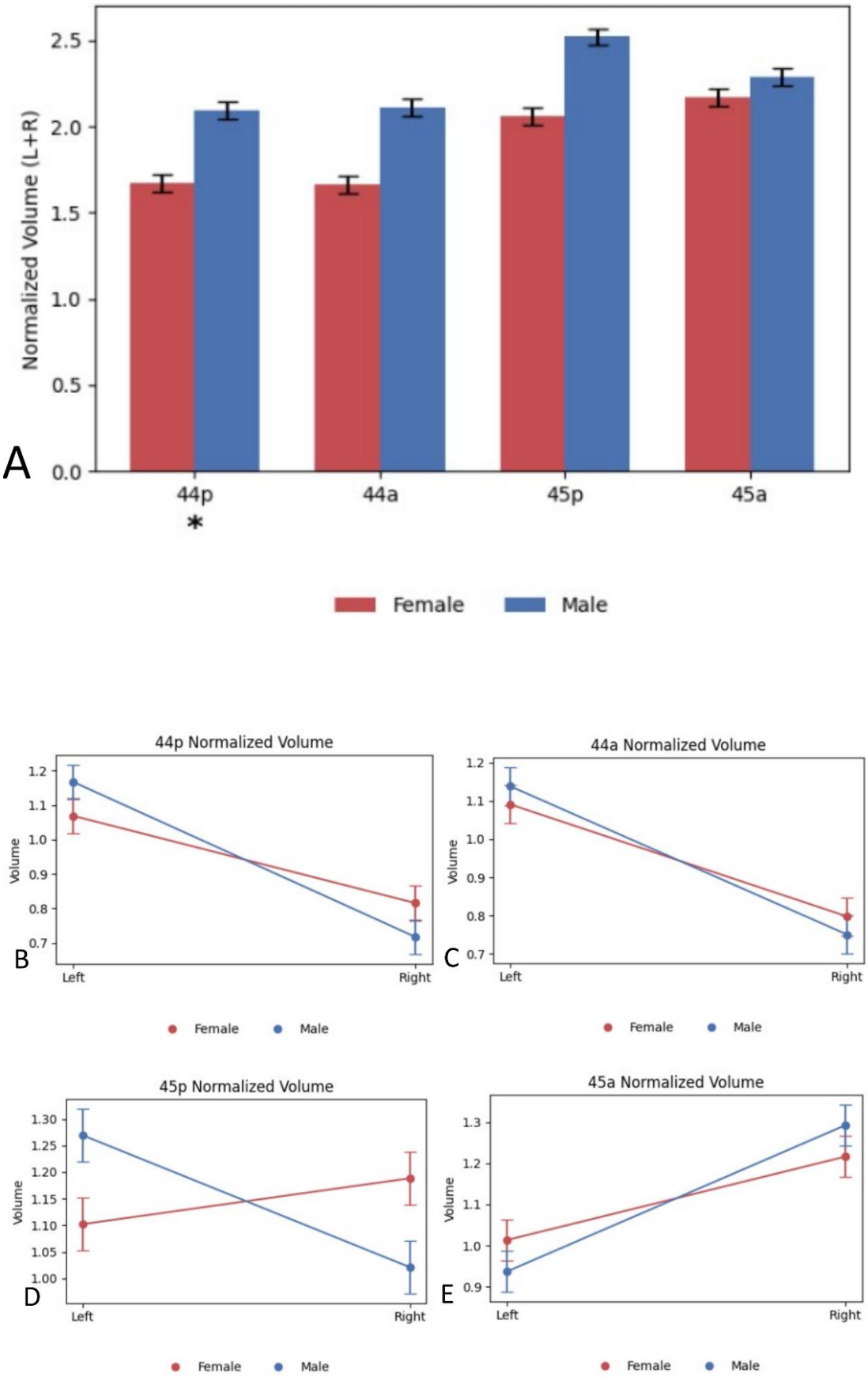

Figure 14 Normalised regional volumes by sex and hemisphere. (A) Bar plot showing normalized volumes (L+R) for females and males across areas 44p, 44a, 45p, and 45a. Error bars represent standard deviations. An asterisk below area 44p indicates a significant hemispheric difference in raw volumes ($p < 0.05$, uncorrected). (B-E) Left vs right hemisphere normalized volumes

for each area, separated by sex. Female volumes are shown in red, male volumes in blue. Error bars indicate standard deviation.

3.7.3 Hemispheric Differences

Permutation-based paired comparisons of left vs right hemispheric volumes revealed regional asymmetries (Tab. 8). Area 44p showed a significant leftward volume asymmetry before correction for multiple comparisons (p = 0.0303). At the same time, 44a exhibited a similar but non-significant trend (p = 0.0721). Anterior regions (45p and 45a) were more symmetric. The area × hemisphere interaction approached significance (p = 0.0534), suggesting that the degree of asymmetry may vary across subdivisions, although this effect did not reach conventional significance thresholds.

Region	L raw	R raw	L-R	p-value	Sig.	95% CI (random)
44p	1.0686	0.8152	0.2534	0.03031	*	[0.0063 – 0.2280]
44a	1.0907	0.7978	0.2929	0.07207		[0.0093 – 0.3212]
45p	1.1021	1.1884	–0.0863	0.62152		[–0.0111 – –0.2893]
45a	1.0136	1.2164	–0.2028	0.19372		[–0.0100 – –0.2872]
Total	4.2749	4.0177	0.2572	0.43315		[0.0194 – 0.6315]

Region × Hemisphere interaction: p = 0.0534; SSQ = 1.8269; 95% CI [0.3208 – 1.8371]

Table 8 Hemispheric differences (permutation test results). The table summarises the results of permutation-based paired comparisons between left and right hemispheric volumes for each cytoarchitectonic area (44p, 44a, 45p, and 45a) of Broca's region. Mean raw normalised volumes are reported for the left (L) and right (R) hemispheres, together with the left-right difference (L-R), associated p-values, and 95% confidence intervals (CI) derived from random permutations. Asterisks (*) indicate results.

3.7.4 Sex Differences

When hemispheric volumes were combined (L+R), no significant sex-related differences were observed (Tab. 9). Although males showed slightly larger total volumes, differences did not reach significance.

Region	L+R F	L+R M	F-M	p-value	95% CI (random)
44p	1.6741	2.0933	–0.4192	0.35449	[–0.0222 – –0.8474]
44a	1.6638	2.1131	–0.4493	0.41889	[–0.0340 – –0.9826]
45p	2.0604	2.5204	–0.4600	0.23465	[–0.0244 – –0.7122]
45a	2.1713	2.2888	–0.1175	0.77672	[–0.0254 – –0.6963]
Total	7.5697	9.0156	–1.4460	0.18682	[–0.0741 – –1.9566]

Region × Sex interaction*: p* = 0.9108; SSQ = 1.0576; 95% CI [0.8901–5.3015]

Table 9 Sex differences (permutation test results). This table presents the results of permutation-based analyses comparing total (left + right) shrinkage-corrected volumes between male and female hemispheres across cytoarchitectonic areas (44p, 44a, 45p, and 45a) of Broca's region. Mean combined volumes (L+R) are provided for females (F) and males (M), alongside their differences (F-M), corresponding p-values, and 95% confidence intervals (CI) based on random permutations. Negative difference values (f-m) indicate larger regional volumes in males, while positive values would indicate larger volumes in females. None of the sex differences reached statistical significance after correction for multiple comparisons. The region × sex interaction was non-significant (p=0.9108), suggesting broadly comparable inter-individual variance patterns between sexes.

3.7.5 Interaction Between Hemisphere and Sex

A region × hemisphere × sex interaction showed no overall significant effect, but there were trends in area 44a toward stronger leftward asymmetry in males (Tab. 10). Permutation testing revealed an L-R

× sex interaction (p=0.0153; SSQ = 3.5575; 95% CI [0.5200-3.1345]), indicating possible sex-dependent variations in lateralisation.

Region	L-R F	L-R M	(F-M) Diff	p-value	95% CI (random)
44p	0.0984	0.4084	–0.3100	0.10373	[–0.0076 – –0.3568]
44a	0.0474	0.5385	–0.4911	0.06935	[–0.0251 – –0.5283]
45p	0.1673	–0.3399	0.5071	0.12513	[0.0366 – 0.5656]
45a	–0.0764	–0.3292	0.2527	0.43686	[0.0525 – 0.5123]
Total	0.2366	0.2778	–0.0412	0.96786	[–0.0454 – –1.2968]

Table 10 Interaction between hemispheric and sex differences (permutation test results). The table summarises permutation-based analyses assessing the interaction between hemisphere (left-right) and sex (female-male) across cytoarchitectonic areas (44p, 44a, 45p, and 45a) of Broca's region. For each region, mean left-right (L-R) volumetric asymmetries are reported separately for females and males, together with the difference between sexes (L-R F; L-R M), associated p-values, and 95% confidence intervals (CI) derived from random permutations. Positive L-R values indicate leftward asymmetry; negative values indicate rightward asymmetry. Although no individual regional effects reached significance after correction, a significant overall region × hemisphere × sex interaction was detected (p = 0.0153, SSQ = 3.5575), suggesting that hemispheric lateralisation patterns differ between males and females, particularly within posterior subdivisions (44p and 44a).

3.7.6 Relationship of Volumes to the Pattern of the Diagonal Sulcus

For area 44p, hemispheres with a DS showed higher median normalised volumes (median = 1.251) than those without a DS (0.781); however, the difference was not statistically significant (p = 0.3834). In area 44a, hemispheres with a DS also showed higher median volumes (median = 1.094) compared to those without (median = 0.605). This difference approached significance (p = 0.0572), suggesting a potential influence of DS morphology on the anterior portion of area 44 (Fig. 15). These results indicate that the presence of a diagonal sulcus may contribute to local volumetric variability, particularly in area 44a, which could reflect morphological heterogeneity within the rostral part of area 44 in Broca's region. Results are summarised in Tab. 11.

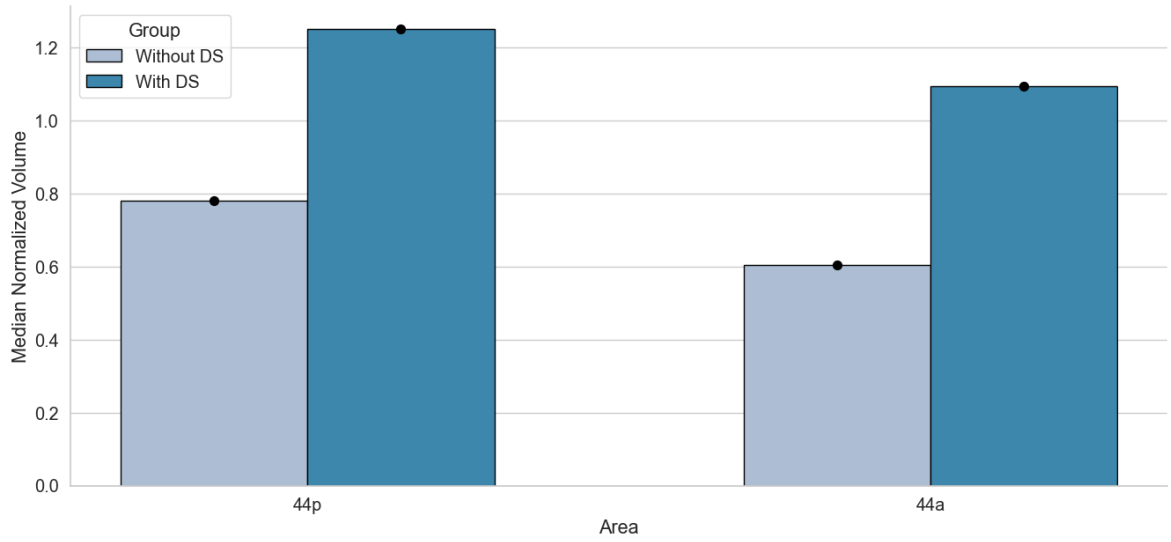

Figure 15 Relationship of the diagonal sulcus (DS) and normalised area volumes. Bar plot shows median normalised volumes for the cytoarchitectonic areas 44p and 44a in hemispheres with and without a diagonal sulcus (DS). Each bar represents the group median, with overlaid black dots indicating individual data points. Median normalised volumes were numerically higher in hemispheres exhibiting a DS for both areas. For area 44a, this difference approach but did not reach statistical significance (Mann-Whitney U test. P = 0.057). No statistically significant difference was observed for area 44p (p = 0.383). These findings indicate a possible association between DS presence and local volumetric variability and should be interpreted as exploratory.

Area	Group	n	Median	p - value
44p	Without DS	13	0.781	0.3834
	With DS	7	1.251	
44a	Without DS	13	0.605	0.0572
	With DS	7	1.094	

Table 11 Mann-Whitney U test comparing normalised volumes between hemispheres with and without a diagonal sulcus (DS). Median normalised volumes and corresponding p-values are reported.

3.8 3D probabilistic Maps in the Julich-Brain Atlas

Three-dimensional cytoarchitectonic probability maps were generated and integrated into the Julich-Brain Atlas to provide a detailed quantitative representation of the four new cytoarchitectonic areas. These maps were aligned to reference spaces, i.e., the Colin27 and ICBM152 non-linear asymmetric 2009c. The centroid coordinates are summarized in Tab. 12. To quantify the degree of intersubject variability, probability maps (pmaps) were computed, reflecting for each voxel the probability that it belongs to a given cytoarchitectonic area (Fig. 16A). Among the investigated regions, areas 44p, and 44a displayed a higher proportion of voxels with lower probability value ("more blue voxels"), indicating a higher interindividual variability in their localization and spatial extent compared to the other areas. All probability maps have been integrated into the Julich-Brain Atlas and are publicly accessible via EBRAINS, thereby promoting reproducibility and facilitating their application in neuroimaging and clinical studies.

Tab. 12 summarises the centres of gravity of each area in MNI (Colin27) space, as well as their corresponding volumetric measurements. Statistical analyses revealed no significant volumetric differences between the left and right hemispheres ($p > 0.05$), and no differences between male and female brains ($p > 0.05$).

Maximum probability maps (MPMs) were computed for all areas to provide a non-overlapping parcellation of the cortical surface, in which each voxel of the reference brain is assigned to the area with the highest local probability (Fig. 16B). These MPMs - Fig. 17 represent the MPMs of the areas 44p, 44a, 45p, and 45a, and in the context of the entire Julich-Brain atlas in the FreeSurfer format available at EBRAINS.eu.

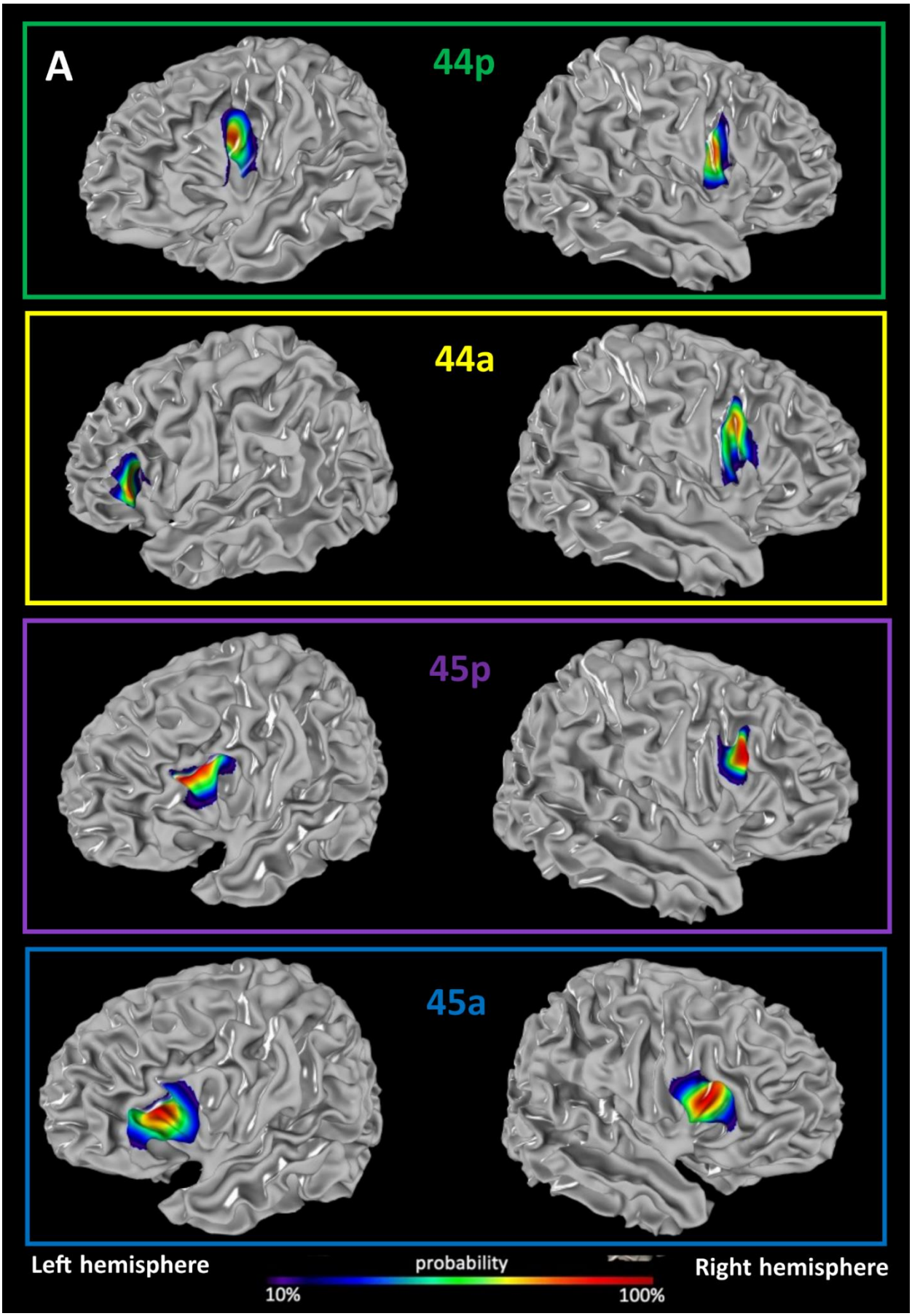
A
44p
44a
45p
45a
Left hemisphere
probability
10%
100%
Right hemisphere

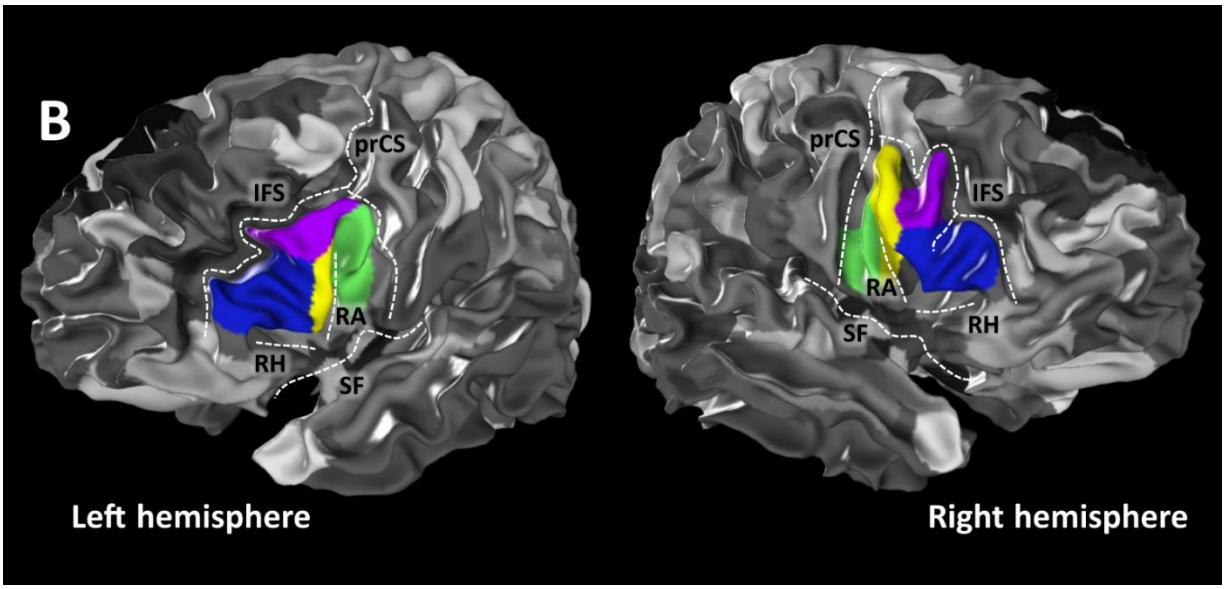

Figure 16 3D Probabilistic maps and maximum probability maps of the areas 44p, 44a, 45p, and 45a. A. Cytoarchitectonic probability maps (pmaps) of Broca's region areas based on the mapping of ten post-mortem brains projected on the smooth white matter surface of the stereotaxic MNI Colin27 template brain (smooth white matter mode). The colour bar indicates the probability with which a certain area was present in a given voxel. B. Maximum probability map (MPM) of Broca's region areas in the MNI Colin27 template (smooth white matter mode). The white dotted lines mark the sulci around Broca's region. prCS pre-central sulcus, IFS inferior frontal sulcus, RA Ramus ascendens, RH Ramus horizontal, SF sylvian fissure. Maps of all areas are freely available in different standard template spaces at EBRAINS.eu.

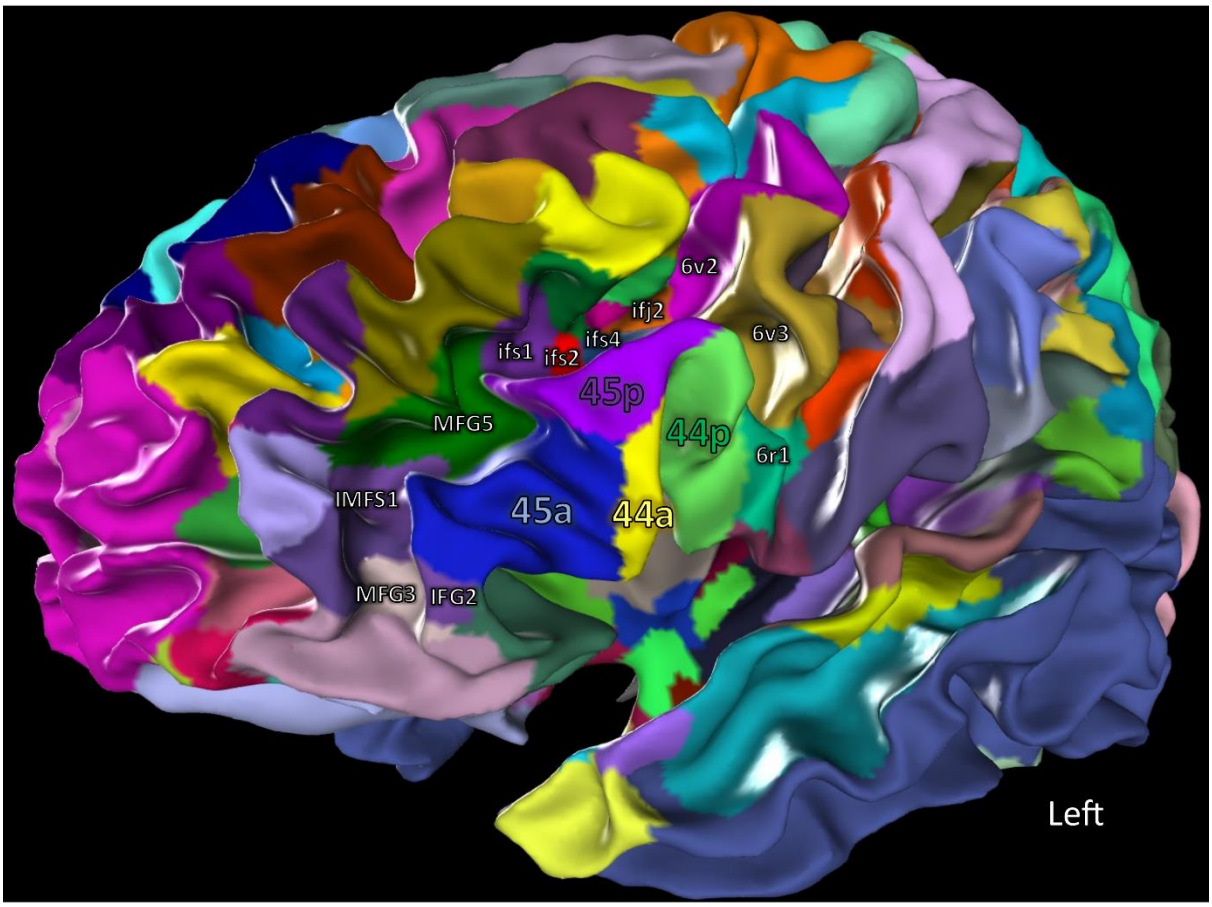

Figure 17: Maximum probability maps of Broca's region with the neighbouring areas. The non-overlapping surface representations (Julich-Brain v3.1) (Amunts et al., 2022) on the smoothed white matter surface of the stereotaxic MNI Colin27 show the stereotactic location of areas 44p (green), 44a (yellow), 45p (purple), and 45a (blue) in relation to neighbouring.

areas of the pre-motor cortex (6r1, 6v3 (Ruland et al., 2025)), inferior frontal sulcus areas (ifs1, ifs2, ifs4, ifj2 (Ruland et al., 2022)), and DLPFC (MFG5 (Bruno et al., 2024)), and anterior LPFC areas (IMFS1, MFG3, IFG2 (Zhang, 2025))

Area	Hemisphere	MNI Colin27			ICBM152casym			Volume (mm^3)
		x	y	z	x	y	z	
44p	Left	-51.21	14.83	17.80	-51.65	14.06	14.59	1296 ± 565
	Right	54.25	13.24	16.06	51.29	15.01	13.98	983 ± 453
44a	Left	-51.20	18.98	17.03	-51.71	18.38	14.05	1323 ± 669
	Right	56.02	16.43	15.76	52.89	18.28	13.40	945 ± 461
45p	Left	-49.31	26.60	23.69	-50.23	26.36	21.08	1314 ± 505
	Right	54.94	25.52	22.07	51.97	27.41	21.26	1415 ± 479
45a	Left	-50.20	31.18	9.38	-51.15	31.34	6.65	1201 ± 450
	Right	53.69	30.79	8.26	50.18	32.43	7.08	1434 ± 410

Table 12 Coordinates (x, y, z) of the centre of gravity of cytoarchitectonic probabilistic maps (pmaps) in MNI Colin27 and MNI ICBM 152 space, as well as shrinkage-corrected area volumes in mm3 (mean ± standard deviation) of areas 44p, 44a, 45p, and 45a in the left and right hemisphere.

3.9 3D Reconstruction of the Areas 44p, 44a, 45p, and 45a in the BigBrain Model

Through the ultra-high-resolution three-dimensional reconstruction of coronal brain sections, the cytoarchitectonic areas 44p, 44a, 45p, and 45a were delineated and visualised in their precise spatial extent on the exposed cortical surface of the BigBrain model (Fig. 18A-D). This reconstruction provides a unique opportunity to examine the fine-grained microstructural organisation of Broca's region in an individual human brain at the cellular resolution. The corresponding datasets have also been made accessible via the EBRAINS research infrastructure, enabling interactive visualisation and quantitative analysis within a common neuroanatomical reference framework.

The BigBrain dataset revealed several distinct hemispheric and sulcal features relevant to the organisation of Broca's region. Notably, the DS was present in the left hemisphere but absent in the right, resulting in divergent spatial arrangements of areas 44p and 44a between hemispheres. In the left hemisphere, area 44p gradually transformed into area 44a, forming a continuous cytoarchitectonic transition along the posterior-inferior to anterior-superior axis. In contrast, in the right hemisphere, the absence of the DS led to a positional shift: area 44p was located more ventrally and posteriorly, whereas area 44a appeared more anteriorly and dorsally.

A comparable hemispheric asymmetry was observed for areas 45p and 45a. When the DS was present, as in the left hemisphere, area 45p originated through a gradual transition from area 44a, making a continuous cytoarchitectonic progression from posterior to anterior regions. In the right hemisphere, area 45p likewise began as a continuation of area 44a, but its localisation differed, being situated in the fundus of RA of the Sylvian fissure (SF). In the left hemisphere, the RA served as a distinct anatomical boundary separating areas 45p and 45a, whereas in the right hemisphere, this border-defining role was assumed by the TS. Additionally, in the right hemisphere, area 45a extended below the RH rostrally, while in the left hemisphere, it was rostrally bordered by the RH.

The availability of an ultra-high-resolution 3D reconstruction, in which each histological section was precisely aligned and mapped using convolutional neural networks (CNNs), was essential for identifying these fine-grained cytoarchitectonic features. This approach ensured a highly accurate correspondence between cellular architecture and macroscopic sulcal morphology. The combination of 3D reconstructions and CNN-assisted mapping enabled precise visualisation of the spatial continuity,

transitions, and boundaries between adjacent cortical areas, thereby providing novel insights into the interhemispheric variability of Broca's region.

Overall, these findings highlight the intricate relationship between local sulcal morphology and cytoarchitectonic differentiation, underscoring the asymmetric structural organisation of the inferior frontal cortex and demonstrating the scientific value of ultra-high-resolution, AI-assisted 3D brain reconstructions in advancing our understanding of human brain complexity.

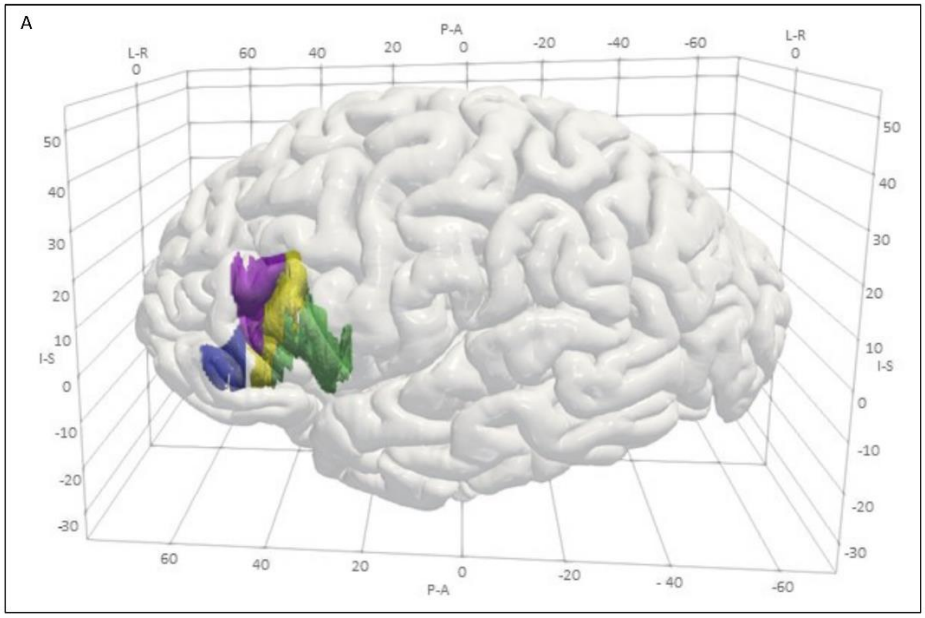

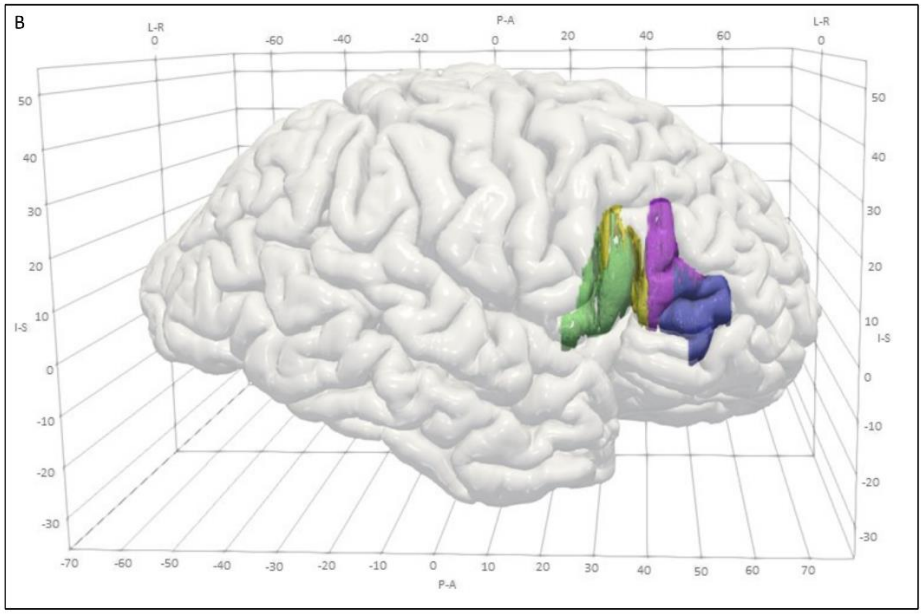

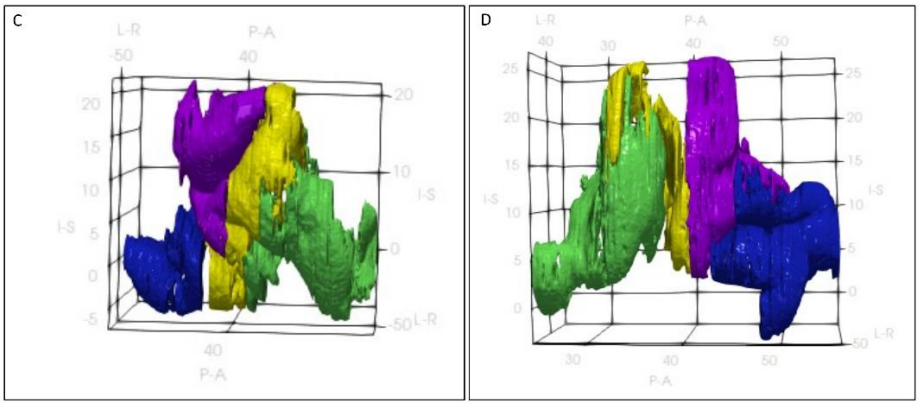

Figure 18: High-resolution 3D maps of areas 44p (green), 44a (yellow), 45p (violet), and 45a (blue), in BigBrain dataset. A+B: Spatial embedding of reconstructed in the BigBrain volume, left and right hemispheres, respectively. C+D: Detailed view of reconstructed cytoarchitectonic areas. Axes x, y, and z correspond to left-to-right, posterior-to-anterior, and ventral-to-dorsal directions. Axis labels are specified in mm and correspond to positions in the 3D reconstructed BigBrain space.

3.10 Spatial Comparison of Cytoarchitectonic Maps with Results from Functional Studies

To provide a first insight into the functional role of the four new areas, we superimposed peak activation coordinates from the three functional neuroimaging (Goucha & Friederici, 2015; Papitto et al., 2024; Zaccarella & Friederici, 2015), focusing on syntax, semantics, and action domains, onto the cytoarchitectonic maps. Given the substantial heterogeneity in theoretical frameworks and experimental designs across language neuroscience laboratories, studies from the Department of Neuropsychology (Max Planck Institute for Human Cognitive and Brain Sciences, Leipzig), led by Prof. Friederici, were included. This decision was based on the lab's consistent theoretical orientation, precise task design targeting core language components, and close methodological alignment with cytoarchitectonic mapping. Their work provides reliable functional data for assessing the structure-function relationship of the newly identified areas with Broca's region. A total of 24 activation coordinates were extracted from these studies and assigned to new cytoarchitectonic areas (Fig. 19A).

In the right hemisphere, five coordinates were identified (Tab. 13): two representing action, one syntax, one semantics, and one syntax and semantics, with no coordinates corresponding to lexical and phonological processing. Spatial variability among the action–related coordinates ranged from 9 mm (x-axis), 3 mm (y-axis), and 12 mm (z-axis). For domains represented by a single coordinate (syntax [33, 29, -2] and semantics [36, 23, -2]), spatial dispersion could not be estimated.

In the left hemisphere, 19 coordinates were found (Tab.13): two representing action, ten syntax, three semantics, two syntax and semantics, and two lexical and phonological processing. Spatial variability across coordinates was as follows:

- Action: x = 20 mm, y = 2 mm, z = 8 mm
- Syntax: x = 21 mm, y = 18 mm, z = 21 mm
- Semantics: x = 9 mm, y = 6 mm, z = 27 mm
- Syntax + Semantics: x = 20 mm, y = 2 mm, z = 8
- Lexical/Phonological: x = 15 mm, y = 12 mm, z = 5 mm

Fig. 19B presents the corresponding functional profiles derived from the co-localization of activation peaks in Figure A. The peak activations indicate a denser and more functionally diverse clustering of coordinates in the left hemisphere compared to the right, reflecting the dominance of the left hemisphere for language-related functions. As illustrated in Fig. 19B, the activation peaks reported in the selected functional studies showed a consistent spatial correspondence with

the cytoarchitectonic architecture of Broca's region. In the left hemisphere, coordinates associated with syntactic and semantic processing were predominantly localised within areas 44a, 44p, and 45a, overlapping with regions known to core combinatorial and integrative language operations. Lexical and phonological coordinates were mainly along the ventral boundary of area 44a and the frontal operculum Id7, Id8, suggesting a functional continuum between classical Broca's region areas and adjacent opercular-insular territories. In contrast, action-related activations extended into premotor areas (6r1, 6v3) and adjacent frontal operculum area Op5, reflecting the engagement of motor-planning and action-related networks that interface with syntactic structuring processes. In the right hemisphere, activation peaks were fewer and exhibited limited spatial dispersion, primarily within areas 6v2, 44p, and Id8, consistent with a supportive rather than dominant role in language processing. Across both hemispheres, most functional peaks fell within or near the boundaries of the newly defined cytoarchitectonic subdivisions of Broca's region, indicating a strong structure-function correspondence between the microstructural parcellation and functional specialisation observed in these independent datasets.

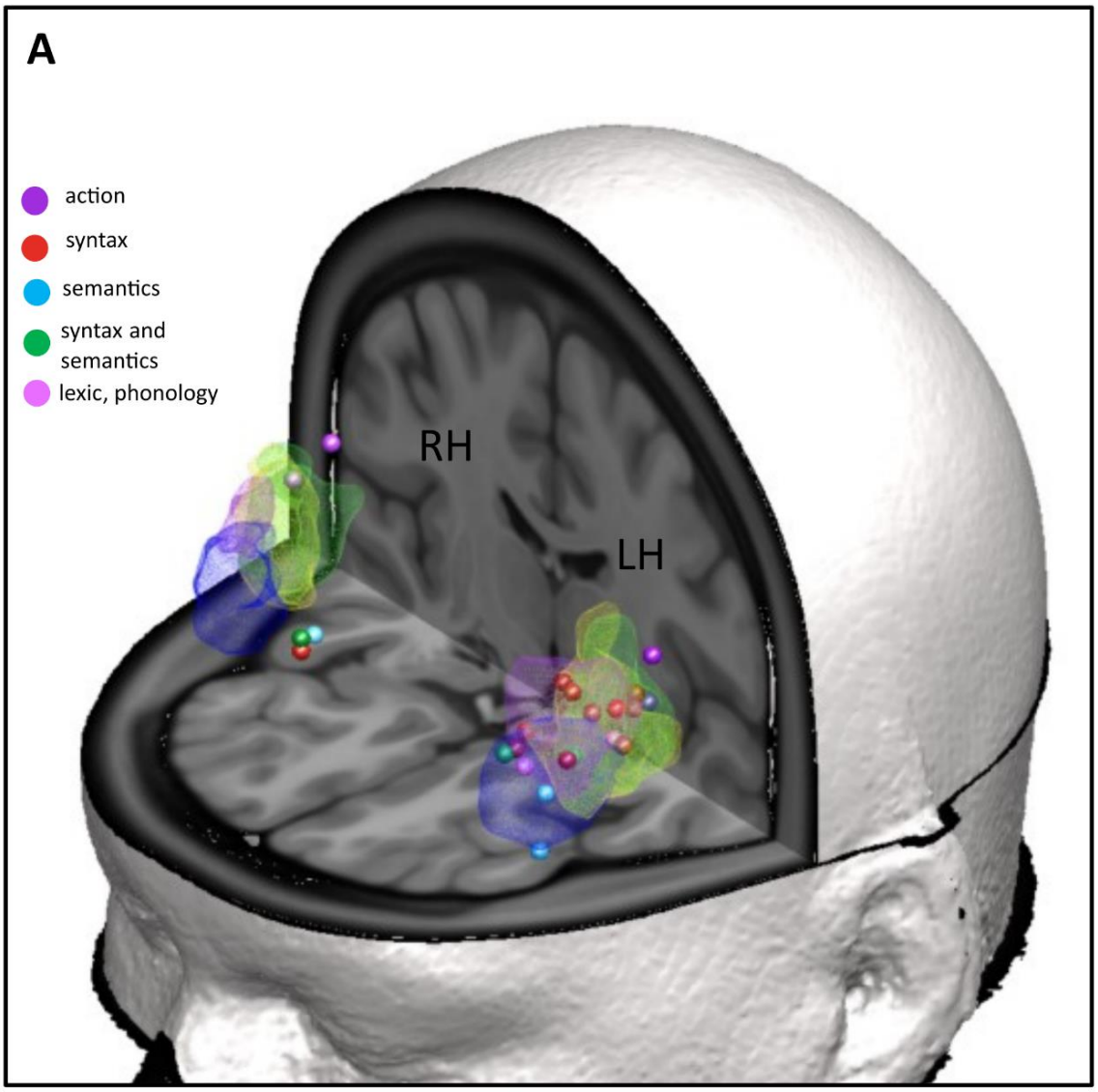

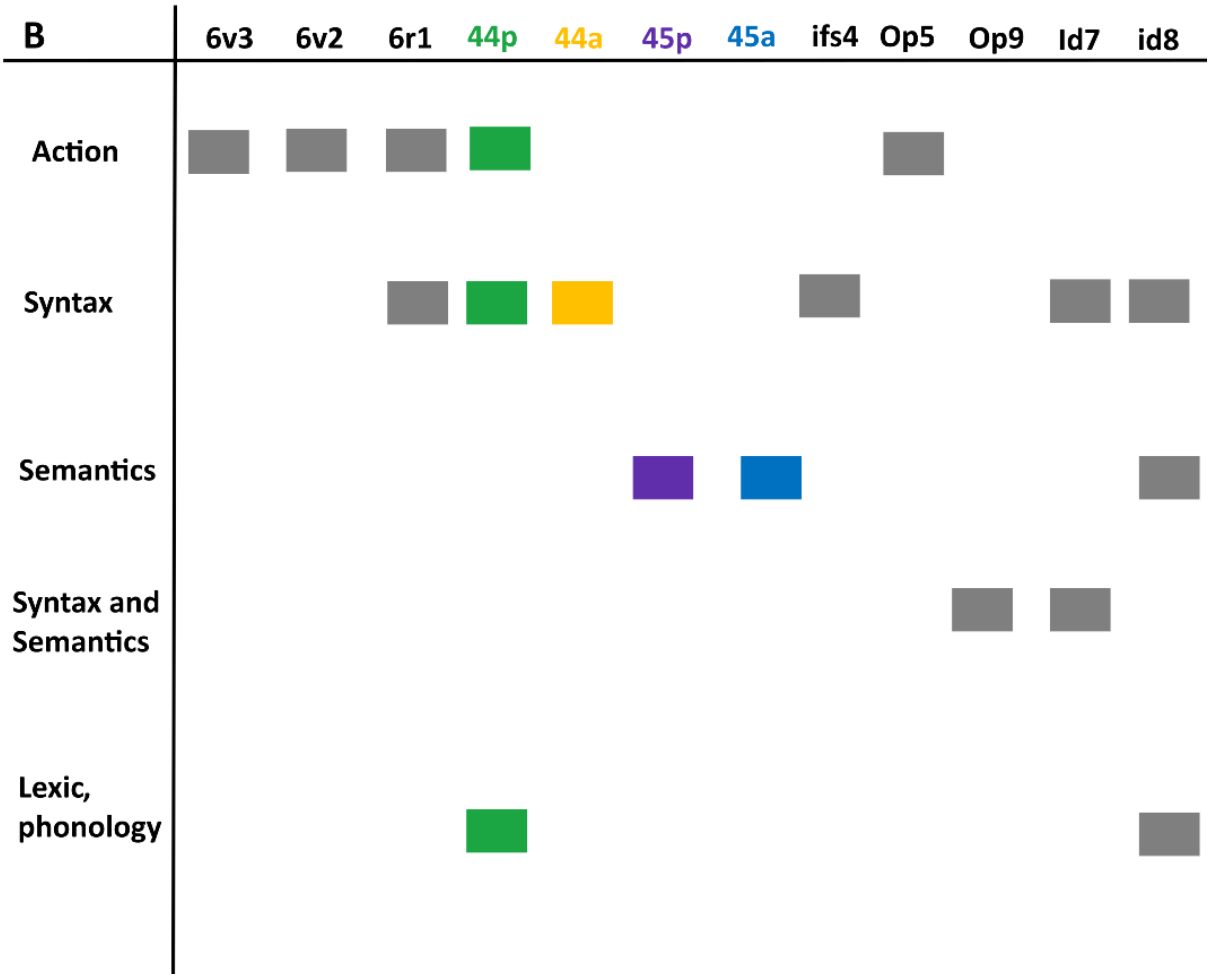

Figure 19 Spatial comparison of Broca's region areas 44p, 44a, 45p, 45a maps and the peak activations coordinates reported in functional studies on language processing and action. **A** 24 coordinates were reported in three studies (Goucha & Friederici, 2015; Papitto et al., 2024; Zaccarella & Friederici, 2015) from the Department of Neuropsychology, MPI CBS in Leipzig, and were plotted on the pmaps of Broca's region areas with a threshold of 40% in ICBM152 space. **B** Functional profiles of Broca's region and neighboring areas as revealed by the co-localisation of study coordinates visualised in **A**. The horizontal axis represents cytoarchitectonic areas and adjacent regions (6v3, 6v2, ifs4, Op5, Op9, Id7, Id8), and the vertical axis represents functional domains (action, syntax, 4semantics, syntax and semantics, lexical/phonological processing). Colored squares indicate co-localisation of study coordinates with each cytoarchitectonic area: green = 44p, yellow = 44a, purple 0 45p, and blue = 45a. Grey squares represent adjacent areas not part of the newly delineated Broca's region subdivisions.

Information from the publication and cytoarchitectonic area assignment	Hemisphere	Location in areas and p-value in the Julich Brain Atlas v3.1	x	y	z	Functional decoding of the experimental setting
Words/whole brain/FOP adINS Zacarella et al. (2015)	Left	Id8, p=0,6	-33	23	2	Lexical-phonological processing
Words/whole brain/FOP/adINS Zacarella et al. (2015)	Right	Id8, p=0,5	36	23	-2	Basic single-word processing with phonological and semantic control support
Words/whole brain/BA 44/ Pars opercularis Zacarella et al. (2015)	left	44p p = 0,26	-48	11	7	Lexical/sublexical phonological language processing

Phrase vs list/volume of interest/BA44/Pars opercularis Zacarella et al. (2015)	left	44p p= 0.57	-48	17	16	Implements core syntactic computation via *Merge*
Contrast phrases lists vs one-word phrase condition/volume of interest/ventral anterior portion of BA44 Zacarella et al. (2015)	left	44p p = 0,46	-51	11	7	Performs syntactic *Merge*; sensitive to structural complexity
AP/RWO/Whole Brain/BA44 Goucha et al. (2015)	left	ifs4 p = 0,3	-42	20	22	Builds hierarchical syntactic structure from word sequences.
AP/RWO/Whole Brain/BA45 Goucha et al. (2015)	left	Op9 p=0.5; BA44=0,4	-50	24	9	Supports lexical-semantic processing and semantic integration during syntax-semantic integration.
AP/RWO/Whole Brain/BA47 Goucha et al. (2015)	left	45a p=0,36	-45	29	-15	Controlled semantic processing and retrieval of lexical meaning
JP/JRO/whole brain/BA44 Goucha et al. (2015)	left	ifs4 p=0,5	-45	20	21	Syntax without meaning
JP/JRO/Whole Brain/BA45 Goucha et al. (2015)	left	45a p=0,58	-54	35	6	Process semantic information conveyed through morphological features.
JP1/JRO1/Whole Brain/Small Volume Correction/B44 Goucha et al. (2015)	left	44a p=0,49	-50	12	16	Core syntactic processing irrespective of semantic content
JP1/JRO1/Whole Brain/Small Volume Correction/BA45 Goucha et al. (2015)	left	45a p=0,64; 45p p=0.36	-54	29	12	Semantic processing beyond lexical access.
JP2/JRO2/Whole Brain/Small Volume Correction/ BA44 Goucha et al. (2015)	left	6r1 p=0,6	-51	8	15	Pure syntax processing
Contrast Function Words/ Content Words/ BA44 Goucha et al. (2015)	left	6r1 p=0,3	-48	5	16	Syntactic and grammatical processing
Contrast Function Words/Content Words/Frontal Operculum/Anterior Insula Goucha et al. (2015)	left	Id7 p=0,5	-30	23	1	Syntax-related processing
Respond to JP/More than to RWO/BA44 Goucha et al. (2015)	left	ifs4 p=0,2	-40	18	21	Syntactic structure independently of lexical semantics (Syntax without meaning)

Category Processing Phrase/BA44 Papitto et al. (2024)	right	6r1 p=0,5; 44p p=0,34	57	11	22	Processes hierarchical rules and encodes structure action sequences
Category processing phrase/BA6 Papitto et al. (2024)	left	6v3 p=0,8	-57	8	31	Motor sequence planning, hierarchical structuring
Category processing phrase/BA6 Papitto et al. (2024)	left	Op5 p=0,5	-45	-1	10	Rule-based motor preparation
Category processing phrase/BA6 Papitto et al. (2024)	right	6v2 p=0,7	48	8	34	Plans structure actions based on rule-governed sequences
Category processing phrase/Pars orbitalis BA47 Papitto et al. (2024)	right	Id8 p=0,6	33	29	-2	Monitoring and adaptive control of syntactic rules processing
Category processing phrase/Insula Papitto et al. (2024)	left	Id7 p=0,4	-30	20	4	Syntactic hierarchy tracking and integration
Execution/BA45 Papitto et al. (2024)	right	Id7 p=0,6	33	29	1	Dynamic prioritization of syntactic and semantic rule processing
Execution/Insula Papitto et al. (2024)	left	Id7 p=0,5	-30	26	1	Executive control of syntactic and semantic rule integration

Table 13 Data on peak activations from the fMRI studies. Includes the task from the functional study, and anatomical localisation taken from the publications. Includes location identified in the area of the Julich Brain Atlas v3.1 and the p-value, and functional decoding of the experimental setting.

3.11 Functional Meta-Analysis

While the preceding chapter focused on a direct comparison between cytoarchitectonic maps of Broca's region and activation peaks from selected functional neuroimaging studies, the present chapter extends this analysis through a quantitative functional meta-analysis using the BrainMap database. This large-scale, data-driven approach aims to characterise the functional profiles of the newly defined cytoarchitectonic areas 44p, 44a, 45p, and 45a, complemented by area 6r1 as a transitional reference region between premotor cortex and Broca's region areas. Although 6r1 was not part of the present cytoarchitectonic mapping project, it was included to provide a structural and functional bridge between the agranular premotor cortex and the disgranular Broca's region areas. Functional characterisation was derived from BrainMap Sleuth, based on the number of studies reporting activations in specific behavioural domains and subdomains. Twelve figures (Supplementary material Fig. 1-12) summarise the distribution of study counts across the action and cognition domains and their respective subcategories. Overall, all regions were bilaterally engaged, with cognitive domains represented by a markedly higher number of studies than action-related domains. Across areas, right-hemispheric counts were consistently slightly higher, though differences were small and variable across subdomains.

3.11.1 Function Characterisation Based on BrainMap Sleuth

Across all cytoarchitectonic seed regions, cognitive domains were associated with substantially more studies than action domains, with the highest counts observed in areas 45p (cognition: 512; action 130), 45a (cognition: 480; action 125), and 44p (cognition 465; action 110). Action-related associations were consistently led by execution, followed by imagination and inhibition, whereas cognitive associations were dominated by language, speech, and semantics, with additional contributions from attention and phonology. Among all regions, area 44a left showed the lowest number of associated

studies in both domains (action 45; cognition 308), while its right-hemispheric homologue, as well as area 6r1 and other Broca's region areas, showed higher involvement. Overall, right-hemisphere regions demonstrated higher co-activation frequencies than their left-hemisphere counterparts, despite the traditional left-lateralisation of the inferior frontal language network (Fig. 20).

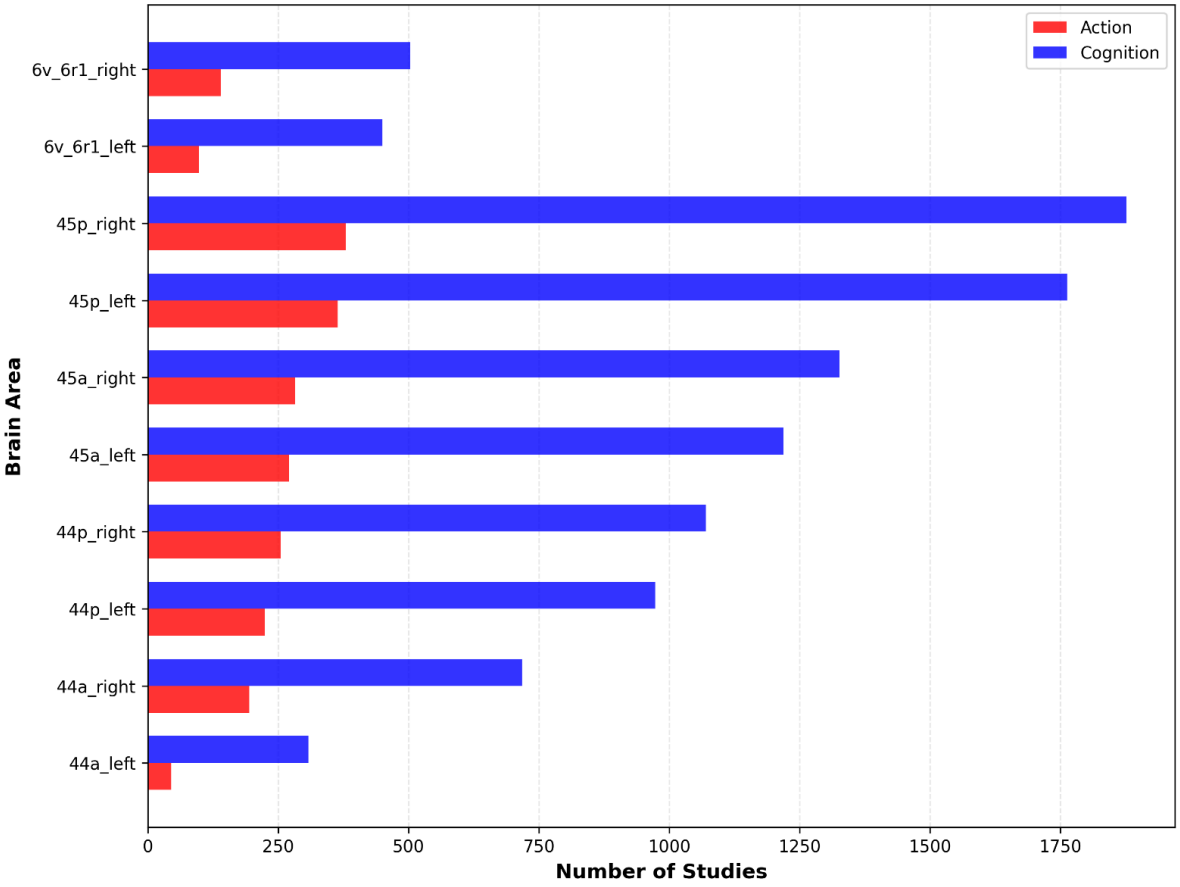

Figure 20: Distribution of Cognitive and Action-Related Domains Across Seed Cytoarchitectonic Regions. The figure illustrates the number of studies associated with Action (red) and Cognition (blue) domains from the BrainMap database for each seed cytoarchitectonic region. Cognitive domains were more frequently represented, particularly in Broca's areas 44p, 45p, and 45a, with 45p showing the highest counts. Area 44a left showed the lowest number of studies for both cognition (308) and action (45), while 44a right and premotor area 6r1 (left: 450/98; right: 503/140 for cognition/action) showed greater involvement, especially for cognition. Overall, right-hemisphere regions exhibited higher co-activation than their left-hemisphere homologues.

When behavioural-domain data were examined in relation to the structural measures described in Section 3.6, functionally rightward-shewed activation patterns were observed predominantly in regions with greater structural dissimilarity – most notably 44a and, to a lesser degree, 6r1 (Fig. 21;22). Posterior IFG regions showed the most balanced functional profiles across hemispheres, with 45p displaying the highest – and nearly symmetrical – counts of studies in both action (left 364, right 380) and cognition (left 1763, right 1876) (Fig. 23; 24). The anterior subdivision is 45a, which also showed largely symmetrical distributions. These findings indicated that only specific subdivisions deviated from classical leftward language dominance, and this deviation occurred primarily in regions demonstrating higher structural asymmetry (Fig.25).

All behavioural subdomain data, including language-related categories (semantics, syntax, phonology, speech) and fine-grained action categories, are provided in full in the Supplementary Material.

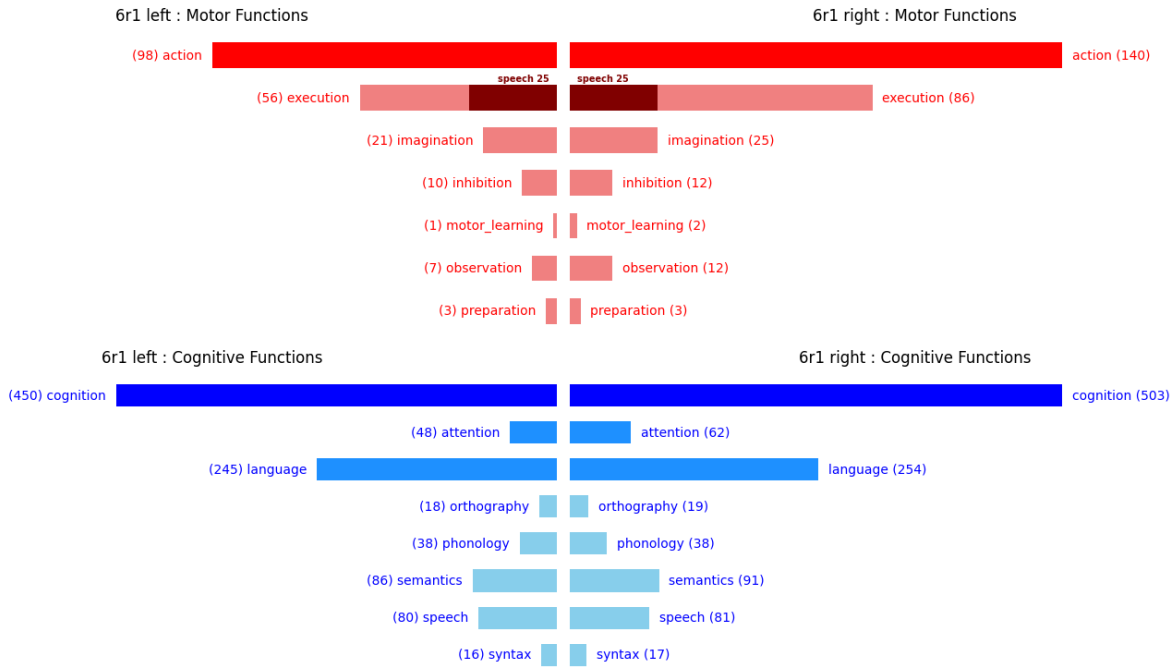

Figure 21 Functional associations of area 6r1 in left and right hemispheres. Area 6r1, a transitional region between PM cortex and Broca's region, exhibits bilateral engagement in both motor and cognitive domains. Vertical bars indicate the number of experiments retrieved from BrainMap via Sleuth, with red representing action-related and blue cognition-related categories. Action subdomains include execution, imagination, inhibition, motor learning, observation, and preparation; cognition domains include attention, language, orthography, phonology, semantics, speech, and syntax. Right–hemisphere associations are slightly more prominent in motor execution and action observation, while cognitive associations, particularly language and speech-related functions, are balanced across hemispheres.

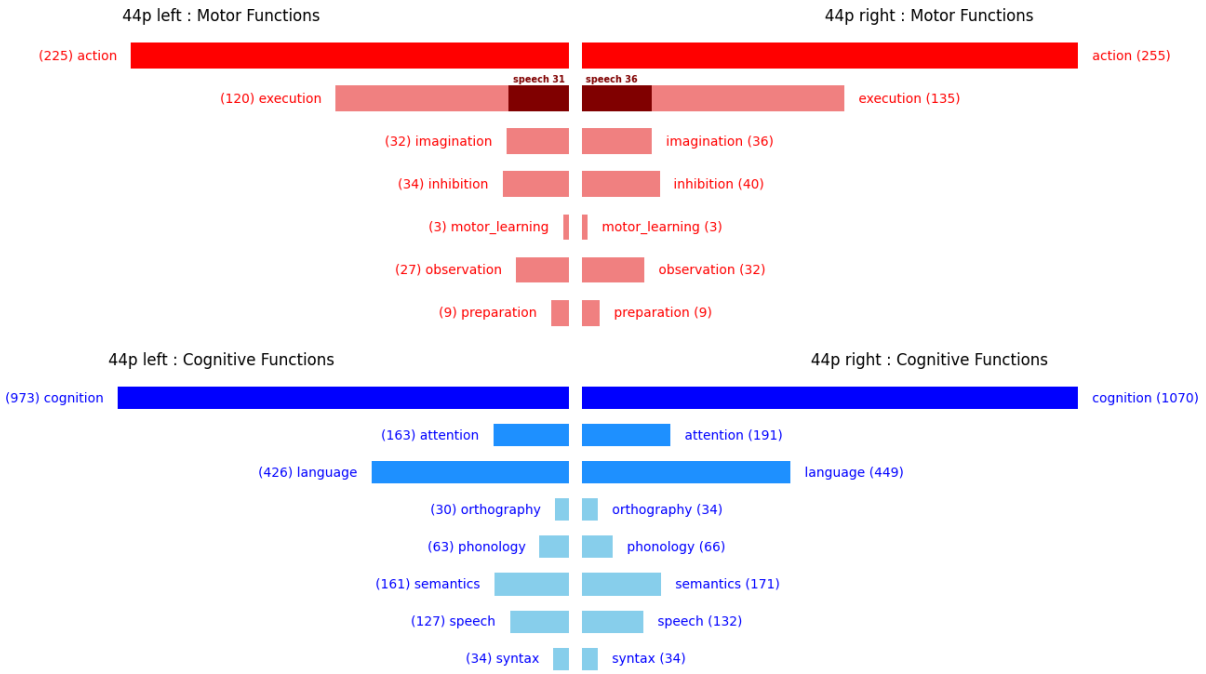

Figure 22 Functional associations of cytoarchitectonic area 44p of the left and right hemispheres. Area 44p demonstrates broad functional involvement across both hemispheres, with action execution and inhibition prominent in the action domain and language, attention, and semantic processes dominating cognition. Vertical bars represent the number of BrainMap experiments (red: action; blue: cognition). Right-hemisphere counts are slightly higher overall, indicating subtle lateralisation, though bilateral representations are maintained for language-related functions, reflecting 44p's role in integrating speech motor control with higher-order cognitive processes.

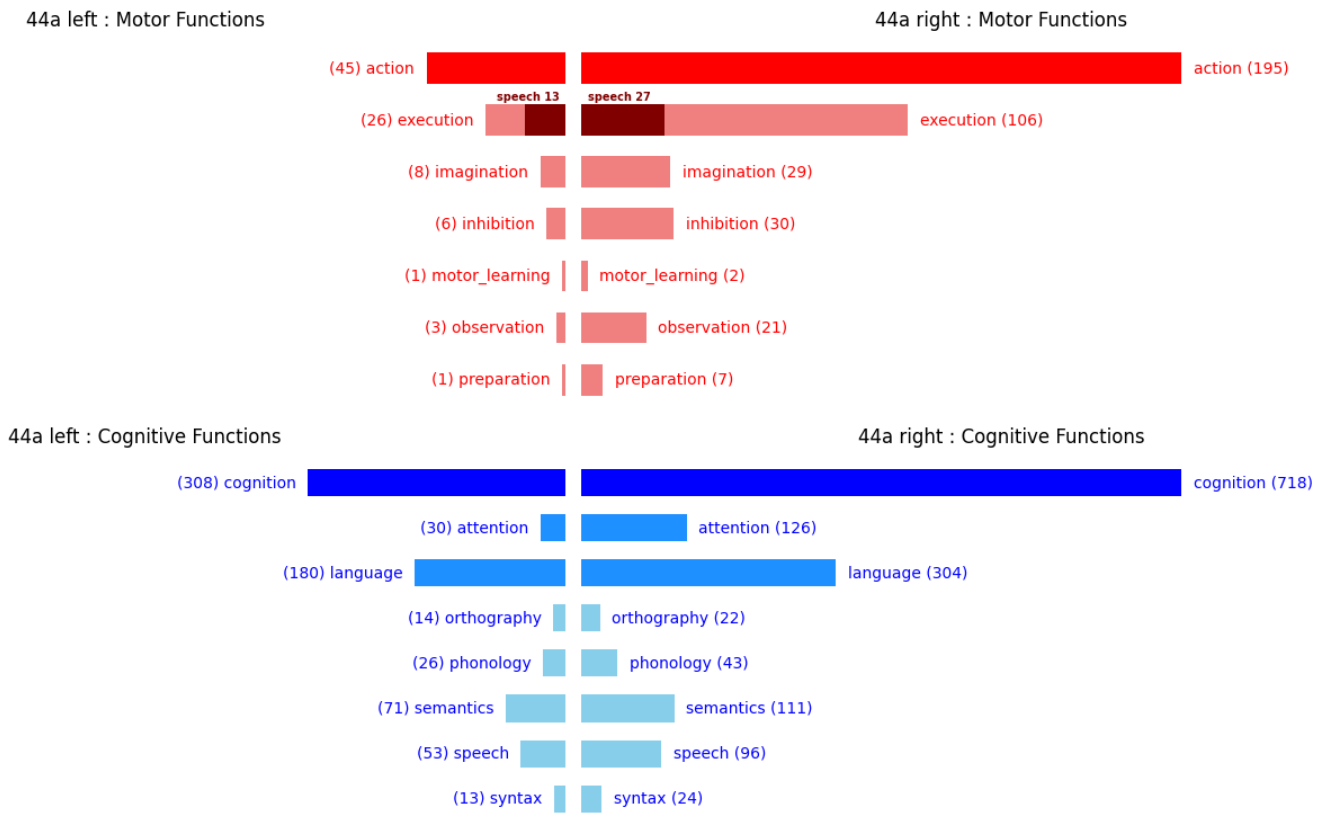

Figure 23 Functional associations of cytoarchitectonic area 44a in the left and right hemispheres. Area 44a shows pronounced right-hemispheric predominance in both action and cognitive domains. Action, execution, imagination, and inhibition are especially represented in the right hemisphere, while cognition is dominated by language, attention, and semantic tasks. Bars indicate experiment counts from BrainMap (red: action; blue: cognition). The lateralization pattern suggests that 44a contributes more selectively to right-lateralized aspects of motor control and cognitive integration compared to neighbouring 44p.

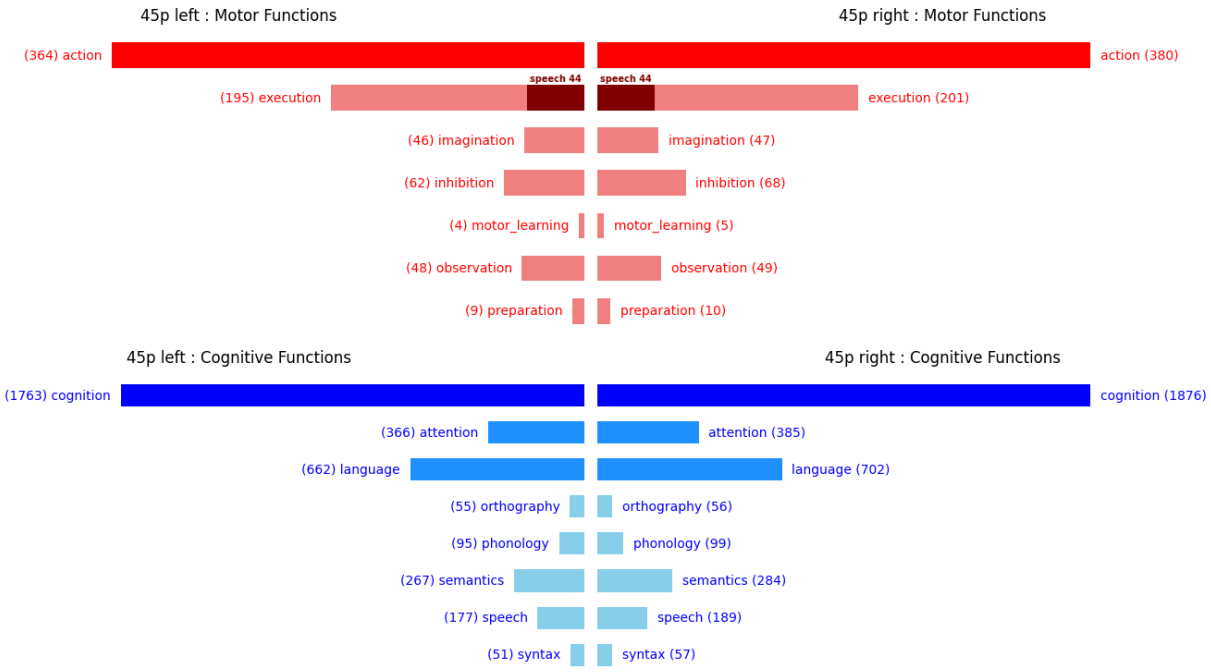

Figure 24 Functional associations of cytoarchitectonic area 45p in left and right hemispheres. Area 45p exhibits high bilateral engagement, with cognitive domains – particularly language, attention, and semantics – dominating its functional profile.

Action–related subdomains, such as execution and inhibition, are consistently represented in both hemispheres. Vertical bars show the number of experiments from BrainMap (red: action; blue: cognition). The balanced hemispheric distribution underscores 45p's role as an integrative hub linking motor and higher-order cognitive processes.

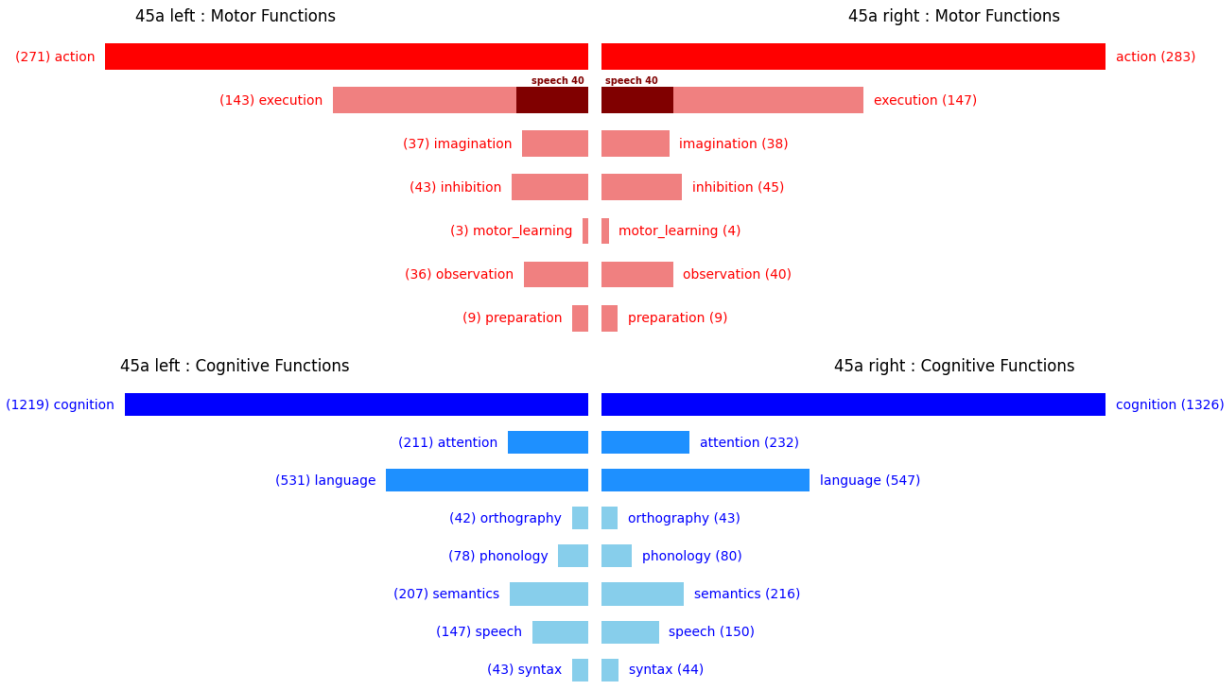

Figure 25 Functional associations of cytoarchitectonic area 45a, left and right hemispheres. Area 45a displays robust bilateral associations across both action and cognition domains, with slightly higher counts in the right hemisphere. Action execution and inhibition contribute prominently to motor-related activity, while language, attention, semantics, and speech dominate cognition. Bars indicate BrainMap experiment counts (red: action; blue: cognition). The distribution highlights 45a's involvement in the coordination of language and executive functions with motor planning, like 45p but with a subtle rightward bias.

3.11.2 Co-Activation Analysis of Premotor Area 6r1 and Broca's Region Subdivisions

To characterise functional differentiation within PM area 6r1 and areas 44p, 44a, 45p, and 45a, a series of MACM comparisons was conducted. Pairwise contrasts were organised based on the results of the MDS and cluster analyses to assess whether areas with similar structural properties also exhibit similar co-activation profiles. Importantly, the MACM analyses were used to evaluate whether the proposed subdivisions of areas 44 and 45 are associated with distinct functional connectivity patterns. Direct comparisons between the subdivisions of areas 44 and 45 were therefore performed to identify shared and region-specific co-activation networks.

Across all MACM analyses, premotor area 6r1 and the areas 44p, 44a, 45p, and 45a exhibited both shared and hemisphere-specific co-activation patterns. In the left hemisphere, MACM results revealed a consistent fronto-parietal core network encompassing inferior frontal, premotor, intraparietal, and temporo-parietal regions, accompanied by systemic area-specific extensions. Areas 44p and 45p showed stronger associations with dorsal premotor, posterior parietal, and thalamic systems, whereas areas 44a and 45a exhibited more focal coupling with opercular, insular, and occipitotemporal regions.

In the right hemisphere, co-activation profiles were more selective and spatially restricted, with a smaller shared core across inferior frontal, premotor, and insular regions. Area 44p right demonstrated pronounced co-activation with bilateral thalamic and premotor networks, whereas area 44a showed fewer unique co-activations, with preferential engagement of limbic or higher-order frontal regions. The following sections report MACM results in a structured comparison sequence. Analyses begin with the left hemisphere, where co-activation patterns were more extensive and allowed for detailed

characterisation of premotor area 6r1 and area 44p, followed by direct contrasts between areas 44p and 44a and between areas 45p and 45a. Further comparisons examine co-activation patterns between areas 44p and 45p and between areas 44a and 45a. Finally, corresponding analyses in the right hemisphere are reported to assess hemispheric similarities and differences in co-activation profiles.

3.11.2.1 Co-activation Patterns of Left Areas 6r1 and 44p

The MACM-derived co-activation clusters of areas 6r1 and 44p (left hemisphere) were intersected with the 577 cytoarchitectonic maps of the Julich-Brain Atlas (Fig. 26). For each region, map value, map containedness, and input containedness were computed. Thresholds were then applied to identify shared and region-specific anatomical correspondences:

- Shared (6r1 and 44p): map containedness > 0.30; input containedness > 0.50
- 6r1-specific: map containedness > 0.50; input containedness > 0.03
- 44p-specific: map containedness > 0.03; input containedness > 0.10

Only regions that passed these thresholds were included in the analyses. All thresholded areas are presented in the supplementary material (Tab. 1-3). Areas 6r1 and 44p shared a set of inferior parietal lobule (IPL): supramarginal gyrus (PFcm, PF, PFop, PFm), and rostral angular gyrus in the right hemisphere (PGa); intraparietal sulcus (IPS): hIP1, hIP2, hIP3, hIP6; and posterior superior temporal cortex (TPJ): Te 2.2, the broader temporo-parietal junction (TPJ) region. Together, these areas constituted a shared IPL-IPS-TPJ network associated with both 6r1 and 44p areas.

Regions uniquely linked to 6r1 after thresholding were in dorsal frontal and ventro occipito-temporal cortex (PM region (area 6d3), fusiform gyrus (areas FG1, FG2, FG3), ventral occipital cortex, lingual gyrus (hOc4v)). These areas indicated a 6r1-specific dorsal premotor and ventral visual-stream recruitments not observed for 44p.

At the same time, three posterior parietal regions selectively met the threshold for area 44p: superior parietal lobule (7P), posterior IPS (hIP5, hIP8). These regions comprised a posterior superior parietal lobule (SLP) and the posterior segment of the intraparietal sulcus (IPS) cluster, uniquely associated with 44p.

Although areas 6r1 and 44p are adjacent within the caudal inferior frontal cortex and rostral inferior premotor cortex, their MACM profiles showed both extensive overlap and clear region-specific differentiation, as reflected in the co-activation patterns.

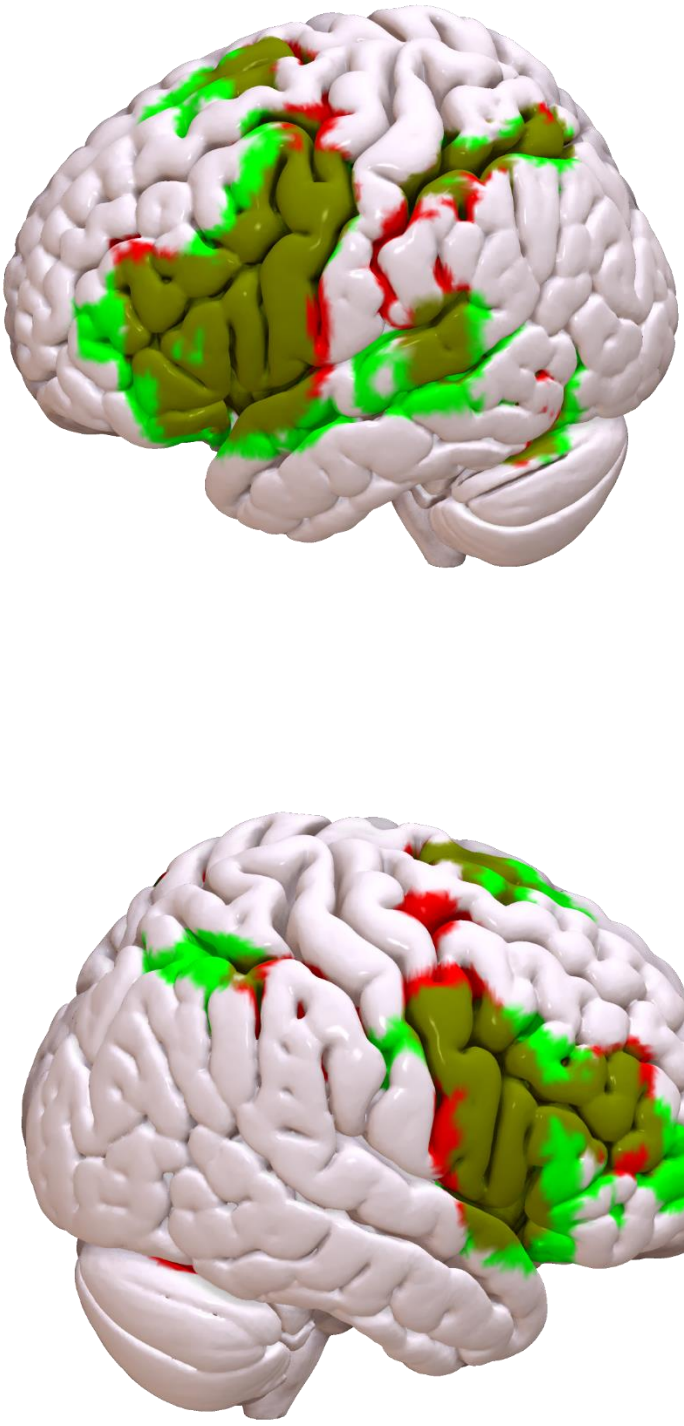

Figure 26 Co-activation patterns of left area 6r1 (red) and area 44p (green). Area 44p co-activation with ventral temporal and orbitofrontal regions, including parahippocampal, lingual, occipital, and hippocampal areas, reflecting engagement in associative and mnemonic processing. In contrast, 6r1 co-activated with dorsal premotor, thalamic, subcortical, and cerebellar structures, consistent with its role in motor-executive and integrative sensorimotor control.

3.11.2.2 Co-activation Patterns of Left Areas 44p and 44a

The MACM-derived co-activation clusters of areas 44p left and 44a left were compared with the Julich – Brain cytoarchitectonic maps (Fig. 27). Map containedness and input containedness values were calculated and thresholded as follows:

- Shared areas (44p and 44a): map containedness > 0.30 and input containedness > 0.30
- 44p-specific regions: map containedness > 0.10 and input containedness > 0.10
- 44a-specific regions: map containedness > 0.01

Only the regions passing these thresholds were included in the final analysis; all tables are provided in Supplementary Material (Sup. Tab. 1-21).

The MACM clusters of areas 44p and 44a showed convergent involvement of inferior frontal, intraparietal, and posterior temporal-parietal regions. Both areas were consistently assigned to: left Broca regions areas (44 and 45), and right area 45; shared IPS regions included (hIP1, hIP2, hIP3, hIP6), and TJP-related temporal areas (TPJ (STG/SMG), TE 2.2 (posterior STG). Further overlap was detected in precentral area 6v3 right, Op9 right, right insular subdivision Id8, and left ventral anterior thalamic nuclei (VA, VAmc). Together, these areas formed a joint IFG-IPS-TPJ-thalamic network co-activated by both areas 44p and 45a.

After thresholding, area 44p left showed a distinct set of posterior parietal and thalamic regions not shared with area 44a. The 44p specific posterior parietal cluster composed area 7A (posterior superior parietal lobule, right): hIP1, hIP2, hIP3, hIP6 (posterior/dorsal IPS, right). These areas collectively formed a posterior SPL-IPS complex, extending toward the parieto-occipital junction. A broader thalamic set was unique to 44p: VIM, VLP, VLA (ventral lateral subdivisions), VA, VAmc (ventral anterior nuclei), AV, AM (anteroventral and anteromedial nuclei), CL (central lateral intralaminar nucleus). These nuclei represent motor-related, modulatory, and sensorimotor integrative thalamic territories. Thus, the left 44p area-specific network was characterised by a posterior parietal and thalamic expansion beyond the overlap with area 44a.

Only two regions surpassed the threshold for left area 44a: Op1 (parietal operculum, left), Ig2 (posterior insula, left). These areas represent somatosensory-interoceptive opercular-insular territories not observed for 44p.

Despite their close anatomical proximity within the left inferior frontal cortex, left areas 44p and 44a exhibited both extensive overlap and clear dissociations, particularly reflected in the posterior parietal and thalamic connectivity that was specific to area 44p left and the opercular-insular contribution specific to area 44a left.

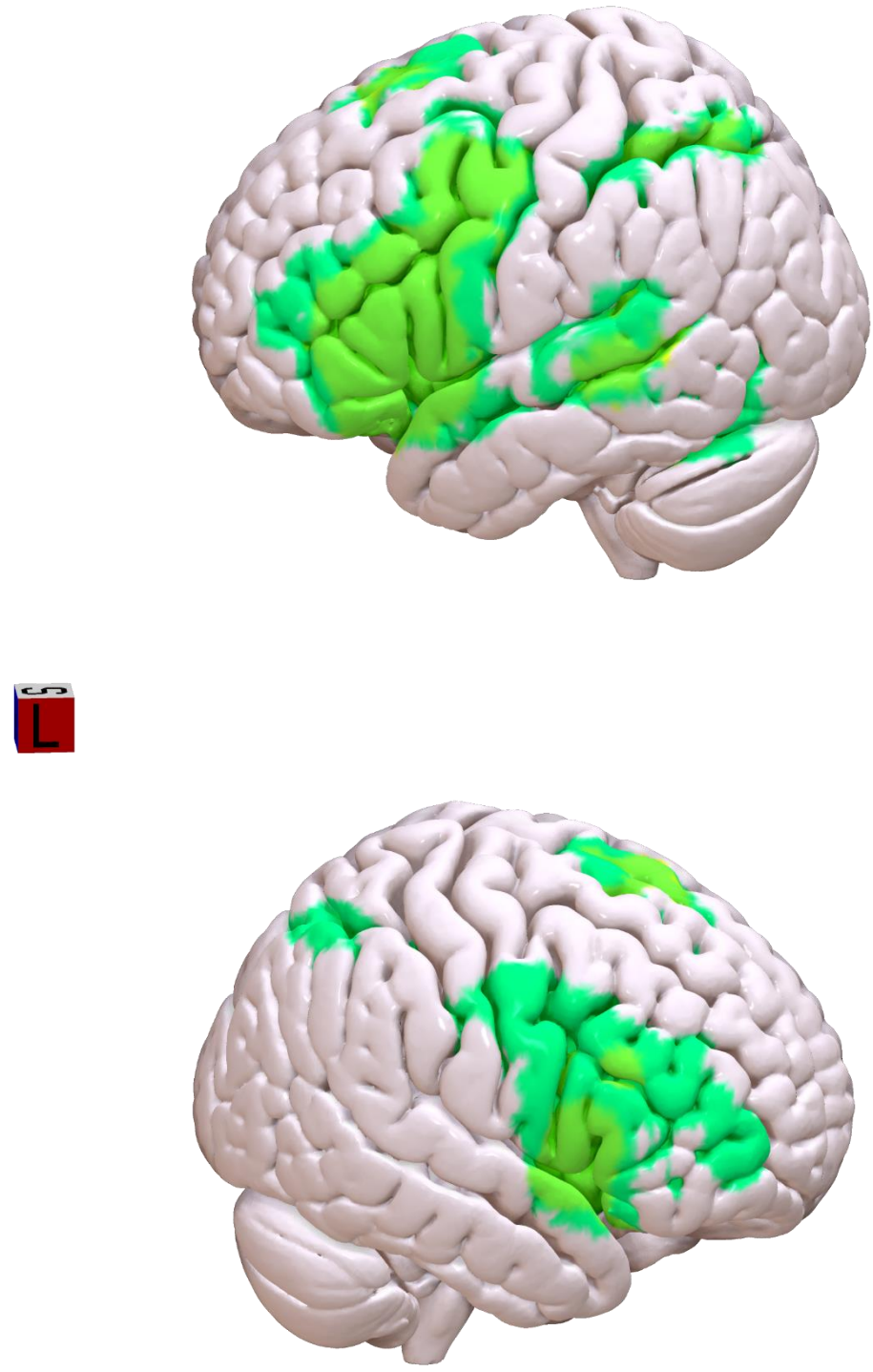

Figure 27 Co-activation patterns of left areas 44p (green) and 44a (yellow). Surface rendering shows overlapping and distinct co-activations for both inferior frontal subregions. Common activations were observed across frontal opercular, premotor, insular, and temporo-parietal cortices as well as thalamic and basal forebrain nuclei. Area 44p exhibited additional right-hemispheric and subcortical co-activations, including thalamic, ventral striatal, and hippocampal regions, whereas 44a showed more focal connections with orbitofrontal and insular areas.

7.2.3 Co-activation Patterns of Left Areas 45p and 45a

The MACM analysis for areas 45p left and 45a left identified distinct but partially overlapping co-activation patterns across the left inferior frontal gyrus (IFG), fronto-insular operculum, precentral premotor cortex, intraparietal sulcus (IPS), superior parietal lobule (SPL), and thalamus. (Fig. 28) From the full set of Julich-Brain cytoarchitectonic areas evaluated before thresholding, only those regions surpassing the predefined thresholds (map containedness and input containedness; see Supplementary Tables 13-15) were retained and are summarised below.

Both seeds showed convergent co-activation within the left posterior intraparietal sulcus, specifically overlapping in areas hIP1, hIP2, hIP3, and hIP6, as well as in the ventral lateral posterior thalamic nucleus (VLP) and portions of the superior parietal lobule (area 7PC). These regions correspond to the posterior parietal cortex involved in higher-order sensorimotor integration and domain-general associative processing. The consistent assignment of these parietal and thalamic nuclei across both seeds indicated a shared parietal-thalamic recruitment profile across the two subdivisions of the left are 45.

After thresholding (map containedness > 0.3, input containedness > 0.03), area 45p left demonstrated specific co-activation to posterior IPS areas hIP1, hIP2, hIP3, and hIP6, as well as the left VLP nucleus and SPL area 7PC, without involvement of frontal or insular territories that appeared for 45a. These findings indicate that area 45p left was associated with a comparatively parietally focused co-activation profile, with strong engagement of posterior IPS areas that are typically linked to visuo-spatial transformation, multisensory integration, and sensorimotor mapping.

In contrast, area 45a left showed a broader and more anteriorly distributed co-activation pattern. Unique regions included multiple subdivisions of the inferior frontal sulcus (IFS; IFS2, IFS4), inferior frontal junction (IFJ1, IFJ2), and left precentral premotor cortex areas (6v2, 6v3). Additionally, area 45a left was uniquely co-activated with the frontal operculum (Op9) and with anterior and posterior short insular gyri (Id7, Id8).

These assignments indicate that area 45a left was preferentially linked to fronto-opercular and premotor networks, encompassing regions implicated in cognitive-linguistic control, multimodal integration, and articulatory planning.

In summary, areas 45p left and 45a left showed partially overlapping but clearly dissociable co-activation profiles. Both subdivisions commonly engaged posterior parietal IPS regions and the ventral lateral posterior thalamus, indicating shared involvement in a domain-general integrative process. However, 45p left displayed a predominantly posterior parietal pattern focused on IPS and SPL regions, whereas 45a left uniquely recruited front-insular, premotor, and IFS/IFJ territories. This distinction reflected a functional gradient from a parietally oriented subdivision (45p) to a more fronto-opercular and premotor-integrative subdivision (45a).

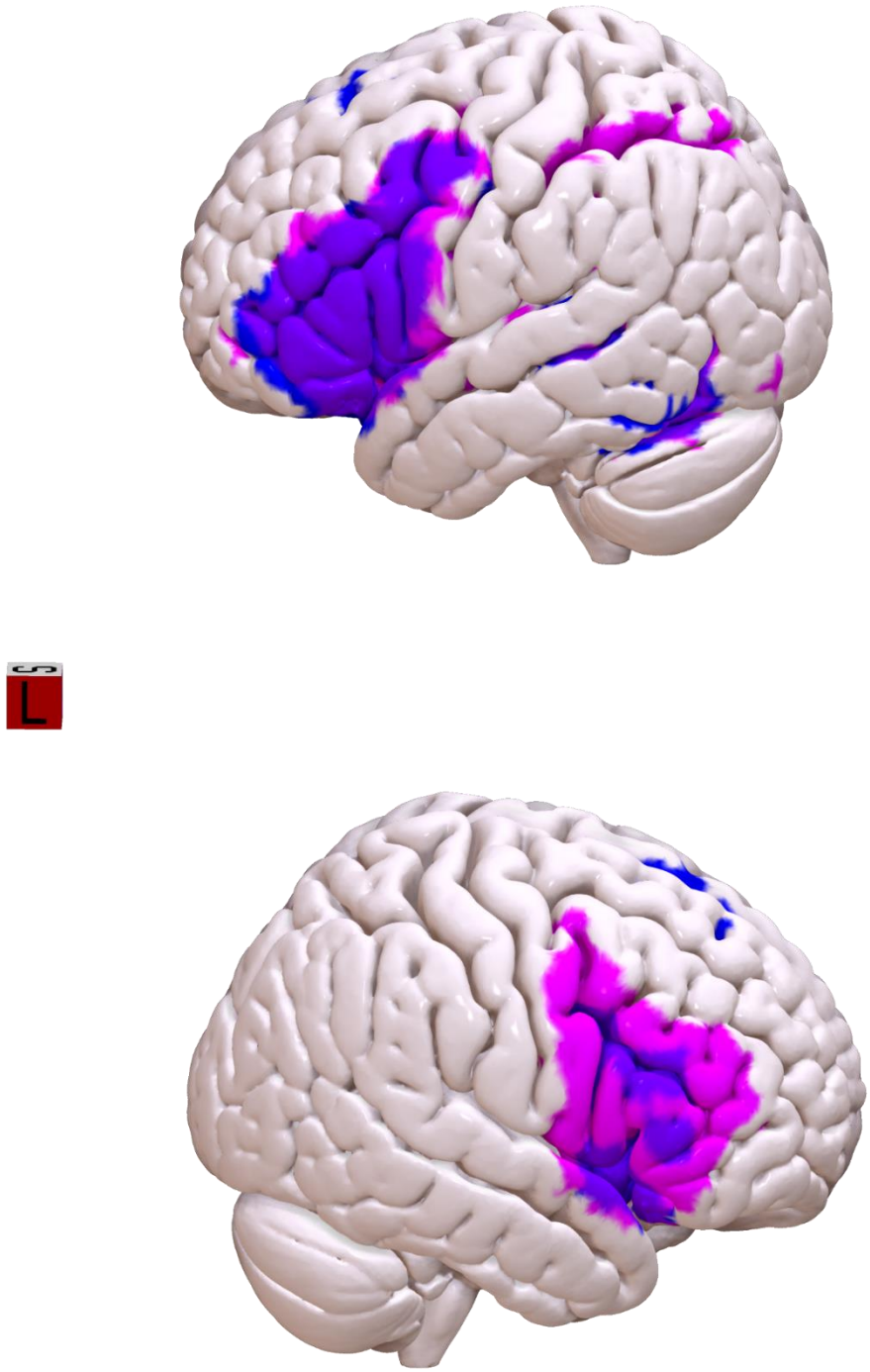

Figure 28 Co-activation patterns of left inferior frontal areas 45p (violet), 45a (blue). Both regions show extensive overlapping co-activation within a bilateral fronto-temporo-parietal network, including inferior and middle frontal gyri, premotor, and temporal cortices. Common activations encompass inferior frontal areas, including Broca's region, premotor regions (6d, 6v, 6r), inferior parietal lobule, and superior and middle temporal cortices. Unique to area 45p is broader engagement of thalamic, limbic, and subcortical structures, including the amygdala, hippocampus, and ventral striatum, indicating a stronger connection to affective and associative systems. In contrast, area 45a shows distinct co-activation in dorsomedial prefrontal and anterior cingulate regions, reflecting its involvement in higher-order executive and control functions.

7.2.4 Co-activation Patterns of Left Areas 44p and 45p

Meta-analytic connectivity modelling (MACM) revealed both shared and distinct co-activation profiles for areas 44p left and 45p left (Fig. 29). The overlap analysis identified a set of Julich-Brain cytoarchitectonic areas that were consistently recruited by MACM clusters of both areas when applying the thresholds of map cotainedness > 0.5 and input containedness > 0.1. These overlapping regions comprised primarily inferior frontal, insular, and precentral regions. For area 44p left, the most robustly co-activated regions included Id8 and Id6 (insula), Op6 (Frontal Operculum), 44 and 45 (IFG), and 6v2-6v3 (PreCG) on the left hemisphere. For 45p left, overlapping contributions were observed mainly in the inferior frontal gyrus (areas 44 and 45) and the associated right-hemispheric opercular and insular regions. Together, these findings demonstrate that both areas share a common frontal-insular-precentral core network, reflecting their joint involvement in higher-order cognitive and sensorimotor integration functions.

Non-overlapping regions highlighted distinct MACM results for each area. For 44p left, unique regions (map containedness > 0.1, input containedness > 0.2) were predominantly located in premotor, parietal, and mesial frontal territories. These included Area 6ma (preSMA), mesial SFG, and multiple intraparietal sulcus regions (hIP1-hIP6), indicating a comparatively stronger association of 44p with sensorimotor and visuospatial networks. In contrast, 45p left demonstrated unique contributions (map containedness > 0.1, input containedness > 0.01) within limbic and medial temporal structures, including CM, SF, MF, and VTM nuclei of the amygdala, as well as Ch4 (Basal Forebrain). This pattern suggests a more pronounced engagement of 45p in affective, mnemonic, and associative limbic circuity.

In summary, MACM results revealed that areas 44p left and 45p left share a frontal-insular-precentral co-activation network, but diverge substantially in their secondary association patterns: 44p left aligns more strongly with premotor and parietal systems, whereas 45p left preferentially engages limbic and medial temporal regions. These dissociations support a functional differentiation between the two adjacent inferior frontal regions despite their anatomical proximity.

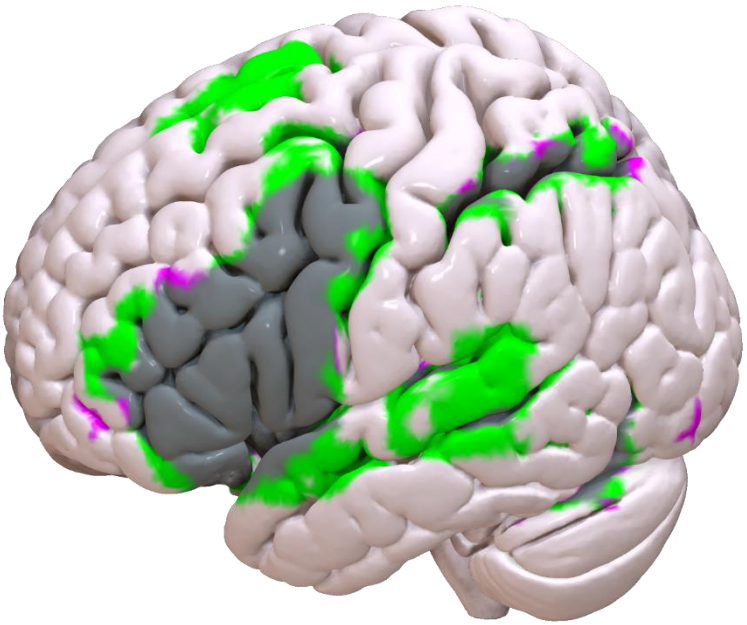

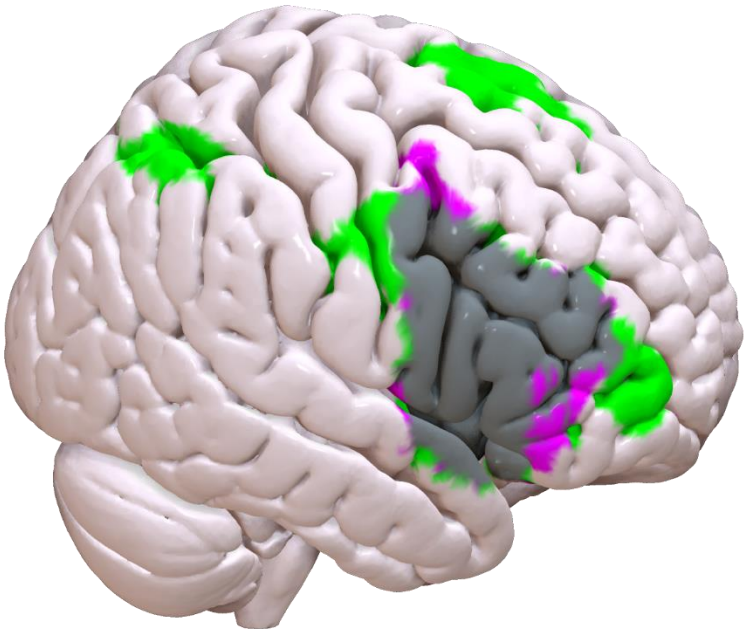

Figure 29 Co-activation patterns of left areas 44p (green) and 45p (violet). Area 44p co-activated mainly with dorsal frontoparietal and premotor regions. At the same time, 45p showed co-activations with ventral temporal, limbic, and subcortical areas, indicating a dorsal-ventral functional segregation within the left inferior frontal cortex.

7.2.5 Co-activation Patterns of Left Areas 44a and 45a

The MACM analysis identified a set of regions co-activated with both areas 44a left and 45a left (Supplementary Table 13). These overlapping territories were primarily located in the left temporo-parietal cortex, including the TPJ, STG (Te 2.2), and SMG, as well as within left inferior frontal regions corresponding to areas 44 and 45. Additional shared engagement was observed in the right IFG/Frontal Operculum (Op9 and area 45), indicating that both subdivisions participate in a broadly similar bilateral fronto-temporo-parietal network.

Distinct patterns were observed as well. Area 44a left showed exclusive associations with dorsal intraparietal sulcus regions (hIP1, hIP2, hIP3, hIP6) and with several thalamic nuclei, including MD, VA, and VAmc, AV, AM, and Pv (Supplementary Table 14). These unique connections suggest a preferential link between area 44a and parietal-thalamic circuits implicated in sensorimotor integration and higher-order cognitive control.

In contrast, area 45a left exhibited only two unique co-activation regions, both in ventral occipital cortex: hOc5 in the lateral occipital complex and hOc4v in the lingual gyrus (Supplementary Table 15). Although limited in number, these regions point to a specific coupling between area 45a and visual-perceptual processing pathways.

Overall, the results reveal substantial overlap in the networks associated with areas 44a and 45a, while also highlighting their distinct connectivity biases, area 44a toward dorsal parietal and thalamic systems, and area 45a toward ventral occipital systems.

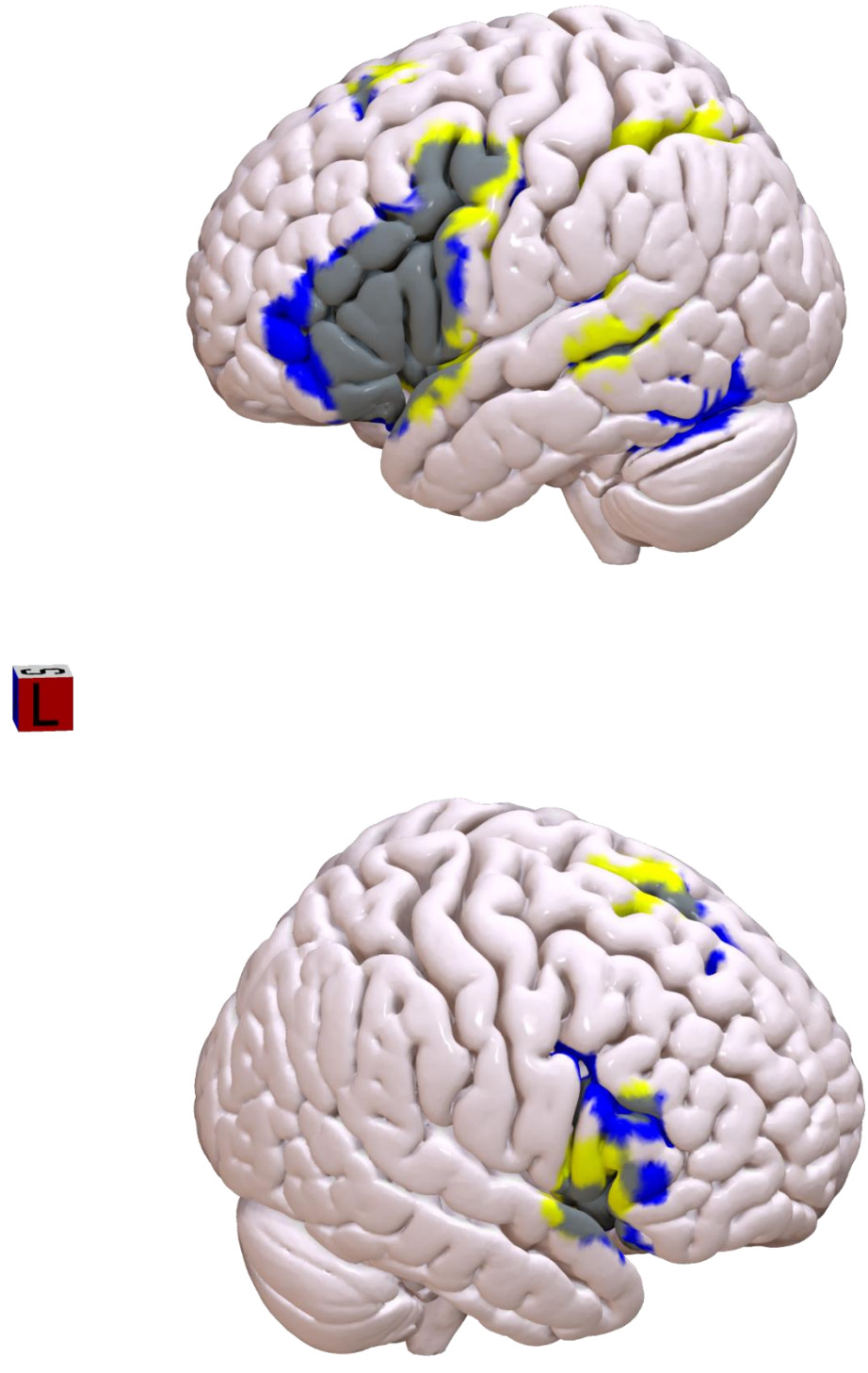

Figure 30 Co-activation maps of left inferior frontal areas 44a (green) and 45a (blue). Both areas show overlapping fronto-temporo-parietal co-activations. Area 44a extends toward thalamic and parietal sensorimotor regions, while 45a shows additional frontopolar, occipital, and parahippocampal co-activations, reflecting motor-control versus semantic-associative network involvement.

7.2.6 Co-activation Patterns of Right Areas 44p and 45p

The MACM revealed partially overlapping but functionally distinct co-activation profiles for areas 44p right and 45p right (Fig. 31). The overlap between the two regions was spatially restricted and primarily involved left insular cortex (Id6), left ventral premotor cortex (6v3), right pre-SMA/mesial SFG (6ma), and right IFG area 45, all exceeding the containment thresholds required for shared assignment. These regions represent a common frontal-insular-premotor network jointly engaged by both posterior IFG subdivisions.

Beyond these shared territories, 44p right showed a broader set of unique co-activations, predominantly involving bilateral thalamic nuclei, including ventral intermediate (VIM), ventral lateral posterior (VLP), ventral anterior (VA), ventral anterior magnocellular (VAmc), anterior intralaminar (CL), and ventral lateral anterior (VLA) nuclei. In contrast, 45p right displayed a limited number of unique regions that met the threshold criteria. Exclusive co-activation was observed in left fusiform areas (FG4, FG1, FG2), indicating a posterior ventral visual linkage not shared by 44p right.

Overall, the results demonstrated that while 44p right and 45p right converged within a common prefrontal-premotor-insular axis, 44p right engaged more extensive thalamic networks, whereas 45p right showed selective coupling with ventral occipitotemporal cortex.

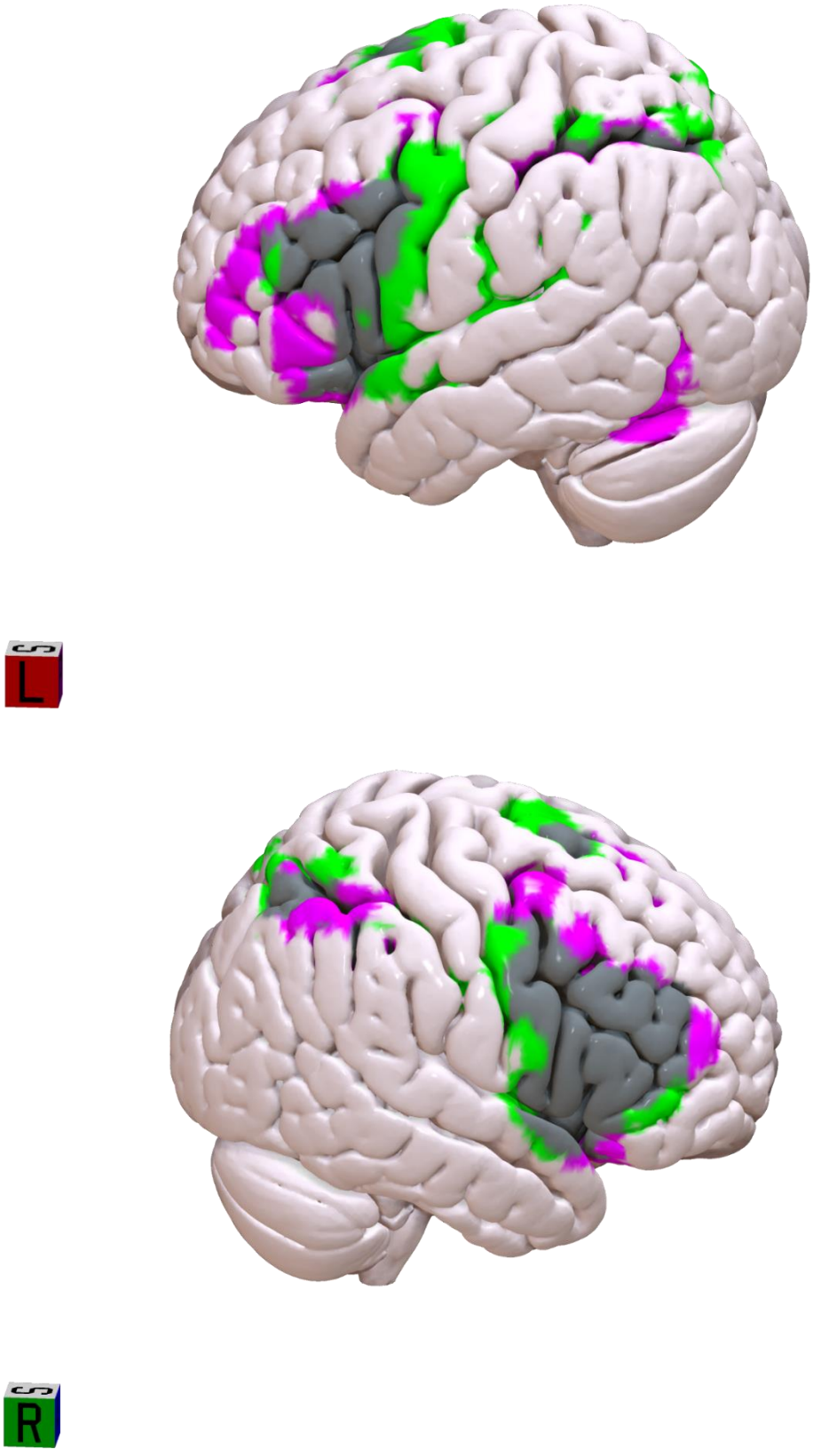

Figure 31 Co-activation patterns of right inferior frontal areas 44p right (green), 45p right (blue). The two areas show extensive overlap in frontal, parietal, and temporal cortices, with 44p displaying stronger subcortical connectivity and 45p more anterior and ventral cortical involvement.

7.2.7 Co-activation Patterns of Right Areas 44a and 45a

For areas 44a right and 45a right, MACM revealed partially overlapping but distinguishable co-activation networks (Fig. 32). Both areas showed convergent co-activation with bilateral IFG (areas 44 and 45), right frontal operculum (Op9), left ventral premotor cortex (6v3), and the Frontal I.2 gap-map, reflecting a shared fronto-opercular and premotor functional core. Additionally, both regions consistently engaged the intraparietal cortex (hIP1, hIP2, hIP3) and bilateral anterior intralaminar and ventral anterior thalamic nuclei, meeting the threshold criteria for overlapping assignment.

Beyond these common territories, 44a right exhibited a markedly broader set of unique associations. Exclusive co-activation involved an extended set of amygdalar nuclei (LB, Astr, IF, CM, SF, MF, VTM) and hippocampal HATA, indicating a preferential coupling with limbic-medial temporal structures not shared by 45a right. This pattern suggests that 44a right engages a more affective-mnemonic network component.

In contrast, 45a right presented only limited unique regions that met the containment thresholds, reflecting a more selective co-activation profile. The few exclusive areas identified were restricted to higher-order frontal territories, consistent with a more circumscribed functional specialisation relative to 44a right.

Overall, 44a right and 45a right shared a common fronto-parietal-thalamic architecture, while 44a right showed additional strong limbic connectivity, and 45a right remained comparatively restricted in its unique associations.

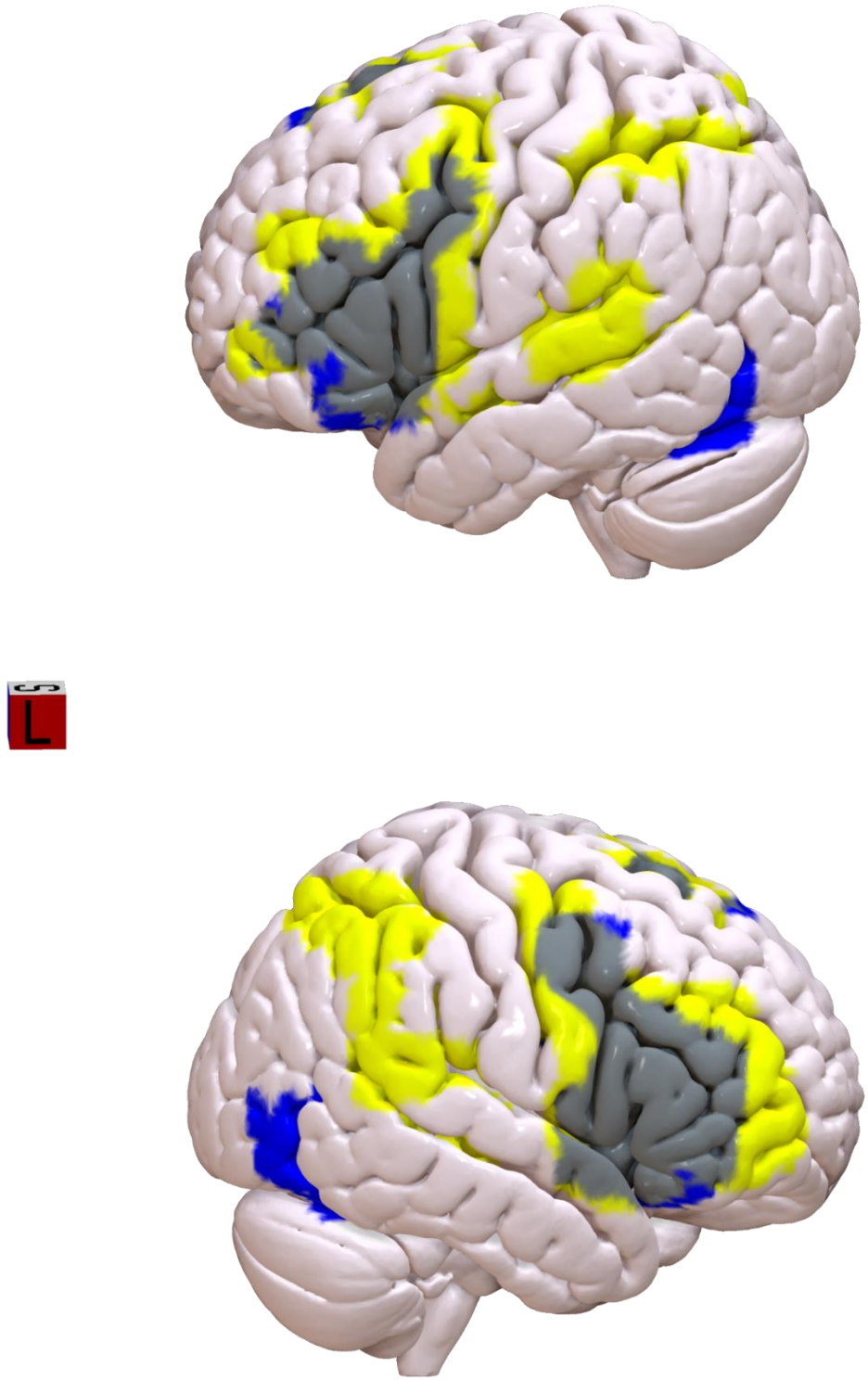

Figure 32 Co-activation patterns of right inferior frontal areas 44a (yellow), 45a (blue). The two areas show extensive overlap within bilateral inferior and middle frontal gyri, frontal operculum, and thalamic nuclei, alongside distinct patterns: area 44a extending into sensorimotor and parietal association cortices, and area 45a into occipitotemporal, hippocampal, and amygdaloid regions. This organisation supports right-hemispheric contributions to prosodic and integrative aspects of language processing.

3.12 Speech-Related Activity Lies Outside Broca's Region

Overlaying 3D maximum probability maps (MPMs) of Broca's region areas 44p, 44a, 45p, and 45a onto task-evoked electrocorticography (ECoG) recordings from the work of Liu et al. (2025) revealed a small overlap between areas of Broca's region and high kernel density estimates associated with articulatory and sequential complexity tasks (Fig. 33 B-C). The overlay suggests that the sequence complexity was mainly localised in the ventral portion of area 44a, with a smaller contribution in area 44p, whereas activations for articulatory complexity were largely located outside Broca's areas, in premotor cortex. The electrode density map provides a functional correlate for the spatial patterns observed in our MPM overlays (Fig.33 D-F). Zoomed views of regions of interest (Fig. 33 D-F) illustrate spatial distribution. Activation during pre-speech lies largely outside Broca's areas. Together, these findings indicate a functional separation between traditional language areas and motor execution circuits, highlighting the premotor cortex as the primary cortex for articulatory control during speech.

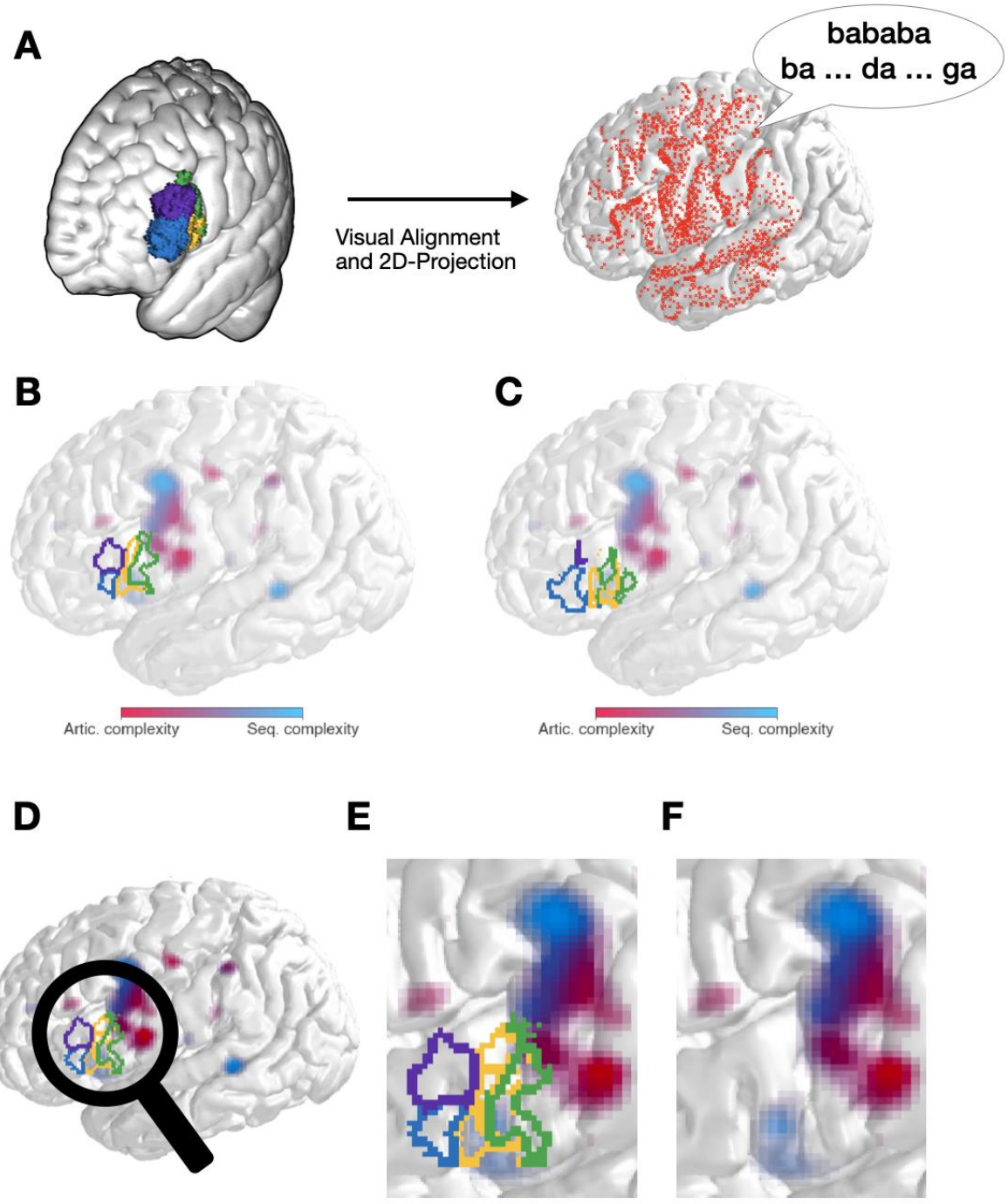

Figure 33 Overlay of the MPMs of the areas of Broca's region with task-evoked ECoG activity: Left-hemisphere MPMs of areas 44p, 44a, 45p, and 45a were loaded into the ICBM 152 2009c asym reference space volume as contours. The volume was then cropped to the left hemisphere, which, together with the MPMs, was visually aligned using the Software Napari (rotation and translation) and projected onto the left MNI-lateral image used in Liu et al. (2025). Red crosses indicate electrode positions used for high-density ECoG recordings. Patients were instructed to produce different syllables with and without cortical stimulation. B-C Projection of volume slices of the MPMs onto the MNI-lateral image, shown from lateral to medial. Red and blue indicate kernel density estimates of activity during articulatory and sequential complexity tasks. D-F Zoomed view of a region of interest (ROI), with saturated colours to improve visibility of overlaps between sequential MPMs and electrode signals. D shows the ROI. E shows the same ROI without MPMs. F shows the electrode signal only.

4. Discussion

This study introduces maps of four cytoarchitectonic areas 44p, 44a, 45p, and 45a in Broca's region, providing information about spatial localisation and interindividual variability. According to the functional subdivision of area 44 (Fabbri-Destro & Rizzolatti, 2008; Papitto et al., 2024; Zaccarella & Friederici, 2015; Zaccarella et al., 2021),two cytoarchitectonically distinct areas 44p and 44a have been identified, that share cytoarchitectonic features of previously identified area 44. Thus, cytoarchitecture supports the hypothesis resulting from functional imaging studies (Clos et al., 2013) that area 44 is not uniform, but it contains two distinct areas: anterior 44a and posterior 44p. Macroanatomically, areas 44p and 44a differed in topographic stability and sulcal associations. Area 44p consistently occupied a posterior position anchored to the prCS, whereas area 44a was situated more rostrally and exhibited greater interindividual variability. The anterior border of area 44p, its transition to area 44a, shifted according to the presence and depth of the DS in the left hemisphere and was often aligned with the RA on the right. Consequently, the 44p-44a border was not defined by a single macroscopic feature but reflected the transition from the stable prCS-anchored territory of area 44p to the sulcal variability characteristic of area 44a. This pattern corresponded with variability described in the literature, where in the RA and RH of the SF, which were present in over 98% of hemispheres, but displayed multiple configurations that influenced the relative positions of surrounding cortices and the macroscopic landmarks used to delineate these areas (Keller et al., 2009; Wang et al., 2022). The rostral border of area 44a with area 45p was more consistently associated with the RA, serving as an approximate landmark for the transition from opercular to triangular parts of the IFG. However, variability in sulcal morphology resulted in differences in the precise location of this boundary along the opercular-triangular junction. In some cases, area 44a extended slightly anteriorly before transitioning to area 45p at the level of the RA, whereas in others, the border coincided directly with the sulcal fundus or rostral bank of the RA. These observations indicated that the 44a-45p border, although guided by the RA, was gradual rather than sharply demarcated, tapering across the opercular-triangular junction. The border, therefore, reflected both the structural continuity of cytoarchitecture and dependence on local sulcal morphology, highlighting variable yet topographically constrained organisation of the rostral Pars opercularis (Keller et al., 2009; Wang et al., 2022). Area 45p occupied the Pars triangularis and transitioned anteriorly into area 45a, the most rostral subdivisions of area 45. Surface localisation of area 45a varied: in most hemispheres, it began at the rostral bank of the TS, while in others it arose at the rostral bank of the RA or spanned both sulci, reflecting a broader rostro-caudal placement. Caudally, area 45a reached the fundus or caudal bank of the HR in all left hemispheres and in most right hemispheres, whereas in some it extended several millimetres beyond the RH, indicating anterior spread in some individuals. These findings highlighted a gradual yet anatomically constrained transition from area 44a through area 45p to area 45a, shaped by the relative positions of the RA, TS, and HS, and reflecting both individual sulcal variability and continuity of cortical organisation in the anterior IFG (Keller et al., 2009; Wang et al., 2022).

Comparative findings supported these observations, demonstrating that sulcal variability of the frontal operculum was substantial within and across species. In humans, for example, the presence of sulci, such as the DS, increased the cortical volume and intrasulcular surface area of the Pars opercularis, yet population-based asymmetry was not consistently observed (Keller et al., 2009). Our results further showed that for area 44p, hemispheres with a DS had higher median normalised volumes (median = 1.251) than those without a DS (median = 0.781), although this difference was not statistically significant ($p=0.3834$). In area 44a, hemispheres with a DS also exhibited higher median volumes (median = 1.094) compared to those without (median = 0.605), and this difference approached significance ($p = 0.0572$), suggesting that DS morphology may influence the anterior portion of area 44. These results indicate that the presence of DS contributes to local volumetric variability,

particularly in area 44a, reflecting morphological heterogeneity within the rostral part of area 44 in Broca's region. Sex-and hemisphere-related volumetric patterns of this study further contextualised the organisation of Broca's region. Males showed larger absolute and normalised regional volumes than females across most areas, accompanied by consistently greater variability, particularly in areas 44a and 45p, suggesting increased morphological heterogeneity in males. Despite these overall size differences, the pattern of hemispheric lateralisation was consistent across sexes: area 44p showed a clear leftward volume asymmetry, reaching significance before correction, and area 44a exhibited a similar but non-significant leftward trend. In contrast, areas 45p and 45a displayed no meaningful hemispheric difference in volume, indicating relative symmetry in the anterior triangular part. This pattern, according to cytoarchitectonic work by Amunts et al. (1999; 2003), who demonstrated significantly larger left-hemispheric volumes of area 44, while finding little or no asymmetry in area 45. Similarly, Uylings et al. (2006) reported robust leftward volumetric asymmetry of area 44 but inconsistent asymmetry of area 45, reinforcing that posterior IFG cortex is more strongly lateralised. Complementary MRI-based morphometric evidence from Keller et al. (2009) also showed leftward volume asymmetry of the Pars opercularis, linked to the asymmetric presence of the diagonal sulcus. In this context, our findings that leftward volume asymmetry was stronger in posterior IFG subdivisions (areas 44p and 44a) and weakest or absent in anterior ones (area 45p, and 45a) fit well within the broader anatomical literature. Although there were no significant overall volume differences between males and females, the interaction between hemisphere and sex showed that lateralisation differed between the sexes. This effect was mainly driven by area 44a, where males tended to show a stronger leftward asymmetry than females. Together, these findings underscored that macroscopic transitions between areas 44p, 44a, 45p, and 45a were shaped by local sulcal morphology, interindividual variability, and cytoarchitectural continuity rather than fixed anatomical landmarks alone, emphasizing the complex but constrained structural organisation of Broca's region. Together, these findings demonstrate that the cytoarchitectonic organisation of Broca's region is both highly structured and shaped by considerable interindividual variability. The clear distinction between areas 44p and 44a supports functional models proposing posterior and anterior subcomponents within area 44, while the gradual transition toward areas 45p and 45a reflects a continuous yet anatomically guided organisation of the Pars opercularis and Pars triangularis of the IFG. Sulcal morphology, particularly the configuration of the DS, RA, TS, and RH, emerged as a major contributor to variability in both area boundaries and local volumes, with the DS exerting a measurable influence on the size of anterior area 44. Additionally, hemispheric lateralisation was most pronounced in the posterior subdivisions, consistent with cytoarchitectonic and MRI-based evidence of leftward specialisation in the Pars opercularis. Smaller sex-dependent effects further seemed to modulate this pattern, indicating that both biological and morphological factors shape the structural architecture of Broca's region. Importantly, the present results suggest that different Broca's region areas contribute to hemispheric specialisation to varying degrees, with area 45a showing high lateralisation, suggesting that this region may contribute to left hemisphere dominance (Trettenbrein & Friederici, 2025). Functional peak mapping from the fMRI studies onto the pmaps of the areas 44p, 44a, 45p, and 45a showed that in the left hemisphere, syntactic and semantic activations predominantly overlap with areas 44p, 44a, and 45a. Lexical and phonological processing primarily involved area 44a and adjacent opercular areas, whereas action-related activations engaged area 44p, as well as premotor and opercular areas. Area 45p was mainly involved in semantic processing. The right hemisphere included fewer peaks, mainly in premotor areas 44p and the insula. Together, these findings suggest a close structure-function relationship within Broca's region, where anteriorly located areas (44a, 45a, and 45p) contribute to higher-level language functions such as syntax and semantics, and posterior area 44p supports syntactic and action-related motor processes (Gallardo et al., 2023). The asymmetrical distribution of activations, with the left hemisphere showing extensive language-related peaks, further supports the

link between cytoarchitectonic lateralisation and functional specialisation in Broca's region. Large-scale functional connectivity analyses also show that left language networks exhibit stronger connectivity and lateralisation than right homologues, and that diminished leftward asymmetry is associated with language-related cognitive differences (Amelink et al., 2024).

Historical and more recent maps of Broca's region show both similarities and notable differences to the present map, particularly in terms of the number, arrangement, and extension of the areas (see section 1.1). One example is the pilot study from our lab by Amunts et al. (2010), which motivated this cytoarchitectonic mapping work from a receptorarchitectonic perspective. However, this receptor mapping was performed on only six hemispheres from three post-mortem human brains, which limited the assessment of interindividual variability. At the same time, it provided high spatial resolution and detailed receptor profile maps derived from in vitro autoradiography of six neurotransmitter receptor types. This study revealed that area 45 comprised two receptorarchitectonic distinct areas in anterior-posterior orientation (45a and 45p), which closely correspond to the subdivisions identified in the present cytoarchitectonic mapping. Area 44 was also subdivided into two areas, but in a ventral-dorsal orientation (44v and 44d). By contrast, the current systematic cytoarchitectonic mapping demonstrated a clearer anterior-posterior organisation within area 44, with subdivisions designated as 44a (anterior) and 44p (posterior). Similarly, Fan et al. (2016) identified five areas in Broca's region, with areas 44 arranged ventrally and dorsally, including an additional area 44op located in the depth of the SF of the IFG, corresponding to insular area Id7 ($p = 0.56$) in the Julich-Brain Atlas. Areas 45r and 45c, in turn, followed an anterior-posterior orientation.

Differences between historical, receptor-, and MR-based maps of Broca's region may arise from both interindividual variability and methodological differences. Historical maps often relied on visual inspection of one or a few hemispheres, making it difficult to distinguish cytoarchitectonically similar areas. By contrast, the use of quantitative measures and statistical criteria in a sample of ten brains allowed a reproducible identification of areas, although their locations and volumes varied between individuals.

The high interindividual variability in this region (Keller et al., 2009; Tomaiuolo et al., 1999) is now quantified through probabilistic maps of the four areas. While MR studies cannot achieve the cellular resolution of histology, they enable analysis of larger samples at the group level as compared to the present study. However, group-level analyses are challenged by spatial variability: regions with lower variability are more likely to reach statistical significance, whereas highly variable areas may be missed, potentially yielding false-positive or negative findings (Mueller et al., 2013; Zilles & Amunts, 2013). Differences in pre-processing pipelines, spatial smoothing, software, and thresholding further contribute to variability in MR-based parcellations (Botvinik-Nezer et al., 2020), explaining the inconsistencies observed between MR and histological maps of Broca's region (Brodmann, 1909; Fan et al., 2016; Glasser et al., 2016). Overall, these findings highlight that interindividual variability is a fundamental feature of Broca's region and underscore the value of integrating cyto-, receptor-, and MR-based approaches for a comprehensive understanding of its organisation.

The new cytoarchitectonic maps provided a highly resolved characterisation of Broca's region and its adjacent ventral premotor and insular areas. Because the maps were derived from ten post-mortem human brains based on histological analysis, they captured sulcal variability and microstructural borders with far greater spatial precision than is achievable with current in vivo MRI. This high-resolution representation enabled us to localise functional activation peaks from prior studies to specific cytoarchitectonic areas within Julich-Brain Atlas v3.1. In doing so, we refined existing anatomical interpretations of language- and action-related activations and revealed the underlying microstructural heterogeneity of classical Broca's region.

In all three published fMRI studies that were examined in section 3.10 (Goucha & Friederici, 2015; Papitto et al., 2024; Zaccarella & Friederici, 2015), the reported functional peak activations were originally assigned to the cytoarchitectonic areas. Upon re-examination using the probabilistic cytoarchitectonic maps of the Julich-Brain v3.1, and the new areas 44p, 44a, 45p, and 45a, these peaks could be more precisely localised. As a result, many activations were more accurately assigned to distinct cytoarchitectonic areas 44p, 44a, ifs4, 6r1, 6v2, 6v3, Op5, Op9, Id7, and Id8 (Table 13, Section 3.10), thereby providing a finer-grained understanding of the structure-function relationship of these areas with respect to functions reported in the studies. For example, Zaccarella et al. (2015) reported peak activations in the anterior dorsal insula (adINS). When we mapped these coordinates to the Julich-Brain, both left and right peaks were assigned to Id8 with probabilities of p = 0.6 and 0 = 0.5, respectively. This finding indicated that activations previously labelled as "FOP/adINS" fell within a specific dorsal insular subdivision, which is known to support lexical-phonological processing and phonological-semantic control. Similarly, all three peaks that Zaccarella attributed to the Pars opercularis (BA44) were assigned to area 44p with probabilities ranging from p = 0.26 to p = 0.57, confirming involvement of posterior BA44 in syntactic *Merge* operations and structural complexity processing. Goucha et al. (2015) reported peaks in BA 44 and BA45 during conditions manipulating hierarchical syntactic structure and semantic content. Several BA44 peaks were localised to ifs4 (with p-values of 0.3, 0.5, and 0.2), a dorsal opercular subdivision implicated in binding hierarchical syntactic structure and supporting syntax without meaning. A separate BA44 peak was localised to 44a (p = 0.49), corresponding to core syntactic processing independent of semantics. Importantly, two peaks that Goucha labelled as BA44 were assigned to area 6r1 with probabilities p = 0.6 and p = 0.3, demonstrating that some syntactic computations attributed to BA44 were actually situated within the ventral premotor cortex. Peaks originally assigned to BA45 were mostly localised to areas 45a, 45p, and OP9, confirming their role in semantic integration, morphological processing, and lexical-semantic control. Finally, "anterior insula" peak mapped to Id7 (p = 0.5), providing a precise structural correlate for syntax-related processing in dorsal insula. Papitto et al. (2024) investigated category processing in phrases and rule-based action sequence structuring, reporting numerous peaks in BA44, BA47, BA6, and the insula. Our cytoarchitectonic mapping clarified these assignments substantially. The right-hemisphere peak labelled as BA44 was located at (57,11,22) and was assigned primarily to area 6r1 (p = 0.5) and secondarily to area 44p (p = 0.34). Published peak coordinates can differ from the precise underlying anatomy because of pre-processing effects such as spatial smoothing and normalisation/interpolation, which blur the signal and can systematically bias the localisation of peak foci by several millimetres and even toward neighbouring regions with Gray-matter content (Luppi et al., 2024; Sacchet & Knutson, 2013). This result demonstrated that the reported BA44 activation overlapped the interface of ventral premotor cortex and posterior BA44, consistent with the combined linguistic and action-sequence functions described in the study. Peaks labelled as BA6 were distributed across 6v3 (p = 0.8), Op5 (p = 0.5), and 6v2 (p = 0.7), indicating that multiple premotor subregions contributed to rule-based motor and structural sequence planning. A peak assigned to Pars orbitalis (BA47) was instead mapped to Id8 (p = 0.6), reflecting the dorsal insula's role in monitoring and adapting syntactic rule processing. Finally, three peaks labelled as "insula" or "BA45" fell consistently within Id7 (probabilities of p = 0.4, 0.6, and 0.5), capturing dorsal insula involvement in syntactic hierarchy tracking, rule integration, and executive control of syntactic and semantic operations. Taken together, these findings demonstrated that functional activations attributed to BA44 and BA6 in the literature were frequently distributed across microstructurally distinct subregions. In particular, peaks falling within areas 44p and 6r1 were highly informative. Posterior area 44 (44p) has been associated with articulatory planning, syntactic *Merge*, and structural computation, whereas the newly defined ventral premotor area 6r1 (Ruland et al., 2025) lies at the interface of motor and language-related circuity and supports coordinated action-language processing. Notably, Friederici (Friederici, 2011,

2017a) proposed that syntactic *Merge* and action-related processing co-occur within BA44, suggesting a functional distinction between anterior and posterior portions of the area. Our fine-grained cytoarchitectonic mapping provided an anatomical substrate for this hypothesis: area 44p, 44a, and the intermediate areas 6r1 may mediate integrative functions bridging motor and linguistic processing. The present results show that several syntactic and rule-based computations reported in earlier fMRI studies relied on both area 44p and premotor area 6r1, indicating Broca's region, which integrates linguistic, motoric, and domain-general control functions, and confirms Friederici's functional distinctions with an underlying microstructural basis. By applying the latest version of the probabilistic cytoarchitectonic atlas (Julich-Brain Atlas v3.1), we were able to reassign peaks previously reported within broad microanatomical categories (BA44, BA45, BA47, BA6, insula) to specific microstructural fine-grained areas, clarifying the structural basis of linguistic, motor, and integrative computations. The probabilistic nature of the new maps accounted for inter-individual variability, reducing the risk of mislocalisation inherent to deterministic macroanatomical labels. Even when working with previously published fMRI peaks, Julich-Brain allows a more anatomically precise assignment of functional activations than broad microanatomical labels, supporting a clearer interpretation of how distinct areas contribute to linguistic, motor, and integrative computations.

By implementing all peak assignments directly into Julich-Brain, we leveraged histology-based probabilistic maps to achieve microstructural precision beyond what broad microanatomical labels can provide. The remapping of areas 44 and 45 into 44p, 44a, 45p, and 45a, together with the ventral premotor area 6r1, allowed us to assign functional activations to well-defined cortical areas, providing a structural foundation for interpreting their distinct linguistic, motor, and integrative roles. More broadly, the present study illustrates how high-resolution cytoarchitectonic mapping can serve as a foundational layer for digital brain research, supporting multimodal integration, probabilistic localisation, and reproducible interpretation of functional data, as outlined in recent visions for the coming decade of digital neuroscience (Amunts et al., 2024). While recent probabilistic atlases such as NextBrain (Casamitjana et al., 2025), Brainnetome (Fan et al., 2016), Automated Anatomic labelling (AAL) atlas (Rolls et al., 2020), and the Human Connectome multimodal parcellation (Glasser et al., 2016) offer important advances in whole-brain labelling, connectivity-based parcellation, or multimodal structural–functional integration, they lack the microstructural resolution required to distinguish areas such as 44p, 44a, 45p, 45a, and 6r1. Accordingly, the Julich-Brain Atlas provides the most precise framework for linking fMRI peaks to cytoarchitectonic structure, enabling a refined interpretation of how Broca's region supports syntactic processing, semantic integration, and the coordination of action-language function.

The present findings provide evidence that areas 44p, 44a, 45p, and 45a capture functionally meaningful distinctions that are not accessible using broader anatomical or connectivity-based atlases. By projecting peak activation coordinates from carefully selected functional neuroimaging studies onto histology-based probabilistic maps (section 3.10), this work establishes a direct structure-function relationship at a microarchitectonic level. The close correspondence between functional activations and cytoarchitectonic boundaries shown in Fig. 19A indicates that language-related computations are constrained by fine-grained cortical architecture rather than by classical macroscopic labels. One outcome of this analysis is hemispheric asymmetry in both the density and diversity of functional activations. As illustrated in Fig. 19B and quantified in Table 13, the left hemisphere exhibited a dense and functionally heterogeneous clustering of coordinates across syntax, semantics, action, and lexical-phonological domains. In contrast, the right hemisphere showed only sparse activation, limited to action, syntax, and semantic processing, with no coordinates corresponding to lexical or phonological functions. Within the left hemisphere, substantial spatial dispersion was observed across all functional domains, particularly for syntactic processing, which showed variability exceeding 20 mm along all

three anatomical axes (Section 3.10 Table 13). This wide dispersion suggests that syntactic operations are distributed across multiple areas, primarily involving areas 44a, 44p, and 45a (Section 3.10 Fig. 19.A). Similarly, semantic processing displayed pronounced depth-wise (z-axis) variability, indicating engagement of adjacent cortical layers and neighbouring regions. These findings provide a microstructurally grounded perspective on Broca's region, supporting network-based models in which higher-order linguistic functions emerge from interactions among multiple functionally specialised cortical areas. The observed functional distributions align closely with the dual-stream model of language processing (Eichner et al., 2024; Friederici, 2017a; Nakae et al., 2020). Dorsal stream pathways are implicated in sensorimotor integration and syntactic sequencing, whereas ventral stream pathways support semantic processing and combinatorial meaning. Syntactic and action-related activations were predominantly localised within areas 44a, 44p, and ventral premotor regions (including area 6r1), consistent with dorsal stream engagement, while semantic-related activations in area 45a and adjacent opercular areas correspond to ventral stream functions (Fig. 19A). The partial spatial overlap between these domains suggests that Broca's region functional as an interface between dorsal and ventral streams, integrating structural, semantic, and action-related information during language processing. These findings support network-based models and challenge the classical modular view of Broca's region, emphasising that higher-order linguistic computations emerge from coordinated activity across multiple interacting microstructural areas.

The fine-grained functional organisation revealed in this study is relevant for neurosurgical planning and outcome prediction. The substantial spatial dispersion observed across left-hemispheric language areas (Section 3.10, Table 13) provides further evidence that language deficits cannot be reliably predicted based on gross anatomical landmarks alone. Integrating these functional maps with clinical measures such as lesion-activation distance (LAD) has demonstrated that tumours located within 10 mm of functionally defined Broca's region are associated with significantly reduced verbal fluency and impaired sentence verification (Riley et al., 2022). The cytoarchitectonic subdivisions identified here offer a more precise framework for interpreting such LAD effects, allowing clinicians to infer which specific language networks, syntactic, semantic, or action-related, are at risk when lesions approach distinct subdivisions. For example, lesions near areas 44a and 44p may selectively disrupt syntactic sequencing and speech production, whereas involvement of areas 45a may primarily affect semantic integration. Lesions extending into ventral premotor area 6r1 may further compromise motor-planning and action-related aspects of language.

Building on the more fine-grained parcellation of Broca's region into areas 44p, 44a, 45p, and 45a, as well as area 6r1 as part of the premotor cortex (Ruland et al., 2025), we have performed the MACM analysis and assigned the co-activation clusters to the Julich-Brain Atlas (Supplementary material Tab. 1-21). Posterior areas (44p, 45p) displayed bilateral co-activation, whereas anterior areas (44a, 45a) were predominantly left-lateralised, co-activating fronto-parietal, thalamic, and posterior superior temporal regions, including the posterior superior temporal gyrus (pSTG), a core component of the classical fronto-temporal (IFG-pTC) language system, supporting syntactic and semantic processing (Kroczek et al., 2019; van der Burght et al., 2023). This approach allowed us to delineate both shared and area-specific functional networks, highlighting the dorsal versus ventral stream contributions, thalamic involvement, and hemispheric differences in language processing. Left areas 6r1 and 44p showed co-activation within IFG, Intraparietal sulcus (IPS), temporoparietal junction (TPJ) and thalamic nuclei, forming a dorsal IFG-IPS-TPJ-thalamic network. Area 6r1 uniquely co-activated with dorsal premotor (6d3), fusiform, ventral occipital, and linguistic areas, suggesting a role in action-perception mapping and motor planning. In contrast, area 44p left displayed expanded co-activation in posterior IPS and an extensive set of thalamic nuclei (VLA, VA, VAmc, VLA, AV, Am, CL), consistent with dorsal-stream syntactic sequencing and sensorimotor integration. These results align with previous

observations that dominant thalamic lesions produce lexical-semantic errors and selective deficits in word retrieval, while sparing repetition and highly constrained language tasks (Raymer et al., 1997). Left areas 44p and 44a shared IFG, IPS, TPJ, and thalamic activations, forming a dorsal IFG-IPS-TPJ-thalamic network. Separately, area 44p recruited posterior parietal and broad thalamic networks, whereas area 44a engaged fronto-opercular and somatosensory-insular areas with minimal thalamic co-activation. This dorsal-ventral dissociation supports the dual-stream model of language (Friederici, 2011, 2017b), with area 44p contributing to dorsal auditory-motor mapping and area 44a to ventral semantic integration. Bulut and Hagoort (2024) further emphasised that left thalamic nuclei, particularly VA and VLP. Play a central role in coordinating these dorsal and ventral language streams, consistent with our MACM findings. Left areas 45p and 45a exhibited a dorsal-to-ventral network involvement. Both co-activated posterior IPS, SPL, and VLP thalamus, reflecting shared domain-general integrative processes. Area 45p left was predominantly posterior-parietal, whereas area 45a recruited areas ifs, and ifj, premotor areas (6v2 and 6v3), frontal operculum (Op9), and insula, consistent with higher-order cognitive-linguistic control, articulatory planning, and multimodal integration. Building on the hierarchical cluster analyses across both hemispheres revealed two primary clusters within Broca's region: a posterior cluster (44p, 45p) with closer cytoarchitectonic similarity to premotor area 6r1 and IFG2, and the anterior cluster (44a, 45a), more closely linked to IFG1 and dorsolateral cortex (MFG5). Frontal operculum areas formed a separate cluster, confirming their cytoarchitectonic distinction. Multidimensional scaling (MDS) further supported these patterns, showing that posterior areas cluster together with area 6r1, while anterior areas align with anterior IFG and dorsolateral frontal regions. Right-hemispheric homologues mirrored this overall organisation, but with subtle shifts toward subcortical, limbic, and visual territories, indicating hemispheric asymmetries consistent with the left hemisphere's dominance for core language processing. MACM analyses provided functional confirmation of these structural patterns. Pairwise comparisons in the left hemisphere revealed that areas 44p-45p co-activated a shared frontal-insular-precentral network, with area 44p uniquely recruiting dorsal premotor, parietal, and mesial frontal regions, whereas area 45p selectively engaged limbic and medial temporal areas. Similarly, 44a-45a co-activated fronto-temporo-parietal regions, but area 44a showed additional dorsal IPS and thalamic connectivity, whereas area 45a exhibited limited ventral occipital involvement. Right-hemispheric homologues exhibited analogous patterns but generally weaker, with area 44p recruiting thalamic and dorsal subcortical regions, area 45p coupling to ventral occipitotemporal cortex, and area 44a showing strong limbic connectivity, and area 45a remaining largely restricted to the frontal cortex. In conclusion, areas 44p, 45, and 6r1 are primarily involved in dorsal stream functions, such as integrating sensory and motor information, sequencing syntax, and supporting action-related aspects of language. In contrast, the areas 44a and 45a are more engaged in ventral-stream processes, including semantic integration and control within the fronto-opercular network (Friederici, 2011, 2017b). Also, the observed co-activation of thalamic nuclei with areas 44p and 44a underscores the critical role of cortico-thalamo-cortical circuits in coordinating these distributed language networks, in line with Crosson's model of recurrent thalamo-cortical circuits (Crosson, 2021).

By integrating maximum probability cytoarchitectonic maps with task-evoked electrocorticography data, the present study provides converging evidence that speech-related neural activity is predominantly localised outside Broca's areas. Both articulatory and sequence complexity effects were largely observed in premotor cortex, with only limited overlap within Broca's region. This overlap was confined mainly to the ventral portion of area 44a, with a smaller contribution from area 44p, and was evident for only sequence complexity, suggesting a selective and limited role of Broca's region areas in speech sequencing rather than in articulatory execution. Importantly, this spatial dissociation does not imply a reduced role of Broca's region in language. Instead, it supports the interpretation that it constitutes a core linguistic processing region that is not driven by speech articulation itself, but rather

contributes to higher linguistic and cognitive processes. Friederici et at. (2006) demonstrated that the core region, area 44, is modulated by the linguistic complexity of well-formed sentences, whereas neighbouring frontal operculum responds to syntactic violations rather than articulatory demands. Complementing this view, direct cortical recordings by Flinker et al. (2015) demonstrated that Broca's region mediates information transfer between posterior temporal language regions and motor cortex, yet is not robustly engaged during articulation itself. Consistent with these observations, Liu et al. (2025) demonstrated that during the pre-speech phase, electrodes exhibiting high-gamma activity (HGA) related to both sequence and articulatory complexity were predominantly located in the middle precentral gyrus (mPrCG) and surrounding premotor regions. Visual inspection of these electrode clusters onto the receptoarchitectonic maps of Ruland et al. (2025) suggests that they may correspond to ventral premotor areas 6v2 and 6v3, though precise anatomical assignment requires formal registration. A more comprehensive mapping approach, in which all individual electrode activations are quantitatively assigned to Julich-Brain Atlas MPMs, would enable systematic localisation of sequence- and articulatory-related effects across participants. Such an analysis could provide fine-grained, cross-subject comparisons, linking functional ECoG signals directly to cytoarchitectonically defined cortical areas and reducing ambiguity from visual inspection. This would allow more precise identification of the premotor subregions supporting speech preparation and sequencing.

5. Outlook

This work demonstrates that Broca's region is cytoarchitectonically heterogeneous, with distinct areas 44p, 44a, 45p, and 45a showing systematic differences in hemispheric lateralisation, functional specialisation, and connectivity. The probabilistic maps generated during this work provide a precise anatomical framework for future neuroimaging and electrophysiological studies, enabling detailed mapping of individual differences in language, motor, and cognitive processes. Future research can integrate these maps with the task-evoked ECoG and MEG, as well as fMRI and other neuroimaging techniques, to directly link cytoarchitectonic brain structure with high-resolution functional dynamics, such as speech production, sequence complexity, and articulatory control. Longitudinal and developmental studies could leverage these maps to investigate how structural heterogeneity and functional specialisation emerge across the lifespan, and how variability relates to language acquisition or recovery after brain injury. At the network level, combining cytoarchitectonic maps with connectivity analyses will allow exploration of how each area within Broca's region contributes to domain-specific and domain-general networks, and how these networks interact during complex cognitive and motor tasks. Clinically, the refined parcellations could guide neurosurgical planning, non-invasive brain stimulation, and individualised neurorehabilitation by providing more precise targets informed by both structural and functional heterogeneity. In summary, these findings offer a framework for linking microstructural variation with functional differentiation, supporting next-generation, multimodal brain atlases that capture the interplay between architecture, connectivity, and cognition across health and disease.

6. Reference List/Bibliography

Amelink, J. S., Postema, M. C., Kong, X.-Z., Schijven, D., Carrión-Castillo, A., Soheili-Nezhad, S., Sha, Z., Molz, B., Joliot, M., Fisher, S. E., & Francks, C. (2024). Imaging genetics of language network functional connectivity reveals links with language-related abilities, dyslexia and handedness. *Communications Biology*, *7*(1), 1209. https://doi.org/10.1038/s42003-024-06890-3

Amunts, K., Armstrong, E., Malikovic, A., Hömke, L., Mohlberg, H., Schleicher, A., & Zilles, K. (2007). Gender-specific left-right asymmetries in human visual cortex. *J Neurosci*, *27*(6), 1356-1364. https://doi.org/10.1523/jneurosci.4753-06.2007

Amunts, K., Axer, M., Banerjee, S., Bitsch, L., Bjaalie, J. G., Brauner, P., Brovelli, A., Calarco, N., Carrere, M., Caspers, S., Charvet, C. J., Cichon, S., Cools, R., Costantini, I., D'Angelo, E. U., De Bonis, G., Deco, G., DeFelipe, J., Destexhe, A., . . . Zaborszky, L. (2024). The coming decade of digital brain research: A vision for neuroscience at the intersection of technology and computing. *Imaging Neurosci (Camb)*, *2*. https://doi.org/10.1162/imag_a_00137

Amunts, K., DeFelipe, J., Pennartz, C., Destexhe, A., Migliore, M., Ryvlin, P., Furber, S., Knoll, A., Bitsch, L., Bjaalie, J. G., Ioannidis, Y., Lippert, T., Sanchez-Vives, M. V., Goebel, R., & Jirsa, V. (2022). Linking Brain Structure, Activity, and Cognitive Function through Computation. *eNeuro*, *9*(2). https://doi.org/10.1523/eneuro.0316-21.2022

Amunts, K., Kedo, O., Kindler, M., Pieperhoff, P., Mohlberg, H., Shah, N. J., Habel, U., Schneider, F., & Zilles, K. (2005). Cytoarchitectonic mapping of the human amygdala, hippocampal region and entorhinal cortex: intersubject variability and probability maps. *Anat Embryol (Berl)*, *210*(5-6), 343-352. https://doi.org/10.1007/s00429-005-0025-5

Amunts, K., Lenzen, M., Friederici, A. D., Schleicher, A., Morosan, P., Palomero-Gallagher, N., & Zilles, K. (2010). Broca's Region: Novel Organizational Principles and Multiple Receptor Mapping. *PLOS Biology*, *8*(9), e1000489. https://doi.org/10.1371/journal.pbio.1000489

Amunts, K., Lepage, C., Borgeat, L., Mohlberg, H., Dickscheid, T., Rousseau, M., Bludau, S., Bazin, P. L., Lewis, L. B., Oros-Peusquens, A. M., Shah, N. J., Lippert, T., Zilles, K., & Evans, A. C. (2013). BigBrain: an ultrahigh-resolution 3D human brain model. *Science*, *340*(6139), 1472-1475. https://doi.org/10.1126/science.1235381

Amunts, K., Mohlberg, H., Bludau, S., & Zilles, K. (2020). Julich-Brain: A 3D probabilistic atlas of the human brain's cytoarchitecture. *Science*, *369*(6506), 988-992. https://doi.org/10.1126/science.abb4588

Amunts, K., Schleicher, A., Bürgel, U., Mohlberg, H., Uylings, H. B. M., & Zilles, K. (1999). Broca's region revisited: Cytoarchitecture and intersubject variability. *Journal of Comparative Neurology*, *412*(2), 319-341. https://doi.org/https://doi.org/10.1002/(SICI)1096-9861(19990920)412:2<319::AID-CNE10>3.0.CO;2-7

Amunts, K., Schleicher, A., Ditterich, A., & Zilles, K. (2003). Broca's region: Cytoarchitectonic asymmetry and developmental changes [Article]. *Journal of Comparative Neurology*, *465*(1), 72-89. https://doi.org/10.1002/cne.10829

Amunts, K., & Zilles, K. (2012). Architecture and organizational principles of Broca's region. *Trends in Cognitive Sciences*, *16*(8), 418-426. https://doi.org/https://doi.org/10.1016/j.tics.2012.06.005

Bacher, J., Pöge, A., & Wenzig, K. (2010). Oldenbourg Wissenschaftsverlag. https://doi.org/doi:10.1524/9783486710236

Bernal, B., & Ardila, A. (2009). The role of the arcuate fasciculus in conduction aphasia. *Brain*, *132*(9), 2309-2316. https://doi.org/10.1093/brain/awp206

Bizzi, A., Nava, S., Ferrè, F., Castelli, G., Aquino, D., Ciaraffa, F., Broggi, G., DiMeco, F., & Piacentini, S. (2012). Aphasia induced by gliomas growing in the ventrolateral frontal region: assessment with diffusion MR tractography, functional MR imaging and neuropsychology. *Cortex*, *48*(2), 255-272. https://doi.org/10.1016/j.cortex.2011.11.015

Bludau, S., Eickhoff, S. B., Mohlberg, H., Caspers, S., Laird, A. R., Fox, P. T., Schleicher, A., Zilles, K., & Amunts, K. (2014). Cytoarchitecture, probability maps and functions of the human frontal pole. *Neuroimage*, *93 Pt 2*(Pt 2), 260-275. https://doi.org/10.1016/j.neuroimage.2013.05.052

Bohland, J. W., Bokil, H., Allen, C. B., & Mitra, P. P. (2009). The brain atlas concordance problem: quantitative comparison of anatomical parcellations. *PLoS One*, *4*(9), e7200. https://doi.org/10.1371/journal.pone.0007200

Botvinik-Nezer, R., Holzmeister, F., Camerer, C. F., Dreber, A., Huber, J., Johannesson, M., Kirchler, M., Iwanir, R., Mumford, J. A., Adcock, R. A., Avesani, P., Baczkowski, B. M., Bajracharya, A., Bakst, L., Ball, S., Barilari, M., Bault, N., Beaton, D., Beitner, J., . . . Schonberg, T. (2020). Variability in the analysis of a single neuroimaging dataset by many teams. *Nature*, *582*(7810), 84-88. https://doi.org/10.1038/s41586-020-2314-9

Brandstetter, A., Bolakhrif, N., Schiffer, C., Dickscheid, T., Mohlberg, H., & Amunts, K. (2021, 2021//). Deep Learning-Supported Cytoarchitectonic Mapping of the Human Lateral Geniculate Body in the BigBrain. Brain-Inspired Computing, Cham.

Broca, P. (1861). Nouvelle observation d'aphémie produite par une lésion de la moitié postérieure des deuxième et troisième circonvolutions frontales. *Bulletins de la Société anatomique de Paris*, *36*, 398-407.

Brodmann, K. (1909). *Vergleichende Lokalisationslehre der Grosshirnrinde in ihren Prinzipien dargestellt auf Grund des Zellenbaues*. Barth.

Bruno, A., Lothmann, K., Bludau, S., Mohlberg, H., & Amunts, K. (2024). New organizational principles and 3D cytoarchitectonic maps of the dorsolateral prefrontal cortex in the human brain. *Front Neuroimaging*, *3*, 1339244. https://doi.org/10.3389/fnimg.2024.1339244

Bulut, T. (2022). Meta-analytic connectivity modeling of the left and right inferior frontal gyri. *Cortex*, *155*, 107-131. https://doi.org/https://doi.org/10.1016/j.cortex.2022.07.003

Bulut, T. (2023). Domain-general and domain-specific functional networks of Broca's area underlying language processing. *Brain Behav*, *13*(7), e3046. https://doi.org/10.1002/brb3.3046

Bulut, T., & Hagoort, P. (2024). Contributions of the left and right thalami to language: A meta-analytic approach. *Brain Structure and Function*, *229*(9), 2149-2166. https://doi.org/10.1007/s00429-024-02795-3

Casamitjana, A., Mancini, M., Robinson, E., Peter, L., Annunziata, R., Althonayan, J., Crampsie, S., Blackburn, E., Billot, B., Atzeni, A., Puonti, O., Balbastre, Y., Schmidt, P., Hughes, J., Augustinack, J. C., Edlow, B. L., Zöllei, L., Thomas, D. L., Kliemann, D., . . . Iglesias, J. E. (2025). A probabilistic histological atlas of the human brain for MRI segmentation. *Nature*. https://doi.org/10.1038/s41586-025-09708-2

Castleman, K. R. (1979). *Digital Image Processing*. Prentice Hall Professional Technical Reference.

Clos, M., Amunts, K., Laird, A. R., Fox, P. T., & Eickhoff, S. B. (2013). Tackling the multifunctional nature of Broca's region meta-analytically: Co-activation-based parcellation of area 44. *Neuroimage*, *83*, 174-188. https://doi.org/https://doi.org/10.1016/j.neuroimage.2013.06.041

Crosson, B. (2021). The Role of Cortico-Thalamo-Cortical Circuits in Language: Recurrent Circuits Revisited. *Neuropsychol Rev*, *31*(3), 516-533. https://doi.org/10.1007/s11065-019-09421-8

Dickscheid, T., Gui, X., Simsek, A., Schiffer, C., Mangin, J.-F., Leprince, Y., Jirsa, V., Bjaalie, J. G., Leergaard, T. B., Bludau, S., & Amunts, K. (2025). Siibra: A software tool suite for realizing a Multilevel Human Brain Atlas from complex data resources. *bioRxiv*, 2025.2005.2020.655042. https://doi.org/10.1101/2025.05.20.655042

Diveica, V., Riedel, M. C., Salo, T., Laird, A. R., Jackson, R. L., & Binney, R. J. (2023). Graded functional organization in the left inferior frontal gyrus: evidence from task-free and task-based functional connectivity. *Cerebral Cortex*, *33*(23), 11384-11399. https://doi.org/10.1093/cercor/bhad373

Eichner, C., Berger, P., Klein, C. C., & Friederici, A. D. (2024). Lateralization of dorsal fiber tract targeting Broca's area concurs with language skills during development. *Progress in Neurobiology*, *236*, 102602. https://doi.org/https://doi.org/10.1016/j.pneurobio.2024.102602

Eickhoff, S. B., Bzdok, D., Laird, A. R., Kurth, F., & Fox, P. T. (2012). Activation likelihood estimation meta-analysis revisited. *Neuroimage*, *59*(3), 2349-2361. https://doi.org/10.1016/j.neuroimage.2011.09.017

Eickhoff, S. B., Jbabdi, S., Caspers, S., Laird, A. R., Fox, P. T., Zilles, K., & Behrens, T. E. (2010). Anatomical and functional connectivity of cytoarchitectonic areas within the human parietal operculum. *J Neurosci*, *30*(18), 6409-6421. https://doi.org/10.1523/jneurosci.5664-09.2010

Eickhoff, S. B., Laird, A. R., Grefkes, C., Wang, L. E., Zilles, K., & Fox, P. T. (2009). Coordinate-based activation likelihood estimation meta-analysis of neuroimaging data: A random-effects approach based on empirical estimates of spatial uncertainty. *Human Brain Mapping*, *30*(9), 2907-2926. https://doi.org/https://doi.org/10.1002/hbm.20718

Eickhoff, S. B., Stephan, K. E., Mohlberg, H., Grefkes, C., Fink, G. R., Amunts, K., & Zilles, K. (2005). A new SPM toolbox for combining probabilistic cytoarchitectonic maps and functional imaging data. *Neuroimage*, *25*(4), 1325-1335. https://doi.org/https://doi.org/10.1016/j.neuroimage.2004.12.034

Evans, A. C., Janke, A. L., Collins, D. L., & Baillet, S. (2012). Brain templates and atlases. *Neuroimage*, *62*(2), 911-922. https://doi.org/https://doi.org/10.1016/j.neuroimage.2012.01.024

Fabbri-Destro, M., & Rizzolatti, G. (2008). Mirror Neurons and Mirror Systems in Monkeys and Humans. *Physiology*, *23*(3), 171-179. https://doi.org/10.1152/physiol.00004.2008

Fan, L., Li, H., Zhuo, J., Zhang, Y., Wang, J., Chen, L., Yang, Z., Chu, C., Xie, S., Laird, A. R., Fox, P. T., Eickhoff, S. B., Yu, C., & Jiang, T.

(2016). The Human Brainnetome Atlas: A New Brain Atlas Based on Connectional Architecture. *Cereb Cortex*, *26*(8), 3508-3526. https://doi.org/10.1093/cercor/bhw157

Fedorenko, E., Duncan, J., & Kanwisher, N. (2012). Language-Selective and Domain-General Regions Lie Side by Side within Broca's Area. *Current Biology*, *22*(21), 2059-2062. https://doi.org/https://doi.org/10.1016/j.cub.2012.09.011

Flinker, A., Korzeniewska, A., Shestyuk, A. Y., Franaszczuk, P. J., Dronkers, N. F., Knight, R. T., & Crone, N. E. (2015). Redefining the role of Broca's area in speech. *Proc Natl Acad Sci U S A*, *112*(9), 2871-2875. https://doi.org/10.1073/pnas.1414491112

Friederici, A. D. (2011). The Brain Basis of Language Processing: From Structure to Function. *Physiological Reviews*, *91*(4), 1357-1392. https://doi.org/10.1152/physrev.00006.2011

Friederici, A. D. (2017a). Evolution of the neural language network. *Psychonomic Bulletin & Review*, *24*(1), 41-47. https://doi.org/10.3758/s13423-016-1090-x

Friederici, A. D. (2017b). *Language in Our Brain: The Origins of a Uniquely Human Capacity*. The MIT Press. https://doi.org/10.7551/mitpress/11173.001.0001

Friederici, A. D., Fiebach, C. J., Schlesewsky, M., Bornkessel, I. D., & von Cramon, D. Y. (2006). Processing Linguistic Complexity and Grammaticality in the Left Frontal Cortex. *Cerebral Cortex*, *16*(12), 1709-1717. https://doi.org/10.1093/cercor/bhj106

Friston, K. J. (1994). Functional and effective connectivity in neuroimaging: A synthesis. *Human Brain Mapping*, *2*(1-2), 56-78. https://doi.org/https://doi.org/10.1002/hbm.460020107

Gallardo, G., Eichner, C., Sherwood, C. C., Hopkins, W. D., Anwander, A., & Friederici, A. D. (2023). Morphological evolution of language-relevant brain areas. *PLOS Biology*, *21*(9), e3002266. https://doi.org/10.1371/journal.pbio.3002266

Glasser, M. F., Coalson, T. S., Robinson, E. C., Hacker, C. D., Harwell, J., Yacoub, E., Ugurbil, K., Andersson, J., Beckmann, C. F., & Jenkinson, M. (2016). A multi-modal parcellation of human cerebral cortex. *Nature*, *536*(7615), 171-178.

Goucha, T., & Friederici, A. D. (2015). The language skeleton after dissecting meaning: A functional segregation within Broca's Area. *Neuroimage*, *114*, 294-302. https://doi.org/10.1016/j.neuroimage.2015.04.011

Goucha, T., Zaccarella, E., & Friederici, A. D. (2017). A revival of Homo loquens as a builder of labeled structures: Neurocognitive considerations. *Neuroscience & Biobehavioral Reviews*, *81*, 213-224. https://doi.org/https://doi.org/10.1016/j.neubiorev.2017.01.036

Grodzinsky, Y., & Friederici, A. D. (2006). Neuroimaging of syntax and syntactic processing. *Current Opinion in Neurobiology*, *16*(2), 240-246. https://doi.org/https://doi.org/10.1016/j.conb.2006.03.007

Hagoort, P. (2005). On Broca, brain, and binding: a new framework. *Trends in Cognitive Sciences*, *9*(9), 416-423. https://doi.org/https://doi.org/10.1016/j.tics.2005.07.004

Hagoort, P., & Indefrey, P. (2014). The neurobiology of language beyond single words. *Annu Rev Neurosci*, *37*, 347-362. https://doi.org/10.1146/annurev-neuro-071013-013847

Hickok, G. (2013). The role of Broca's area in language function. In C. Boeckx & K. K. Grohmann (Eds.), *The Cambridge Handbook of Biolinguistics* (pp. 341-349). Cambridge University Press. https://doi.org/DOI: 10.1017/CBO9780511980435.020

Hickok, G., Venezia, J., & Teghipco, A. (2022). Beyond Broca: neural architecture and evolution of a dual motor speech coordination system. *Brain*, *146*(5), 1775-1790. https://doi.org/10.1093/brain/awac454

Huson, D. H., & Bryant, D. (2006). Application of phylogenetic networks in evolutionary studies. *Mol Biol Evol*, *23*(2), 254-267. https://doi.org/10.1093/molbev/msj030

Jones, S. E., Buchbinder, B. R., & Aharon, I. (2000). Three-dimensional mapping of cortical thickness using Laplace's equation. *Hum Brain Mapp*, *11*(1), 12-32. https://doi.org/10.1002/1097-0193(200009)11:1<12::aid-hbm20>3.0.co;2-k

Keller, S. S., Roberts, N., & Hopkins, W. (2009). A comparative magnetic resonance imaging study of the anatomy, variability, and asymmetry of Broca's area in the human and chimpanzee brain. *J Neurosci*, *29*(46), 14607-14616. https://doi.org/10.1523/jneurosci.2892-09.2009

Kiwitz, K., Brandstetter, A., Schiffer, C., Bludau, S., Mohlberg, H., Omidyeganeh, M., Massicotte, P., & Amunts, K. (2022). Cytoarchitectonic Maps of the Human Metathalamus in 3D Space [Original Research]. *Frontiers in Neuroanatomy*, *Volume 16 - 2022*. https://doi.org/10.3389/fnana.2022.837485

Kiwitz, K., Schiffer, C., Spitzer, H., Dickscheid, T., & Amunts, K. (2020). Deep learning networks reflect cytoarchitectonic features used in brain mapping. *Scientific Reports*, *10*(1), 22039.

Krause, D., & Thörnig, P. (2018). JURECA: Modular supercomputer at Jülich Supercomputing Centre. *Journal of large-scale research facilities JLSRF*, *4*. https://doi.org/10.17815/jlsrf-4-121-1

Kroczek, L. O. H., Gunter, T. C., Rysop, A. U., Friederici, A. D., & Hartwigsen, G. (2019). Contributions of left frontal and temporal cortex to sentence comprehension: Evidence from simultaneous TMS-EEG. *Cortex*, *115*, 86-98. https://doi.org/https://doi.org/10.1016/j.cortex.2019.01.010

Liu, J. R., Zhao, L., Hullett, P. W., & Chang, E. F. (2025). Speech sequencing in the human precentral gyrus. *Nature Human Behaviour*, *9*(11), 2327-2344. https://doi.org/10.1038/s41562-025-02250-1

Liu, Y., Gao, C., Wang, P., Friederici, A. D., Zaccarella, E., & Chen, L. (2023). Exploring the neurobiology of Merge at a basic level: insights from a novel artificial grammar paradigm [Original Research]. *Frontiers in Psychology*, *Volume 14 - 2023*. https://doi.org/10.3389/fpsyg.2023.1151518

Luppi, A. I., Gellersen, H. M., Liu, Z.-Q., Peattie, A. R. D., Manktelow, A. E., Adapa, R., Owen, A. M., Naci, L., Menon, D. K., Dimitriadis, S. I., & Stamatakis, E. A. (2024). Systematic evaluation of fMRI data-processing pipelines for consistent functional connectomics. *Nature Communications*, *15*(1), 4745. https://doi.org/10.1038/s41467-024-48781-5

Mahalanobis, P., Majumdar, D., & Rao, C. (1949). Anthropometric survey of the United Provinces, 1941: a statistical study. *Sankhya. The Indian Journal of Statistics*, *9*, 89–324.

Mandonnet, E., & Duffau, H. (2021). Broca's area: why was neurosurgery neglected for so long when seeking to re-establish the scientific truth? *Brain*, *144*(7), e60-e60. https://doi.org/10.1093/brain/awab195

Merker, B. (1983). Silver staining of cell bodies by means of physical development. *J Neurosci Methods*, *9*(3), 235-241. https://doi.org/10.1016/0165-0270(83)90086-9

Mueller, S., Wang, D., Fox, M. D., Yeo, B. T., Sepulcre, J., Sabuncu, M. R., Shafee, R., Lu, J., & Liu, H. (2013). Individual variability in functional connectivity architecture of the human brain. *Neuron*, *77*(3), 586-595.

Nakae, T., Matsumoto, R., Kunieda, T., Arakawa, Y., Kobayashi, K., Shimotake, A., Yamao, Y., Kikuchi, T., Aso, T., Matsuhashi, M., Yoshida, K., Ikeda, A., Takahashi, R., Lambon Ralph, M. A., & Miyamoto, S. (2020). Connectivity Gradient in the Human Left Inferior Frontal Gyrus: Intraoperative Cortico-Cortical Evoked Potential Study. *Cerebral Cortex*, *30*(8), 4633-4650. https://doi.org/10.1093/cercor/bhaa065

Omidyeganeh, M., Lepage, C., Wagstyl, K., Spitzer, H., Dickscheid, T., Amunts, K., & Evans, A. (2020). Non-linear registration of 1µm Histology Sections into 3D 20µm BigBrain Space. 26th Annual Meeting of the Organization for Human Brain Mapping,

Ono, M., Kubik, S., & Abernathey, C. D. (1990). *Atlas of the Cerebral Sulci*. G. Thieme Verlag. https://books.google.de/books?id=-MakzgEACAAJ

Papitto, G., Friederici, A. D., & Zaccarella, E. (2024). Distinct neural mechanisms for action access and execution in the human brain: insights from an fMRI study. *Cerebral Cortex*, *34*(4). https://doi.org/10.1093/cercor/bhae163

Pas, K. E., Saleem, K. S., Basser, P. J., & Avram, A. V. (2024). Direct segmentation of cortical cytoarchitectonic domains using ultra-high-resolution whole-brain diffusion MRI. *Imaging Neuroscience*, *2*. https://doi.org/10.1162/imag_a_00393

Petrides, M., & Pandya, D. N. (2002). Comparative cytoarchitectonic analysis of the human and the macaque ventrolateral prefrontal cortex and corticocortical connection patterns in the monkey. *European Journal of Neuroscience*, *16*(2), 291-310. https://doi.org/https://doi.org/10.1046/j.1460-9568.2001.02090.x

Petrides, M., & Pandya, D. N. (2012). Chapter 26 - The Frontal Cortex. In J. K. Mai & G. Paxinos (Eds.), *The Human Nervous System (Third Edition)* (pp. 988-1011). Academic Press. https://doi.org/https://doi.org/10.1016/B978-0-12-374236-0.10026-4

Raymer, A. M., Moberg, P., Crosson, B., Nadeau, S., & Rothi, L. J. (1997). Lexical-semantic deficits in two patients with dominant thalamic infarction. *Neuropsychologia*, *35*(2), 211-219. https://doi.org/10.1016/s0028-3932(96)00069-3

Riley, S. P., Chu, D. Y., Nair, V. A., Baskaya, M. K., Kuo, J. S., Meyerand, M. E., & Prabhakaran, V. (2022). Characterizing the relationship between lesion-activation distance using fMRI and verbal measures in brain tumor patients. *Interdiscip Neurosurg*, *27*. https://doi.org/10.1016/j.inat.2021.101391

Robinson, J. L., Laird, A. R., Glahn, D. C., Lovallo, W. R., & Fox, P. T. (2010). Metaanalytic connectivity modeling: delineating the functional connectivity of the human amygdala. *Hum Brain Mapp*, *31*(2), 173-184. https://doi.org/10.1002/hbm.20854

Rodd, J. M., Vitello, S., Woollams, A. M., & Adank, P. (2015). Localising semantic and syntactic processing in spoken and written language comprehension: An Activation Likelihood Estimation meta-analysis. *Brain and Language*, *141*, 89-102. https://doi.org/https://doi.org/10.1016/j.bandl.2014.11.012

Rolls, E. T., Huang, C. C., Lin, C. P., Feng, J., & Joliot, M. (2020). Automated anatomical labelling atlas 3. *Neuroimage*, *206*, 116189. https://doi.org/10.1016/j.neuroimage.2019.116189

Rosen, H. J., Petersen, S. E., Linenweber, M. R., Snyder, A. Z., White, D. A., Chapman, L., Dromerick, A. W., Fiez, J. A., Corbetta, & M. (2000). Neural correlates of recovery from aphasia after damage

to left inferior frontal cortex. *Neurology*, *55*(12), 1883-1894. https://doi.org/doi:10.1212/WNL.55.12.1883

Ruland, S. H., Palomero-Gallagher, N., Hoffstaedter, F., Eickhoff, S. B., Mohlberg, H., & Amunts, K. (2022). The inferior frontal sulcus: Cortical segregation, molecular architecture and function. *Cortex*, *153*, 235-256. https://doi.org/https://doi.org/10.1016/j.cortex.2022.03.019

Ruland, S. H., Sigl, B., Stangier, J., Caspers, S., Bludau, S., Mohlberg, H., Pieperhoff, P., & Amunts, K. (2025). Revised cytoarchitectonic mapping of the human premotor cortex identifies seven areas and refines the localisation of frontal eye fields. *Communications Biology*, *8*(1), 1143. https://doi.org/10.1038/s42003-025-08528-4

Rutten, G.-J. (2017). *The Broca-Wernicke Doctrine. A Historical and Clinical Perspective on Localization of Language Functions*. https://doi.org/10.1007/978-3-319-54633-9

Saal, M. (2019). *Two new areas in the human frontal operculum: cytoarchitecture, stereotaxic maps and brain function* (Publication Number FZJ-2020-04318) [Dissertation / PhD Thesis, HHU Düsseldorf]. https://juser.fz-juelich.de/record/887657

Sacchet, M. D., & Knutson, B. (2013). Spatial smoothing systematically biases the localization of reward-related brain activity. *Neuroimage*, *66*, 270-277. https://doi.org/10.1016/j.neuroimage.2012.10.056

Sarkisov, S., Filimonov, I., Kononova, E., Preobraschenskaja, I., & Kukuev, L. (1955). Atlas of cytoarchitectonics of the human cerebral cortex. Medzig, Moscow. In.

Schiffer, C., et al. (2025). CytoNet: A Foundation Model for the Human Cerebral Cortex. *arXiv*. https://doi.org/https://doi.org/10.48550/ARXIV.2511.01870

Schiffer, C., Spitzer, H., Kiwitz, K., Unger, N., Wagstyl, K., Evans, A. C., Harmeling, S., Amunts, K., & Dickscheid, T. (2021). Convolutional neural networks for cytoarchitectonic brain mapping at large

scale. *Neuroimage*, *240*, 118327. https://doi.org/10.1016/j.neuroimage.2021.118327

Schleicher, A., Amunts, K., Geyer, S., Kowalski, T., Schormann, T., Palomero-Gallagher, N., & Zilles, K. (2000). A stereological approach to human cortical architecture: identification and delineation of cortical areas. *J Chem Neuroanat*, *20*(1), 31-47. https://doi.org/10.1016/s0891-0618(00)00076-4

Schleicher, A., & Zilles, K. (1990). A quantitative approach to cytoarchitectonics: Analysis of structural inhomogeneities in nervous tissue using an image analyser. *Journal of Microscopy*, *157*(3), 367-381. https://doi.org/https://doi.org/10.1111/j.1365-2818.1990.tb02971.x

Shankle, W. R., Rafii, M. S., Landing, B. H., & Fallon, J. H. (1999). Approximate doubling of numbers of neurons in postnatal human cerebral cortex and in 35 specific cytoarchitectural areas from birth to 72 months. *Pediatr Dev Pathol*, *2*(3), 244-259. https://doi.org/10.1007/s100249900120

Tomaiuolo, F., MacDonald, J. D., Caramanos, Z., Posner, G., Chiavaras, M., Evans, A. C., & Petrides, M. (1999). Morphology, morphometry and probability mapping of the pars opercularis of the inferior frontal gyrus: an in vivo MRI analysis. *European Journal of Neuroscience*, *11*(9), 3033-3046. https://doi.org/https://doi.org/10.1046/j.1460-9568.1999.00718.x

Trettenbrein, P. C., & Friederici, A. D. (2025). Chapter 18 - Functional and structural brain asymmetries in language processing. In C. Papagno & P. Corballis (Eds.), *Handbook of Clinical Neurology* (Vol. 208, pp. 269-287). Elsevier. https://doi.org/https://doi.org/10.1016/B978-0-443-15646-5.00020-8

Turkeltaub, P. E., Eickhoff, S. B., Laird, A. R., Fox, M., Wiener, M., & Fox, P. (2012). Minimizing within-experiment and within-group effects in Activation Likelihood Estimation meta-analyses. *Hum Brain Mapp*, *33*(1), 1-13. https://doi.org/10.1002/hbm.21186

Unger, N., Haeck, M., Eickhoff, S. B., Camilleri, J. A., Dickscheid, T., Mohlberg, H., Bludau, S., Caspers, S., & Amunts, K. (2023). Cytoarchitectonic mapping of the human frontal operculum-New correlates for a variety of brain functions. *Front Hum Neurosci*, *17*, 1087026. https://doi.org/10.3389/fnhum.2023.1087026

Uylings, H. B., Jacobsen, A. M., Zilles, K., & Amunts, K. (2006). Left-right asymmetry in volume and number of neurons in adult Broca's area. *Cortex*, *42*(4), 652-658. https://doi.org/10.1016/s0010-9452(08)70401-5

Uylings, H. B. M., Malofeeva, L. I., Bogolepova, I. N., Jacobsen, A. M., Amunts, K., & Zilles, K. (2005). No postnatal doubling of number of neurons in human Broca's areas (Brodmann areas 44 and 45)? A stereological study. *Neuroscience*, *136*(3), 715-728. https://doi.org/https://doi.org/10.1016/j.neuroscience.2005.07.048

van der Burght, C. L., Numssen, O., Schlaak, B., Goucha, T., & Hartwigsen, G. (2023). Differential contributions of inferior frontal gyrus subregions to sentence processing guided by intonation. *Hum Brain Mapp*, *44*(2), 585-598. https://doi.org/10.1002/hbm.26086

von Economo, C. F., & Koskinas, G. N. (1925). *Die cytoarchitektonik der hirnrinde des erwachsenen menschen*. J. Springer.

Wang, Y., Xu, F., Zhou, W., Hou, L., Tang, Y., & Liu, S. (2022). Morphological and hemispheric and sex differences of the anterior ascending ramus and the horizontal ascending ramus of the lateral sulcus. *Brain Struct Funct*, *227*(6), 1949-1961. https://doi.org/10.1007/s00429-022-02482-1

Ward, J. H. (1963). Hierarchical Grouping to Optimize an Objective Function. *Journal of the American Statistical Association*, *58*(301), 236-244. https://doi.org/10.2307/2282967

Wree, A., Schleicher, A., & Zilles, K. (1982). Estimation of volume fractions in nervous tissue with an image analyzer. *J Neurosci Methods*, *6*(1-2), 29-43. https://doi.org/10.1016/0165-0270(82)90014-0

Wu, Y., Liu, J., Yu, G., Jv, R., Wang, Y., & Zang, P. (2022). Association fiber tracts related to Broca's area: A comparative study based on diffusion spectrum imaging and fiber dissection. *Front Neurosci*, *16*, 978912. https://doi.org/10.3389/fnins.2022.978912

Zaccarella, E., & Friederici, A. D. (2015). Merge in the Human Brain: A Sub-Region Based Functional Investigation in the Left Pars Opercularis. *Front Psychol*, *6*, 1818. https://doi.org/10.3389/fpsyg.2015.01818

Zaccarella, E., Papitto, G., & Friederici, A. D. (2021). Language and action in Broca's area: Computational differentiation and cortical segregation. *Brain and Cognition*, *147*, 105651. https://doi.org/https://doi.org/10.1016/j.bandc.2020.105651

Zhang, Y., Fan, L., Caspers, S., Heim, S., Song, M., Liu, C., Mo, Y., Eickhoff, S. B., Amunts, K., & Jiang, T. (2017). Cross-cultural consistency and diversity in intrinsic functional organization of Broca's Region. *Neuroimage*, *150*, 177-190. https://doi.org/https://doi.org/10.1016/j.neuroimage.2017.02.042

Zhang, Z. (2025). *Cytoarchitectonic mapping of five new areas in the anterior lateral prefrontal cortex* [Dissertation, Heinrich Heine Universität Düsseldorf].

Zilles, K., & Amunts, K. (2013). Individual variability is not noise. *Trends Cogn Sci*, *17*(4), 153-155. https://doi.org/10.1016/j.tics.2013.02.003

Zilles, K., Armstrong, E., Schleicher, A., & Kretschmann, H. J. (1988). The human pattern of gyrification in the cerebral cortex. *Anat Embryol (Berl)*, *179*(2), 173-179. https://doi.org/10.1007/bf00304699

7. Supplementary Materials

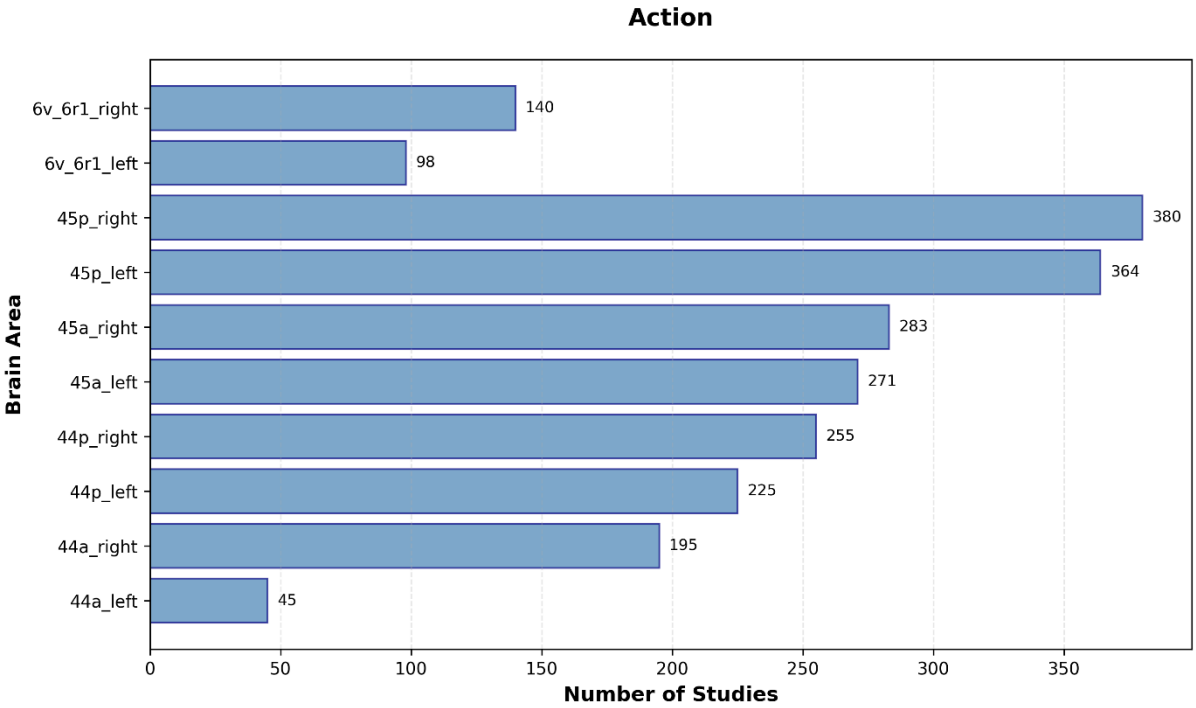

Figure 1 Action – related functional associations across cytoarchitectonic areas. Bar plots (blue-grey) show the number of BrainMap experiments associated with action-related domains for left- and right-hemispheric representations of areas 6r1, 44p, 44a, 45p, and 45a. Across regions, right-hemisphere values are generally higher, most notably in 44a and 6r1, suggesting a modest right-lateralized trend for motor–related functions, whereas areas 45p and 45a show nearly symmetrical distributions.

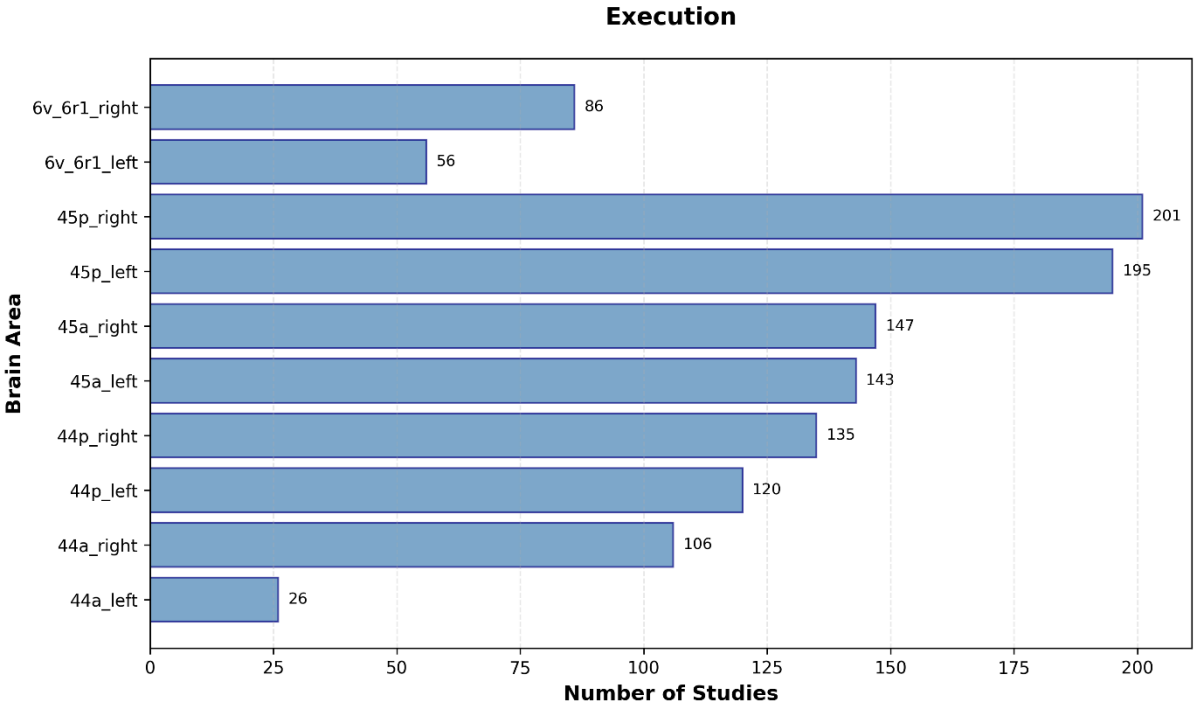

Figure 2 Motor execution-related associations across cytoarchitectonic areas. The figure illustrates the number of experiments associated with motor execution tasks. Most areas show close bilateral balance, though right 6r1 and right 44a display somewhat higher counts, consistent with right-hemispheric contributions to motor coordination and execution monitoring.

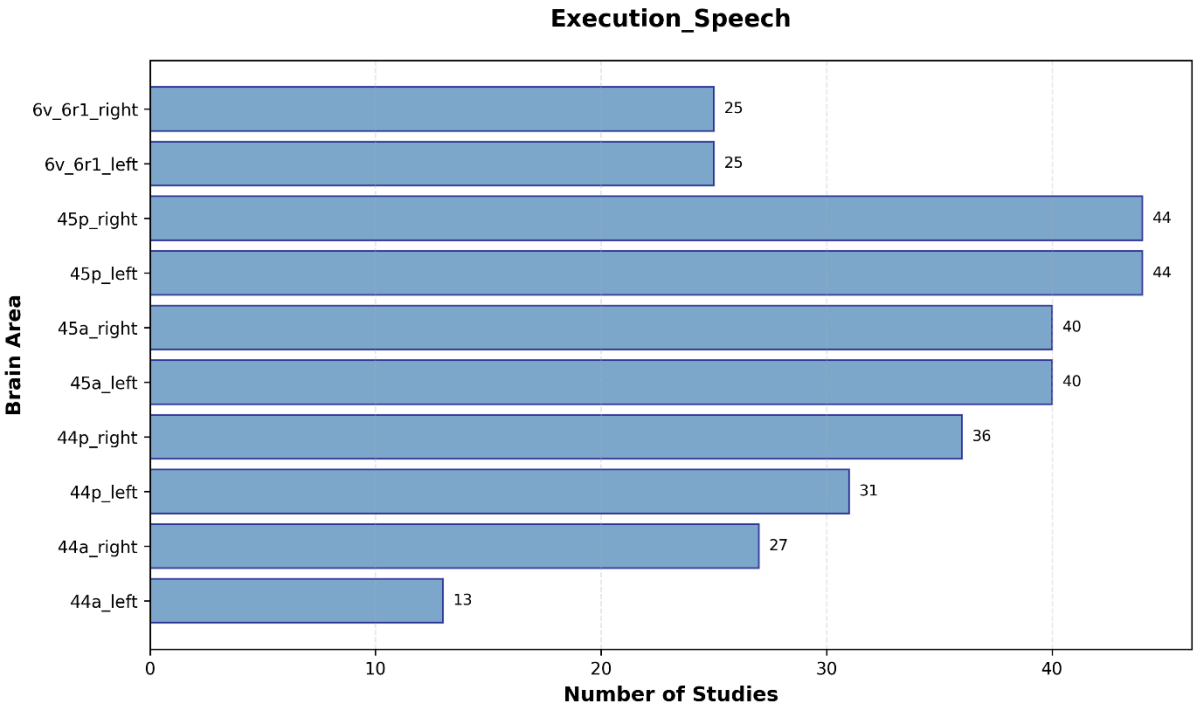

Figure 3 Speech execution – related associations across cytoarchitectonic areas. The plot shows the distribution of experiments involving speech execution tasks. All regions exhibit bilateral involvement with near-identical left-right counts, confirming that speech production engages both hemispheric homologues within inferior frontal and premotor cortices.

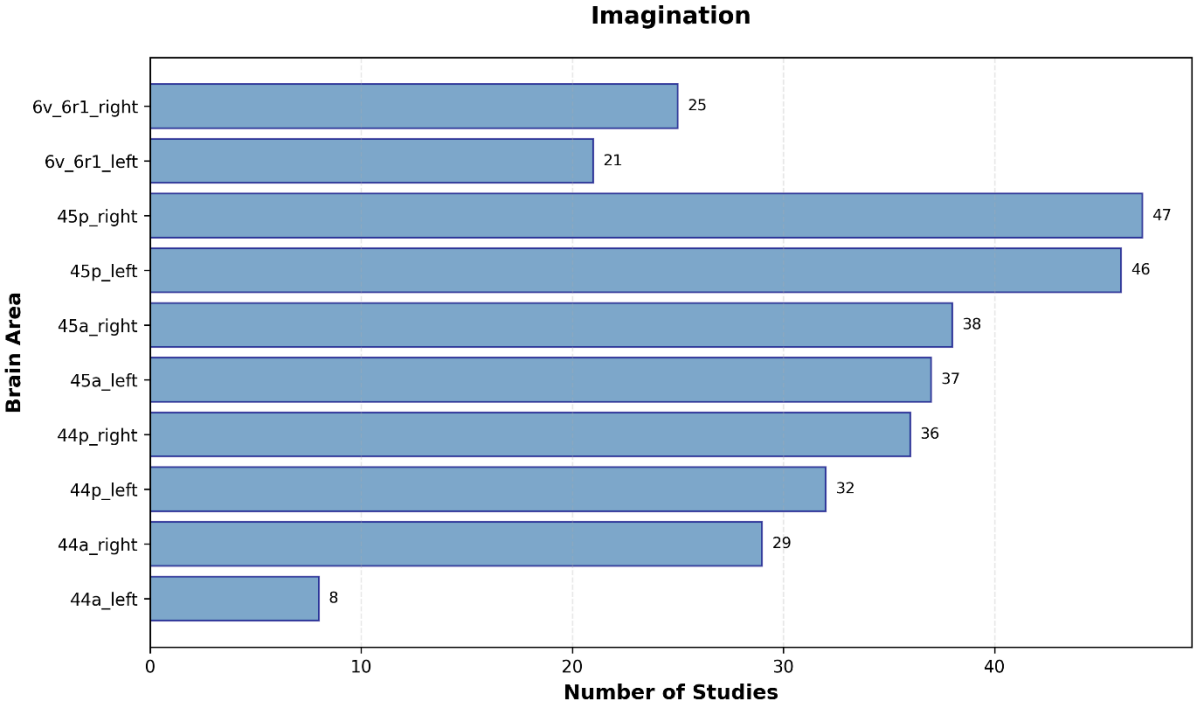

Figure 4 Motor imagination – related associations across cytoarchitectonic areas. Bars indicate the number of experiments related to motor or action imagination. Right-hemispheric representations, particularly in 44a and 6r1, are slightly more prominent, supporting the role of right premotor and inferior frontal regions in imagery and simulation of movement.

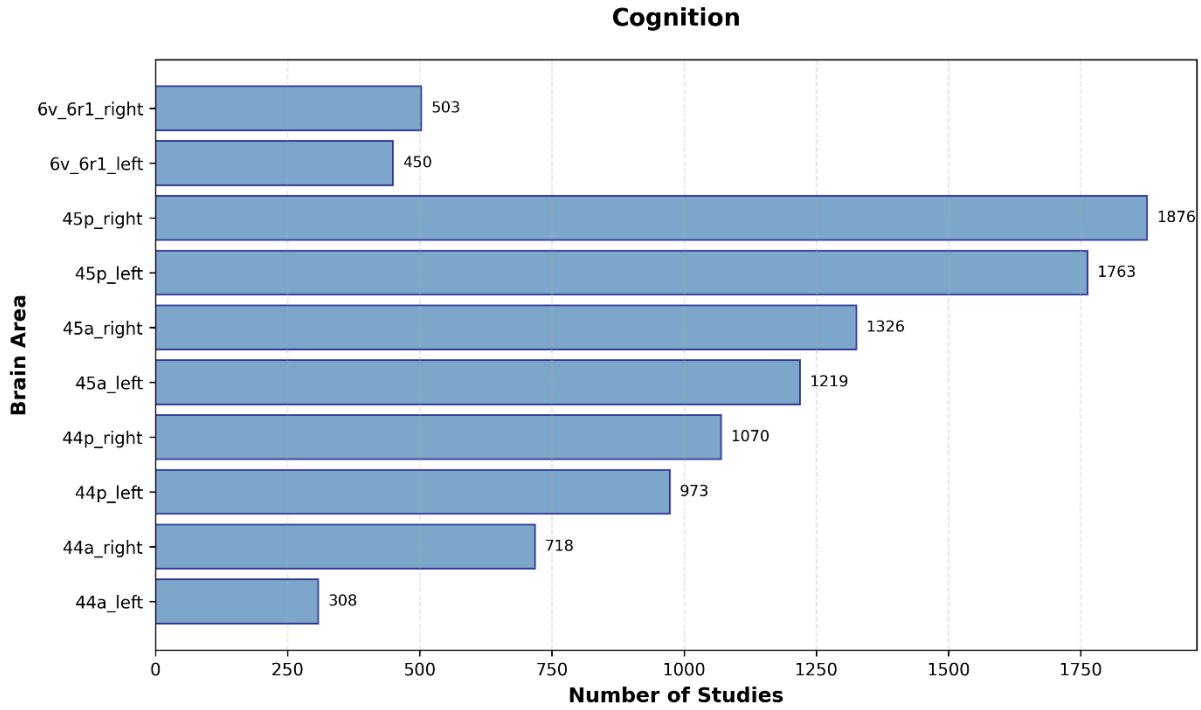

Figure 5 Cognitive domains associations across cytoarchitectonic areas. Bars represent the total number of cognition-related experiments for left and right hemispheres across five areas. Cognitive associations substantially exceed action-related ones overall, with a slight rightward predominance across regions, particularly evident in 44a and 45a, indicating a gradient bilateral but mildly right-lateralized cognitive engagement.

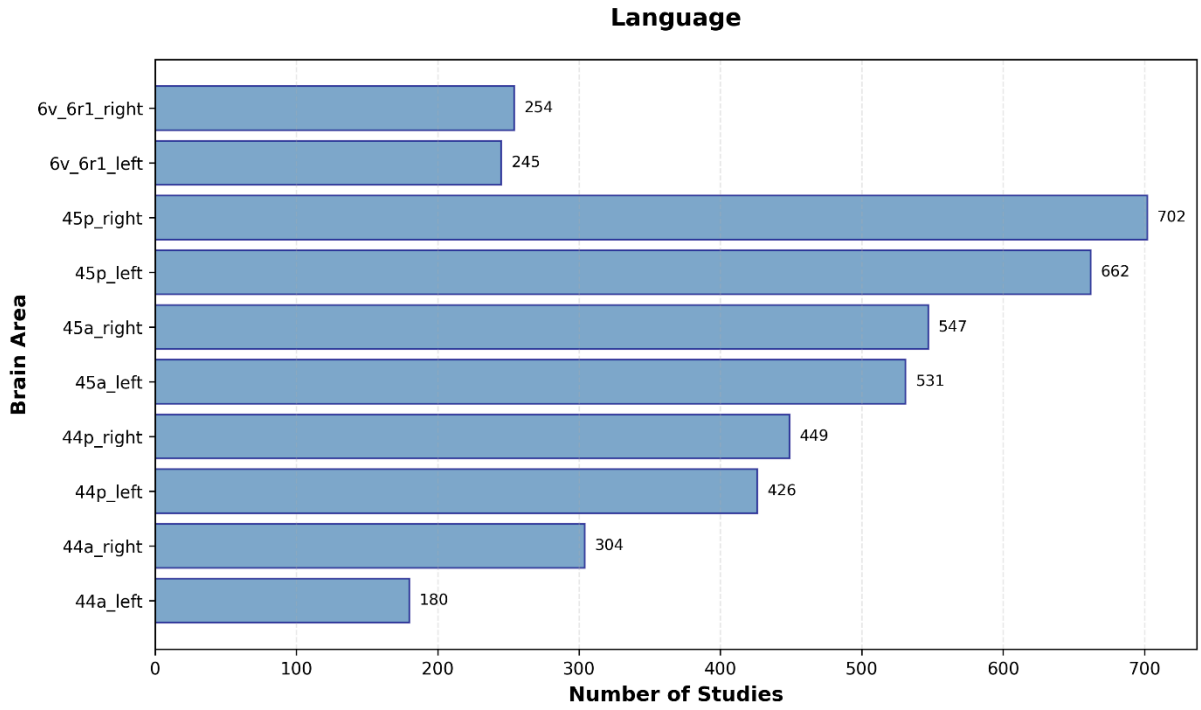

Figure 6 Language–related associations across cytoarchitectonic areas. Bar plots show the number of experiments associated with general language processing. All regions display strong bilateral involvement with only minor rightward asymmetries. The widespread representation reflects the integrative role of inferior frontal and premotor cortices in diverse linguistic operations.

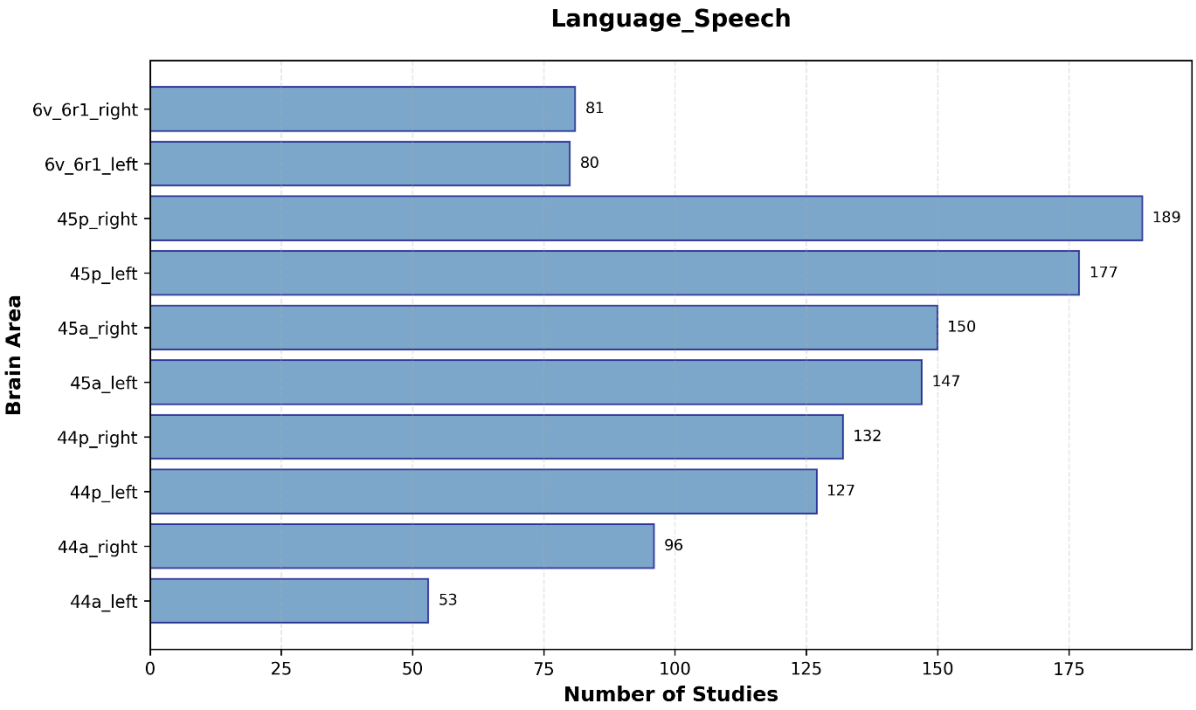

Figure 7 Speech-related language associations across cytoarchitectonic areas. The plot presents the distribution of experiments involving speech production or articulation. Bilateral patterns dominate across regions, with closely matched left-right values, indicating shared contributions of both hemispheres to articulatory aspects of speech within the inferior frontal cortex.

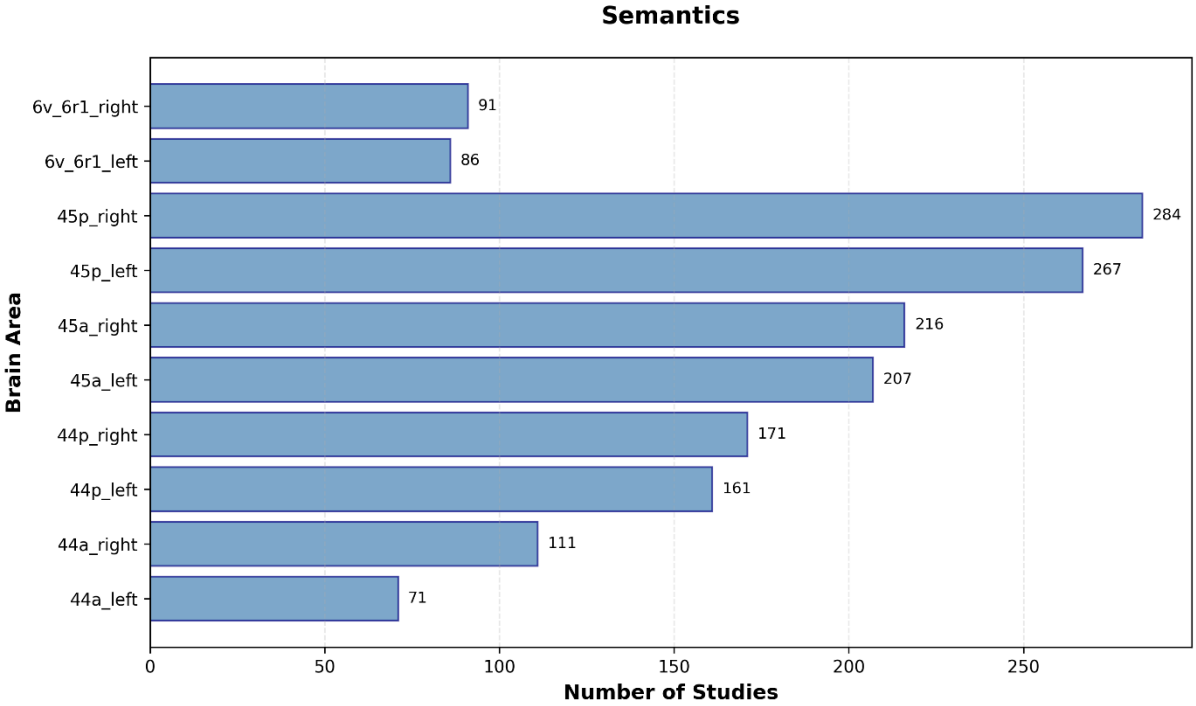

Figure 8 Semantic processing associations across cytoarchitectonic areas. Bars show the number of experiments related to semantic processing. All regions exhibit bilateral engagement, with slightly higher high-hemisphere counts, particularly in 44a and 45a.

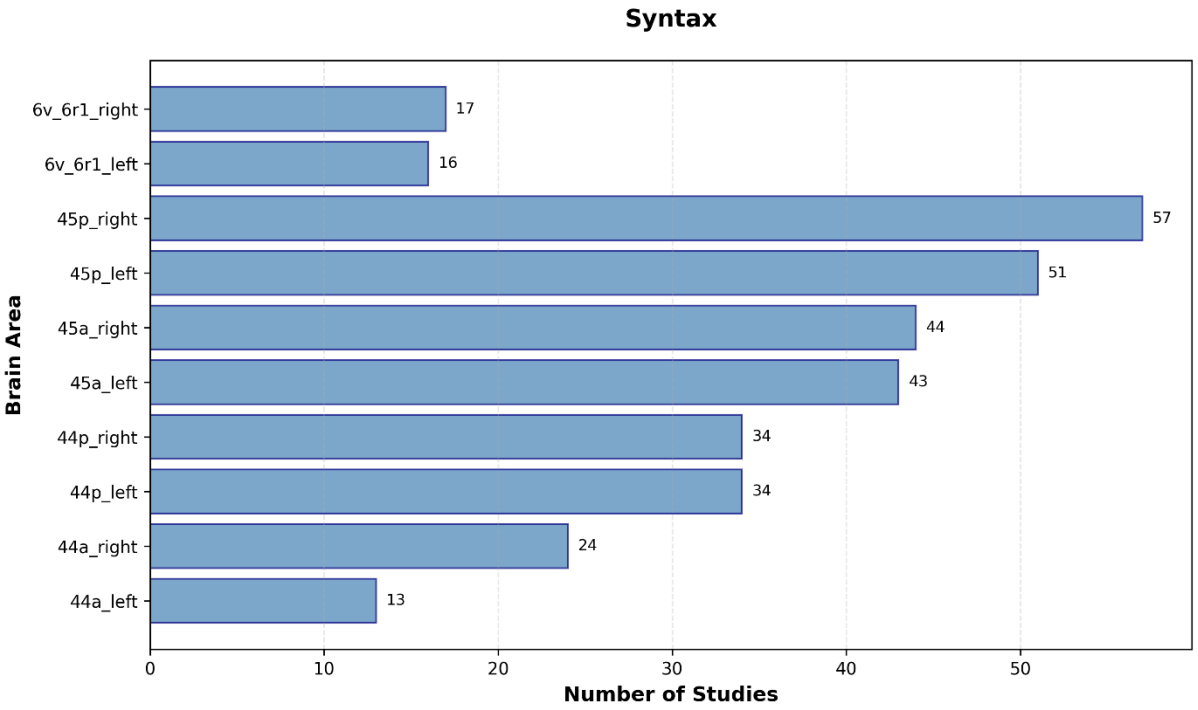

Figure 9 Syntax-related associations across cytoarchitectonic areas. The plot illustrates the distribution of syntax-related experiments. The hemispheric counts are nearly symmetrical in all regions, with only minor rightward differences in 6r1 and 44a.

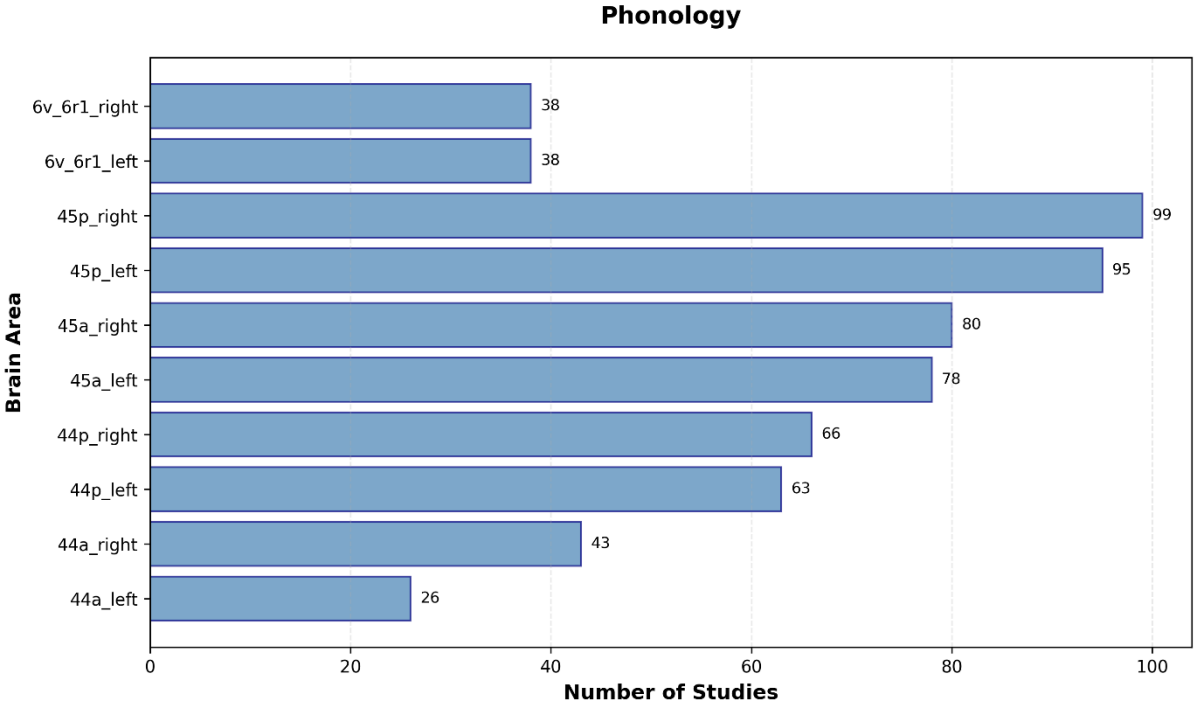

Figure 10 Phonology-related associations across cytoarchitectonic areas. Bars represent the number of experiments linked to phonological processing. Values are highly comparable between hemispheres across all areas.

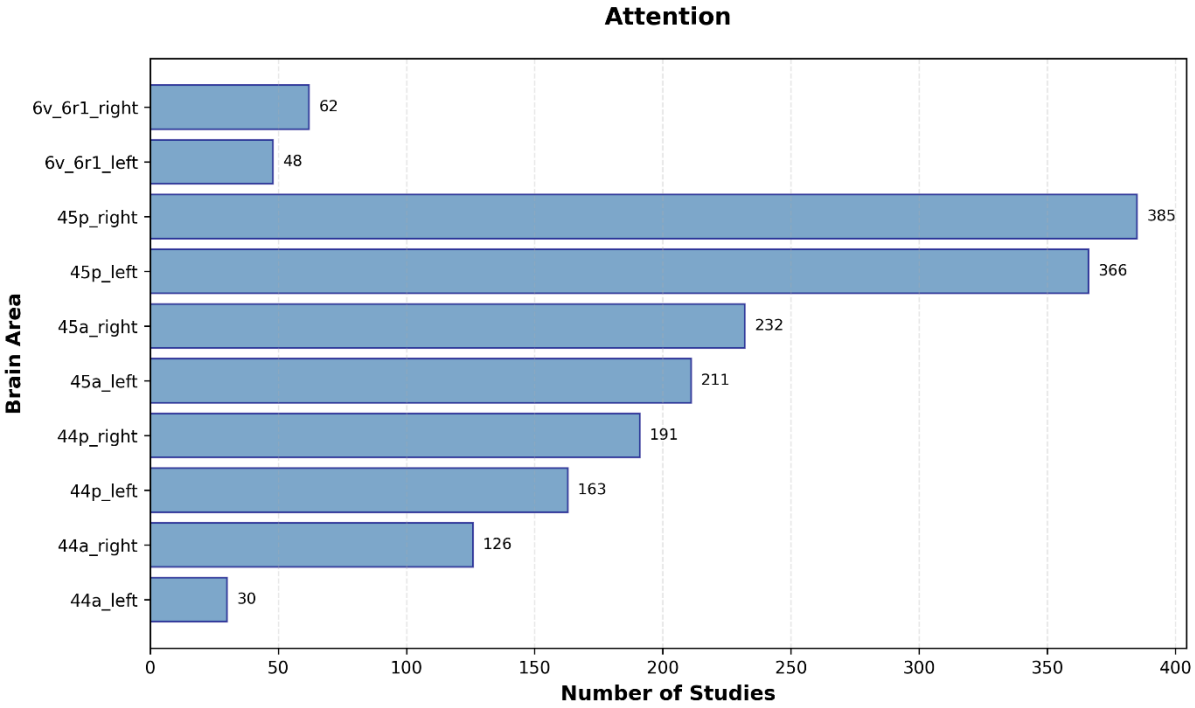

Figure 11 Attention – related functional associations across cytoarchitectonic areas. The plot displays the number of BrainMap experiments linked to attention processes in each area for both hemispheres. While attention is broadly represented bilaterally, higher right-hemisphere values – especially in 44a, 44p, and 5r1 – reflect the established right–hemispheric specialisation for attentional control networks

Co-activation Patterns of Left Areas 6r1 and 44p

Input cluster	Area	Map value	Map containedness	Input containedness	Input region
1	PFcm (IPL) left	0.887342334	0.137210879	0.926752504	6r1 left
1	PF (IPL) left	0.869073153	0.07544191	0.765665236	6r1 left
1	TPJ (STG, SMG) left	0.83015281	0.122755115	0.842918455	6r1 left
1	PFop (IPL) left	0.825640678	0.099259188	0.586552217	6r1 left
1	Te 2.2 (STG) left	0.796301603	0.115978853	0.809728183	6r1 left
3	hIP1 (IPS) left	0.906019866	0.395704112	0.594546396	6r1 left
3	hIP3 (IPS) left	0.879141629	0.425031704	0.751941552	6r1 left
3	hIP2 (IPS) left	0.871724784	0.416404361	0.52511074	6r1 left
4	Temporal-to-Parietal (GapMap) left	1	0.017710394	0.634216406	6r1 left
4	FG4 (FusG) left	0.898326635	0.08981345	0.894350463	6r1 left
4	FG2 (FusG) left	0.877713859	0.12136954	0.820300032	6r1 left
7	45 (IFG) right	0.887148619	0.09377241	0.844484629	6r1 left
7	MFG4 (MFG) right	0.874043226	0.090118318	0.99560837	6r1 left
7	MFG1 (MFG) right	0.815519631	0.124806999	0.50116249	6r1 left
7	MFG5 (MFG, IFG) right	0.811846733	0.287517392	0.747352105	6r1 left
8	7PC (SPL) right	0.912358046	0.093816201	0.52374695	6r1 left
8	hIP1 (IPS) right	0.893188417	0.174837834	0.870283462	6r1 left
8	hIP3 (IPS) right	0.887288392	0.107876098	0.620424254	6r1 left
8	hIP2 (IPS) right	0.855780363	0.263782017	0.939553219	6r1 left
8	PGa (IPL) right	0.844042838	0.067577249	0.548901821	6r1 left

8	PFm (IPL) right	0.829043686	0.105365223	0.642575558	6r1 left
1	Temporal-to-Parietal (GapMap) left	1	0.105041268	0.536584255	44p left
3	hIP1 (IPS) left	0.906019866	0.442874646	0.700987819	44p left
3	hIP6 (IPS) left	0.903438091	0.388818242	0.537361372	44p left
3	hIP3 (IPS) left	0.879141629	0.454134556	0.846372947	44p left
3	7A (SPL) left	0.878652751	0.18175949	0.511847767	44p left
6	7A (SPL) right	0.91081953	0.103905788	0.544829446	44p left
6	hIP6 (IPS) right	0.895308852	0.252735289	0.625994337	44p left
6	hIP1 (IPS) right	0.893188417	0.212814904	0.760819738	44p left
6	hIP3 (IPS) right	0.887288392	0.220713516	0.911689362	44p left
7	45 (IFG) right	0.887148619	0.603654514	0.533664697	44p left

Table 1 Overlapping Julich-Brain Areas Between MACM Clusters of Areas 6r1 and 44p (Map Containedness > 0.30, Input Containedness > 0.50). Cytoarchitectonic regions from the Julich-Brain Atlas that overlap between the MACM co-activation clusters of areas 6r1 and 44p are listed. Only regions exceeding the thresholds of map containedness > 0.30 and input containedness > 0.50 are included. For each input cluster, the table reports the anatomical area, map containedness, input containedness, and the originating dataset (input region). These regions represent areas consistently assigned to both 6r1 and 44p.

Input cluster	Area	Map value	Map containedness	Input containedness	Input region
5	6d3 (SFS) right	0.91635734	0.174200913	0.06132701	6r1 left
6	FG4 (FusG) right	0.91149038	0.003701396	0.031611894	6r1 left
6	hOc4v (LingG) right	0.90799743	0.005590161	0.043818466	6r1 left
6	FG2 (FusG) right	0.83139753	0.007359969	0.048200313	6r1 left
6	FG1 (FusG) right	0.78659385	0.009381663	0.048200313	6r1 left
7	SFG3 (SFG) right	0.79211158	0.009707724	0.0480496	6r1 left
8	PFcm (IPL) right	0.88651329	0.010339123	0.042237657	6r1 left

Table 2 Non-overlapping Julich-Brain Areas Unique to MACM Clusters of Area 6r1 (Map Containedness > 0.5, Input Containedness > 0.03) Cytoarchitectonic regions from the Julich-Brain Atlas that are exclusively associated with the MACM co-activation clusters of area 6r1 and do not overlap with clusters of area 44p are listed. Only regions exceeding the thresholds of map containedness > 0.5 and input containedness > 0.03 are included. For each input cluster, the table reports the anatomical area, map containedness, input containedness, and the originating dataset (input region). These regions highlight areas uniquely assigned to 6r1.

Input cluster	Area	Map value	Map containedness	Input containedness	Input region
6	Area 7P (SPL) right	0.91371346	0.052318828	0.157880545	44p left
6	Area hIP8 (IPS) right	0.83633757	0.079708626	0.205069435	44p left
6	Area hIP5 (IPS) right	0.83221406	0.057377897	0.14952137	44p left

Table 3 Non-overlapping Julich-Brain Areas Unique to MACM Clusters of Area 44p (Map Containedness > 0.03, Input Containedness > 0.1). Cytoarchitectonic regions from the Julich-Brain Atlas that are exclusively associated with the MACM co-activation clusters of area 44p and do not overlap with clusters of area 6r1 are listed. Only regions exceeding the thresholds of map containedness > 0.03 and input containedness > 0.1 are included. For each input cluster, the table reports the anatomical area, map containedness, input containedness, and the originating dataset (input region). These regions highlight areas uniquely assigned to 44p.

Co-activation Patterns of Left Areas 44p and 44a

Input cluster	Area	Map value	Map containedness	Input containedness	Input region
2	44 (IFG) left	0.88717467	0.750180306	0.461798618	44p left
2	45 (IFG) left	0.87480873	0.760803092	0.344393518	44p left
3	hIP1 (IPS) left	0.90601987	0.442874646	0.700987819	44p left
3	hIP6 (IPS) left	0.90343809	0.388818242	0.537361372	44p left
3	hIP3 (IPS) left	0.87914163	0.454134556	0.846372947	44p left
3	hIP2 (IPS) left	0.87172478	0.372656357	0.495060905	44p left
7	Area 45 (IFG) right	0.88714862	0.603654514	0.533664697	44p left
7	Area 6v3 (PreCG) right	0.84712487	0.389446258	0.329774554	44p left
1	Area TPJ (STG, SMG) left	0.83015281	0.354014751	0.409347145	44a left
1	Area Te 2.2 (STG) left	0.7963016	0.347034958	0.407998073	44a left
2	Area 44 (IFG) left	0.88717467	0.672563744	0.576567075	44a left
2	Area 45 (IFG) left	0.87480873	0.728206312	0.459056937	44a left
3	Area hIP1 (IPS) left	0.90601987	0.414618271	0.695459508	44a left
3	Area hIP6 (IPS) left	0.90343809	0.377022583	0.552180335	44a left
3	Area hIP3 (IPS) left	0.87914163	0.410431503	0.810609466	44a left
3	Area hIP2 (IPS) left	0.87172478	0.340905981	0.47993064	44a left
4	VA (Thalamus, ventral anterior Nucleus (ventral)) left	0.65829515	0.447488152	0.508126144	44a left
4	VAmc (Thalamus, ventral anterior Nucleus, magnocellular part) left	0.5572722	0.505101456	0.474222366	44a left
5	Frontal-I.2 (GapMap) left	1	0.479383106	0.33163698	44a left
6	Area Id8 (Insula) right	0.90943766	0.596127485	0.302429695	44a left
6	Area 45 (IFG) right	0.88714862	0.428300967	0.648976398	44a left
6	Area Op9 (Frontal Operculum) right	0.86432695	0.610342066	0.463771896	44a left

Table 4 Overlapping Julich-Brain Areas Between MACM Clusters of Areas 44p Left and 44a Left (Map Containedness > 0.3, Input Containedness > 0.3). Cytoarchitectonic regions from the Julich-Brain Atlas that overlap between the MACM co-activation clusters of areas 44p left and 44a left are listed. Only regions exceeding the thresholds of map containedness > 0.3 and input containedness > 0.3 are included. For each input cluster, the table reports the anatomical area, map containedness, input containedness, and the originating dataset (input region). These regions represent areas consistently assigned to both 44p left and 44a left.

Input cluster	Area	Map value	Map containedness	Input containedness	Input region
5	VIM (Thalamus, ventral intermediate Nucleus) right	0.99683952	0.251105217	0.139695032	44p left
5	Rt (Thalamus, reticular Nucleus) right	0.90744412	0.134796238	0.176258403	44p left

5	VLP (Thalamus, ventral lateral posterior Nucleus) right	0.87824821	0.285114717	0.16707657	44p left
5	AV (Thalamus, anteroventral Nucleus) right	0.81348008	0.219787373	0.166092802	44p left
5	VAmc (Thalamus, ventral anterior Nucleus, magnocellular part) right	0.63393229	0.263833555	0.390883751	44p left
5	CL (Thalamus, anterior intralaminar nuclei) right	0.61638868	0.133439571	0.260862436	44p left
5	VA (Thalamus, ventral anterior Nucleus (ventral)) right	0.60948253	0.287043665	0.460239384	44p left
5	AM (Thalamus, anteromedial Nucleus) right	0.59014434	0.194352658	0.106082964	44p left
5	VLA (Thalamus, ventral lateral anterior Nucleus) right	0.50046694	0.191393706	0.195441876	44p left
6	7A (SPL) right	0.91081953	0.103905788	0.544829446	44p left
6	hIP6 (IPS) right	0.89530885	0.252735289	0.625994337	44p left
6	hIP1 (IPS) right	0.89318842	0.212814904	0.760819738	44p left
6	hIP3 (IPS) right	0.88728839	0.220713516	0.911689362	44p left
6	hIP2 (IPS) right	0.85578036	0.164804469	0.421599029	44p left

Table 5 Non-overlapping Julich-Brain Areas Unique to MACM Clusters of Area 44p Left (Map Containedness > 0.1, Input Containedness > 0.1). Cytoarchitectonic regions from the Julich-Brain Atlas that are exclusively associated with the MACM co-activation clusters of area 44p left and do not overlap with clusters of 44a left are listed. Only regions exceeding the thresholds of map containedness > 0.1 and input containedness > 0.1 are included. For each input cluster, the table reports the anatomical area, map containedness, input containedness, and the originating dataset (input region). These regions highlight areas uniquely assigned to 44p left.

Input cluster	Area	Map value	Map containedness	Input containedness	Input region
1	Op1 (POperc) left	0.90511465	0.070322138	0.024716936	44a left
1	Ig2 (Insula) left	0.83097732	0.013405485	0.005251747	44a left

Table 6 Non-overlapping Julich-Brain Areas Unique to MACM Clusters of Area 44a Left (Map Containedness > 0.01). Cytoarchitectonic regions from the Julich-Brain Atlas that are exclusively associated with the MACM co-activation clusters of area 44a left and do not overlap with clusters of 44p left are listed. Only regions exceeding the threshold of map containedness > 0.01 are included. For each input cluster, the table reports the anatomical area, map containedness, input containedness, and the originating dataset (input region). These regions highlight areas uniquely assigned to 44a left.

Co-activation Patterns of Left Areas 45p and 45a

Input cluster	Area	Map value	Map containedness	Input containedness	Input region
1	44 (IFG) left	0.88717467	0.815811803	0.145933414	45p left
1	45 (IFG) right	0.88714862	0.872407561	0.115402712	45p left
1	45 (IFG) left	0.87480873	0.901026943	0.118521807	45p left
1	FG2 (FusG) left	0.87771386	0.332656434	0.456217617	45a left
2	Frontal-to-Temporal-I (GapMap) left	1	0.650365244	0.179571559	45a left
2	Frontal-II (GapMap) left	1	0.501522401	0.122396552	45a left

2	Op9 (Frontal Operculum) left	0.91214496	0.985844483	0.10793826	45a left
2	Id7 (Insula) left	0.9113676	0.610470375	0.114626016	45a left
2	Id8 (Insula) left	0.89605713	0.501454642	0.120761767	45a left
2	44 (IFG) left	0.88717467	0.585316703	0.585826203	45a left
2	6v2 (PreCG) left	0.87882274	0.672043553	0.141525658	45a left
2	45 (IFG) left	0.87480873	0.745687417	0.54882062	45a left
2	6v3 (PreCG) left	0.82312673	0.436082777	0.252330099	45a left
2	IFJ1 (IFS, PreCS) left	0.69139206	0.731505576	0.167108979	45a left
2	IFJ2 (IFS, PreCS) left	0.67697924	0.766075193	0.185155305	45a left
2	IFS4 (IFS) left	0.63619971	0.870816692	0.134243434	45a left
2	IFS2 (IFS) left	0.58635843	0.78666884	0.102481901	45a left
4	Frontal-to-Temporal-I (GapMap) right	1	0.3611666	0.256763474	45a left
4	Id8 (Insula) right	0.90943766	0.420407814	0.348434282	45a left
4	44 (IFG) right	0.90147179	0.308423586	0.181992473	45a left
4	Id7 (Insula) right	0.88208318	0.31936223	0.237520415	45a left
4	Op9 (Frontal Operculum) right	0.86432695	0.325649239	0.404246254	45a left
4	IFS2 (IFS) right	0.69225228	0.334316799	0.128736775	45a left

Table 7 Overlapping Julich-Brain Areas Between MACM Clusters of Areas 45p Left and 45a Left (Map Containedness > 0.3, Input Containedness > 0.1). Cytoarchitectonic regions from the Julich-Brain Atlas that overlap between the MACM co-activation clusters of areas 45p left and 45a left are listed. Only regions exceeding the thresholds of map containedness > 0.3 and input containedness > 0.1 are included. For each input cluster, the table reports the anatomical area, map containedness, input containedness, and the originating dataset (input region). These regions represent areas consistently assigned to both 45p left and 45a left.

Input cluster	Area	Map value	Map containedness	Input containedness	Input region
1	Area hIP1 (IPS) left	0.90601987	0.563749139	0.116686832	45p left
1	Area hIP6 (IPS) left	0.90343809	0.555360667	0.100264942	45p left
1	Area hIP3 (IPS) left	0.87914163	0.593698176	0.143523361	45p left
1	Area hIP2 (IPS) left	0.87172478	0.524747959	0.110423857	45p left
1	VLP (Thalamus, ventral lateral posterior Nucleus) left	0.86572701	0.606077619	0.118396667	45p left
1	Area 7PC (SPL) left	0.76468712	0.370535871	0.050070148	45p left

Table 8 Non-overlapping Julich-Brain Areas Unique to MACM Clusters of Area 45p Left (Map Containedness > 0.3, Input Containedness > 0.03). Cytoarchitectonic regions from the Julich-Brain Atlas that are exclusively associated with the MACM co-activation clusters of area 45p left and do not overlap with clusters of 45a left are listed. Only regions exceeding the thresholds of map containedness > 0.3 and input containedness > 0.03 are included. For each input cluster, the table reports the anatomical area, map containedness, input containedness, and the originating dataset (input region). These regions highlight areas uniquely assigned to 45p left.

Input cluster	Area	Map value	Map containedness	Input containedness	Input region
1	Area hIP1 (IPS) left	0.90601987	0.563749139	0.116686832	45p left
1	Area hIP6 (IPS) left	0.90343809	0.555360667	0.100264942	45p left
1	Area hIP3 (IPS) left	0.87914163	0.593698176	0.143523361	45p left
1	Area hIP2 (IPS) left	0.87172478	0.524747959	0.110423857	45p left
1	VLP (Thalamus, ventral lateral	0.86572701	0.606077619	0.118396667	45p left

	posterior Nucleus) left				
1	Area 7PC (SPL) left	0.76468712	0.370535871	0.050070148	45p left

Table 9 Non-overlapping Julich-Brain Areas Unique to MACM Clusters of Area 45a Left (Map Containedness > 0.1, Input Containedness > 0.2). Cytoarchitectonic regions from the Julich-Brain Atlas that are exclusively associated with the MACM co-activation clusters of area 45a left and do not overlap with clusters of 45p left are listed. Only regions exceeding the thresholds of map containedness > 0.1 and input containedness > 0.2 are included. For each input cluster, the table reports the anatomical area, map containedness, input containedness, and the originating dataset (input region). These regions highlight areas uniquely assigned to 45a left.

Co-activation Patterns of Left Areas 44p and 45p

Input cluster	Area	Map value	Map containedness	Input containedness	Input region
2	Frontal-to-Temporal-I (GapMap) left	1	0.663514033	0.112678079	44p left
2	Id8 (Insula) left	0.89605713	0.769549502	0.113983886	44p left
2	Op6 (Frontal Operculum) left	0.89255786	0.562399258	0.150350609	44p left
2	44 (IFG) left	0.88717467	0.750180306	0.461798618	44p left
2	6v2 (PreCG) left	0.87882274	0.92317774	0.11957274	44p left
2	45 (IFG) left	0.87480873	0.760803092	0.344393518	44p left
2	Id6 (Insula) left	0.86082768	0.584299989	0.132865854	44p left
2	6v3 (PreCG) left	0.82312673	0.624862406	0.222378919	44p left
2	IFJ1 (IFS, PreCS) left	0.69139206	0.755762082	0.106188219	44p left
2	IFJ2 (IFS, PreCS) left	0.67697924	0.84407941	0.125474987	44p left
7	Id8 (Insula) right	0.90943766	0.648046607	0.191819035	44p left
7	44 (IFG) right	0.90147179	0.86101083	0.181447011	44p left
7	45 (IFG) right	0.88714862	0.603654514	0.533664697	44p left
7	Id7 (Insula) right	0.88208318	0.636433072	0.16904623	44p left
7	Op9 (Frontal Operculum) right	0.86432695	0.638084887	0.282884893	44p left
7	Op8 (Frontal Operculum) right	0.8422215	0.879264556	0.109147161	44p left
7	IFS2 (IFS) right	0.69225228	0.729669924	0.100347425	44p left
7	IFJ1 (IFS, PreCS) right	0.64180076	0.513807975	0.172216164	44p left
7	IFS4 (IFS) right	0.53117794	0.548478346	0.142596303	44p left
1	44 (IFG) left	0.88717467	0.815811803	0.145933414	45p left
1	45 (IFG) right	0.88714862	0.872407561	0.115402712	45p left
1	45 (IFG) left	0.87480873	0.901026943	0.118521807	45p left

Table 10 Overlapping Julich-Brain Areas Between MACM Clusters of Areas 44p Left and 45p Left (Map Containedness > 0.5, Input Containedness > 0.1). Cytoarchitectonic regions from the Julich-Brain Atlas that overlap between the MACM co-activation clusters of areas 44p left and 45p left are listed. Only regions exceeding the thresholds of map containedness > 0.5 and input containedness > 0.1 are included. For each input cluster, the table reports the anatomical area, map containedness, input containedness, and the originating dataset (input region). These regions represent areas consistently assigned to both 44p left and 45p left.

Input cluster	Area	Map value	Map containedness	Input containedness	Input region
4	Frontal-I.2 (GapMap) left	1	0.421823579	0.270537599	44p left
4	Frontal-I.2 (GapMap) right	1	0.403591682	0.265074701	44p left
4	Area 6ma (preSMA, mesial SFG) left	0.90465963	0.705865644	0.20568638	44p left
6	Area 7A (SPL) right	0.91081953	0.103905788	0.544829446	44p left
6	Area hIP6 (IPS) right	0.89530885	0.252735289	0.625994337	44p left
6	Area hIP1 (IPS) right	0.89318842	0.212814904	0.760819738	44p left
6	Area hIP3 (IPS) right	0.88728839	0.220713516	0.911689362	44p left
6	Area hIP2 (IPS) right	0.85578036	0.164804469	0.421599029	44p left

Table 11 Non-overlapping Julich-Brain Areas Unique to MACM Clusters of Area 44p Left (Map Containedness > 0.1, Input Containedness > 0.2). Cytoarchitectonic regions from the Julich-Brain Atlas that are exclusively associated with the MACM co-activation clusters of area 44p left and do not overlap with clusters of 45p left are listed. Only regions exceeding the thresholds of map containedness > 0.1 and input containedness > 0.2 are included. For each input cluster, the table reports the anatomical area, map containedness, input containedness, and the originating dataset (input region). These regions highlight areas uniquely assigned to 44p left.

Input cluster	Area	Map value	Map containedness	Input containedness	Input region
1	Area hOc3v (LingG) left	0.88669282	0.115409376	0.014965584	45p left
1	Ch 4 (Basal Forebrain) left	0.77893776	0.455734132	0.012696461	45p left
1	CM (Amygdala) left	0.69910574	0.600352113	0.014233242	45p left
1	SF (Amygdala) left	0.64244306	0.401039529	0.01112553	45p left
1	MF (Amygdala) left	0.49307057	0.764388999	0.010230024	45p left
1	VTM (Amygdala) left	0.45579755	0.691649378	0.010119983	45p left

Table 12 Non-overlapping Julich-Brain Areas Unique to MACM Clusters of Area 45p Left (Map Containedness > 0.1, Input Containedness > 0.01). Cytoarchitectonic regions from the Julich-Brain Atlas that are exclusively associated with the MACM co-activation clusters of area 45p left and do not overlap with clusters of 44p left are listed. Only regions exceeding the thresholds of map containedness > 0.1 and input containedness > 0.01 are included. For each input cluster, the table reports the anatomical area, map containedness, input containedness, and the originating dataset (input region). These regions highlight areas uniquely assigned to 45p left.

Co-activation Patterns of Left Areas 44a and 45a

Input cluster	Area	Map value	Map containedness	Input containedness	Input region
1	TPJ (STG, SMG) left	0.83015281	0.354014751	0.409347145	44a left
1	Te 2.2 (STG) left	0.7963016	0.347034958	0.407998073	44a left
2	44 (IFG) left	0.88717467	0.672563744	0.576567075	44a left
2	45 (IFG) left	0.87480873	0.728206312	0.459056937	44a left
6	45 (IFG) right	0.88714862	0.428300967	0.648976398	44a left
6	Op9 (Frontal Operculum) right	0.86432695	0.610342066	0.463771896	44a left
1	FG2 (FusG) left	0.87771386	0.332656434	0.456217617	45a left
2	44 (IFG) left	0.88717467	0.585316703	0.585826203	45a left
2	45 (IFG) left	0.87480873	0.745687417	0.54882062	45a left
3	Frontal-I.2 (GapMap) left	1	0.38065432	0.458673509	45a left

4	Op9 (Frontal Operculum) right	0.86432695	0.325649239	0.404246254	45a left

Table 13 Overlapping Julich-Brain Areas Between MACM Co-activation Clusters of Areas 44a Left and 45a Left (Map Containedness > 0.30, Input Containedness > 0.40). Cytoarchitectonic regions from the Julich-Brain Atlas that fulfilled the threshold criteria for both 44a left and 45a left are listed. The table reports the anatomical area, map value, map containedness, input containedness, and the originating input cluster. These regions represent shared co-activation territories consistently assigned to both inferior frontal subdivisions 44a and 45a.

Input cluster	Area	Map value	Map containedness	Input containedness	Input region
3	hIP1 (IPS) left	0.90601987	0.414618271	0.695459508	44a left
3	hIP6 (IPS) left	0.90343809	0.377022583	0.552180335	44a left
3	hIP3 (IPS) left	0.87914163	0.410431503	0.810609466	44a left
3	hIP2 (IPS) left	0.87172478	0.340905981	0.47993064	44a left
4	MD (Thalamus, mediodorsal Nucleus) left	0.90516955	0.458636664	0.149176623	44a left
4	AV (Thalamus, anteroventral Nucleus) left	0.78531861	0.536635471	0.253040577	44a left
4	VA (Thalamus, ventral anterior Nucleus (ventral)) left	0.65829515	0.447488152	0.508126144	44a left
4	AM (Thalamus, anteromedial Nucleus) left	0.59306312	0.532305674	0.174685179	44a left
4	VAmc (Thalamus, ventral anterior Nucleus, magnocellular part) left	0.5572722	0.505101456	0.474222366	44a left
4	Pv (Thalamus, paraventricular Nucleus) left	0.5536688	0.351483801	0.138951674	44a left

Table 14 Non-overlapping Julich-Brain Areas Unique to MACM Clusters of Area 44a Left (Map Containedness > 0.3, Input Containedness > 0.1). Cytoarchitectonic regions from the Julich-Brain Atlas that are exclusively associated with the MACM co-activation clusters of area 44a left and do not overlap with clusters of 45a left are listed. Only regions exceeding the thresholds of map containedness > 0.3 and input containedness > 0.1 are included. For each input cluster, the table reports the anatomical area, map containedness, input containedness, and the originating dataset (input region). These regions highlight areas uniquely assigned to 44a left.

Input cluster	Area	Map value	Map containedness	Input containedness	Input region
1	Area hOc5 (LOC) left	0.88500285	0.10248024	0.073056995	45a left
1	Area hOc4v (LingG) left	0.86302942	0.010490156	0.018393782	45a left

Table 15 Non-overlapping Julich-Brain Areas Unique to MACM Clusters of Area 45a Left (Map Containedness > 0.01). Cytoarchitectonic regions from the Julich-Brain Atlas that are exclusively associated with the MACM co-activation clusters of area 45a left and do not overlap with clusters of 44a left are listed. Only regions exceeding the threshold of map containedness > 0.01 are included. For each input cluster, the table reports the anatomical area, map containedness, input containedness, and the originating dataset (input region). These regions highlight areas uniquely assigned to 45a left.

Co-activation Patterns of Right Areas 44p and 45p

Input cluster	Area	Map value	Map containedness	Input containedness	Input region
2	Id6 (Insula) left	0.86082768	0.54800735	0.205841116	44p right
2	6v3 (PreCG) left	0.82312673	0.508806047	0.299109165	44p right
4	6ma (preSMA, mesial SFG) right	0.91375273	0.81490071	0.217292158	44p right
5	45 (IFG) right	0.88714862	0.614296779	0.399772252	44p right
1	IFJ1 (IFS, PreCS) left	0.69139206	0.696561338	0.204418383	45p right
1	IFJ2 (IFS, PreCS) left	0.67697924	0.729093465	0.226373926	45p right
6	45 (IFG) right	0.88714862	0.670663492	0.534192428	45p right
6	Op9 (Frontal Operculum) right	0.86432695	0.523910308	0.209267256	45p right

Table 16 Overlapping Julich-Brain Areas Between MACM Clusters of Areas 44p Right and 45p Right (Map Containedness > 0.5, Input Containedness > 0.2). Cytoarchitectonic regions from the Julich-Brain Atlas that overlap between the MACM co-activation clusters of areas 44p right and 45p right are listed. Only regions exceeding the thresholds of map containedness > 0.5 and input containedness > 0.2 are included. For each input cluster, the table reports the anatomical area, map containedness, input containedness, and the originating dataset (input region). These regions represent areas consistently assigned to both 44p right and 45p right.

Input cluster	Area	Map value	Map containedness	Input containedness	Input region
2	VIM (Thalamus, ventral intermediate Nucleus) left	0.996490121	0.702718334	0.052414745	44p right
2	VLP (Thalamus, ventral lateral posterior Nucleus) left	0.865727007	0.317566145	0.097603589	44p right
2	VA (Thalamus, ventral anterior Nucleus (ventral)) left	0.658295155	0.357630332	0.081383059	44p right
2	VAmc (Thalamus, ventral anterior Nucleus, magnocellular part) left	0.557272196	0.310214376	0.058368025	44p right
2	VLA (Thalamus, ventral lateral anterior Nucleus) left	0.527197242	0.491163056	0.074329717	44p right
5	VAmc (Thalamus, ventral anterior Nucleus, magnocellular part) right	0.633932292	0.48793714	0.082306601	44p right
5	CL (Thalamus, anterior intralaminar nuclei) right	0.616388679	0.357628114	0.079599761	44p right
5	VA (Thalamus, ventral anterior Nucleus (ventral)) right	0.609482527	0.535637591	0.097782258	44p right
5	VLA (Thalamus, ventral lateral anterior Nucleus) right	0.500466943	0.559890816	0.065094833	44p right

Table 17 Non-overlapping Julich-Brain Areas Unique to MACM Clusters of Area 44p Right (Map Containedness > 0.3, Input Containedness > 0.05). Cytoarchitectonic regions from the Julich-Brain Atlas that are exclusively associated with the MACM co-activation clusters of area 44p right and do not overlap with clusters of 45p right are listed. Only regions exceeding the thresholds of map containedness > 0.3 and input containedness > 0.05 are included. For each input cluster, the table reports

the anatomical area, map containedness, input containedness, and the originating dataset (input region). These regions highlight areas uniquely assigned to 44p right.

Input cluster	Area	Map value	Map containedness	Input containedness	Input region
2	Area FG4 (FusG) left	0.898326635	0.158664017	0.8907684	45p right
2	Area FG1 (FusG) left	0.881975472	0.173485892	0.521144502	45p right
2	Area FG2 (FusG) left	0.877713859	0.243589138	0.928198668	45p right

Table 18 Non-overlapping Julich-Brain Areas Unique to MACM Clusters of Area 45p Right (Map Containedness > 0.1, Input Containedness > 0.5). Cytoarchitectonic regions from the Julich-Brain Atlas that are exclusively associated with the MACM co-activation clusters of area 45p right and do not overlap with clusters of 44p right are listed. Only regions exceeding the thresholds of map containedness > 0.1 and input containedness > 0.5 are included. For each input cluster, the table reports the anatomical area, map containedness, input containedness, and the originating dataset (input region). These regions highlight areas uniquely assigned to 45p right.

Co-activation Patterns of Right Areas 44a and 45a

Input cluster	Area	Map value	Map containedness	Input containedness	Input region
2	44 (IFG) left	0.887174666	0.592698655	0.582626103	44a right
2	45 (IFG) left	0.874808729	0.592799862	0.428508873	44a right
2	6v3 (PreCG) left	0.823126733	0.463675057	0.263506892	44a right
4	VLP (Thalamus, ventral lateral posterior Nucleus) left	0.865727007	0.415608113	0.262313962	44a right
4	VA (Thalamus, ventral anterior Nucleus (ventral)) left	0.658295155	0.57563981	0.269002481	44a right
5	Frontal-I.2 (GapMap) right	1	0.516131065	0.291712668	44a right
5	Frontal-I.2 (GapMap) left	1	0.412660515	0.227750276	44a right
7	Area 45 (IFG) right	0.887148619	0.748831072	0.491702925	44a right
7	Op9 (Frontal Operculum) right	0.864326954	0.741391145	0.244128007	44a right
1	Frontal-to-Temporal-I (GapMap) left	1	0.492579777	0.224276161	45a right
1	Id8 (Insula) left	0.896057129	0.519262982	0.206210832	45a right
1	45 (IFG) left	0.874808729	0.501269255	0.60837447	45a right
5	45 (IFG) right	0.887148619	0.644817991	0.631202089	45a right
5	Op9 (Frontal Operculum) right	0.864326954	0.78446402	0.385084099	45a right

Table 19 Overlapping Julich-Brain Areas Between MACM Clusters of Areas 44a Right and 45a Right (Map Containedness > 0.4, Input Containedness > 0.2). Cytoarchitectonic regions from the Julich-Brain Atlas that overlap between the MACM co-activation clusters of areas 44a right and 45a right are listed. Only regions exceeding the thresholds of map containedness > 0.4 and input containedness > 0.2 are included. For each input cluster, the table reports the anatomical area, map containedness, input containedness, and the originating dataset (input region). These regions represent areas consistently assigned to both 44a right and 45a right.

Input cluster	Area	Map value	Map containedness	Input containedness	Input region
3	hIP1 (IPS) left	0.906019866	0.453786661	0.682600933	44a right

3	hIP3 (IPS) left	0.879141629	0.461938673	0.818176582	44a right
3	hIP2 (IPS) left	0.871724784	0.428128279	0.540517192	44a right
4	CL (Thalamus, anterior intralaminar nuclei) left	0.646935046	0.466514769	0.25394224	44a right
4	VAmc (Thalamus, ventral anterior Nucleus, magnocellular part) right	0.633932292	0.543382027	0.217487597	44a right
4	CL (Thalamus, anterior intralaminar nuclei) right	0.616388679	0.440660907	0.232725018	44a right
4	VA (Thalamus, ventral anterior Nucleus (ventral)) right	0.609482527	0.560384497	0.242735648	44a right
4	VAmc (Thalamus, ventral anterior Nucleus, magnocellular part) left	0.557272196	0.615269976	0.237730333	44a right
6	hIP1 (IPS) right	0.893188417	0.414730729	0.414308857	44a right

Table 20 Non-overlapping Julich-Brain Areas Unique to MACM Clusters of Area 44a Right (Map Containedness > 0.4, Input Containedness > 0.2). Cytoarchitectonic regions from the Julich-Brain Atlas that are exclusively associated with the MACM co-activation clusters of area 44a right and do not overlap with clusters of 45a right are listed. Only regions exceeding the thresholds of map containedness > 0.4 and input containedness > 0.2 are included. For each input cluster, the table reports the anatomical area, map containedness, input containedness, and the originating dataset (input region). These regions highlight areas uniquely assigned to 44a right.

Input cluster	Area	Map value	Map containedness	Input containedness	Input region
3	LB (Amygdala) left	0.901495099	0.361296473	0.316977976	45a right
3	Astr (Amygdala) left	0.802229047	0.393924178	0.43741288	45a right
3	IF (Amygdala) left	0.776243269	0.407666861	0.584053527	45a right
3	CM (Amygdala) left	0.69910574	0.469910371	0.818511291	45a right
3	HATA (Hippocampus) left	0.653480947	0.391835673	0.420128241	45a right
3	SF (Amygdala) left	0.642443061	0.381343182	0.777251185	45a right
3	MF (Amygdala) left	0.493070573	0.742273887	0.72985782	45a right
3	VTM (Amygdala) left	0.455797553	0.526970954	0.566490103	45a right

Table 21 Non-overlapping Julich-Brain Areas Unique to MACM Clusters of Area 45a Right (Map Containedness > 0.3, Input Containedness > 0.2). Cytoarchitectonic regions from the Julich-Brain Atlas that are exclusively associated with the MACM co-activation clusters of area 45a right and do not overlap with clusters of 44a right are listed. Only regions exceeding the thresholds of map containedness > 0.3 and input containedness > 0.2 are included. For each input cluster, the table reports the anatomical area, map containedness, input containedness, and the originating dataset (input region). These regions highlight areas uniquely assigned to 45a right.

Acknowledgement

I want to express my heartfelt gratitude to my supervisor, Prof. Dr. med. Dr. h. c. Katrin Amunts, for believing in me since the beginning of my work at the Institute of Neuroscience and Medicine – 1, at Forschungszentrum Jülich, and for encouraging me to apply to the Max Planck School of Cognition, and start my doctoral work at the C&O Vogt Institute for Brain Research. Under her guidance, I successfully completed this work, attended numerous conferences and events, and even co-organized a symposium during the Meeting of the German Neuroscience Society.

I am sincerely thankful to Prof. Dr. Dr. h. c. Angela D. Friederici, who kindly agreed to serve as my second co-supervisor and welcomed me to spend five weeks in the Department of Neuropsychology at the Max Planck Institute for Human Cognitive and Brain Sciences in Leipzig. This stay allowed me to work on the third part of my thesis and deepen my understanding of the functional neuroanatomy of language.

I am also grateful to Prof. Dr. med. Michael Sabel, who agreed to serve as my third co-supervisor.

My deepest gratitude goes to:

- Prof. Arno Villringer for guidance and mentorship throughout my time at the Max Planck School of Cognition
- Dr. Sabine Ruland, my office neighbour and day-to-day supervisor. Your positive energy has motivated me even through challenging moments. Our long discussions and conversations were invaluable in achieving results. It would not have been the same without you. My German has also greatly improved thanks to your patience in keeping our work dialogues in German. Thank you as well for proofreading my thesis even while on maternity leave.
- Dr. Sebastian Bludau, for helping with the statistical part of the work and discussing the results.
- Hartmut Mohlberg for calculating the probability maps.
- Prof. Dr. Markus Axer for introducing me to the 3D-PLI and for the ongoing work on applying the method to study Broca's region.
- Dr. Roxana N. Kooijmans for introducing me to the difficult staining methods that you apply, for the interesting conversations, and for the ongoing collaboration.
- Dr. Christian Schiffer, for teaching me how to create high-quality images in ParaView, and guiding me in applying his 3D reconstruction pipeline for the newly mapped areas in the BigBrain model.
- Dr. Kai Benning, for explaining the complex physics-related components of the project, for your help with statistics and programming, as well as the visualisation of the results. Thank you for being there during both successful and difficult moments, and for always motivating me.
- Dr. Peter Pieperhoff for assisting with the visualisation of the results.
- Dr. Patrick C. Trettenbrein, for introducing me to BrainMap and MACM analyses, guiding me through them, proofreading my thesis, and helping me understand the functional organisation of language and the interpretation of fMRI research results. Thank you for your warm welcome during my research stay in Leipzig and for our many Zoom calls afterwards.
- Dr. Charlotta Eick for presenting the results of her first approaches on subdividing areas 44 and 45 in BigBrain at one of our group meetings.
- Dr. Ahmet Nihat Simsek, for your help and support with SIIBRA Python.
- Dr. Kimberley Lothmann for our discussions on mapping.

- Dr. Manuel Marx for managing the finances and help during the organisation of the symposium.
- Dr. Felix Ströckens for help with teaching and with the organisation of the symposium.
- Dr. Evelyn Overmann for your support with teaching, and also for helping me to prepare my first lecture.
- Dr. Eve-Marie Frigon, thank you for becoming a very good friend, for sharing international insights on the scientific work, for encouraging me to prepare my first poster, and for the trips we have taken during your stay in Jülich.
- Anna Stössel for making bureaucracy much easier and handling organisational matters both at the institute and the university. Thank you also for supporting me in my journey to learn German.
- Janine Hucko and Stefanie Mattig for their great help during my work at the INM-1 and for all your organisational support.
- Natasha Mendes for helping with organisational work at the Max Planck School of Cognition.
- Dr. Alfred Anwander and Aarushi Juyal for many helpful discussions during my stay in Leipzig.
- Dr. Zieng Zhang, for our discussions about mapping our neighbouring areas with a difficult cytoarchitecture.
- Alexey Chervonyy, for our discussions about our PhD progress, and for co-organising the NWG symposium.
- Dr. Felix Matuschke for explaining many aspects of physics.
- Daniel Krötz, for your help with Linux, and for expanding my social circle during my move to Jülich.
- My parents, Tetiana Fedorchenko and Olexandr Fedorchenko, and all my family for being both far away and always close. Thank you for your unwavering support and understanding throughout my PhD, and for giving me the space to grow, even when that meant seeing each other only once or twice a year.

To all my colleagues, from the INM-1 at the Forschungszentrum Jülich, C&O Vogt Institute for Brain Research, Max Planck School of Cognition, and Max Planck Institute for Human Cognitive and Brain Sciences: thank you for many inspiring discussions, the supportive conversations, and the warm and welcoming environment.

And finally, to all my friends, thank you for being there for me, despite my limited ability to meet at times, and despite the distances, for always finding ways to meet, stay connected, and support one another across countries.

This PhD position was funded by the Max Planck School of Cognition, Leipzig, Germany

I would like to sincerely thank the research group of Edward F. Chang, who provided open access to the code and data of their study “Speech sequencing in the human precentral gyrus,” authors Jessie R. Liu et al. (2025). Their generosity allowed me to integrate their findings with my results, enriching this work.